Emissions and Climate Impacts of Aerosol Emissions from Cookstoves and Gasoline Direct Injection Vehicles

Submitted in partial fulfillment of the requirements for

the degree of

Doctor of Philosophy

in

Mechanical Engineering

Georges Saliba

B.Eng., Mechanical Engineering, American University of Beirut
M.S., Mechanical Engineering, Carnegie Mellon University

Carnegie Mellon University
Pittsburgh, PA

February 2018

In loving memory of my father who passed on to me his passion for numbers

and his joy for life

ACKNOWLEDGMENTS

I met Othman and Karim in Pittsburgh while playing pick-up soccer. It was surprising to meet two amazing Lebanese persons. I have shared with them a memorable time, loud laughter, and countless meals!

Rayan and Samira are truly amazing friends. Our visits cleared my mind when I needed it the most. Also, I am grateful to the support of my best friends from high school: Toufic, Tarek, and Sandra. I cannot thank enough Toufic with whom I have the craziest laughs and Tarek and Elie for visiting me in Pittsburgh so many times!

My dear fiancée and partner Maria supported me every step of the way. She is by my side through all the good and the bad, and for that I love her more and more every day. Her long visits to the United States have made my stay here extraordinary. We travelled together to many places in the US and she loved Pittsburgh. Now I can't wait for her to visit me in San Diego! My thesis would not have seen the light without her help.

There are no words to describe the support my family has given me over the years. I want to thank from the depth of my heart my cousin Cyril for being an amazing friend. Carina, Serge, and George who are amazing human beings. My aunt Nicole and her sons Edwin and Alex with whom I spent amazing holidays in Washington DC. My grandfather Edwin who has a resolve like I have never seen, and from whom I still learn today. My father Dimitri who always believed in me and pushed me to achieve more than I ever thought was possible. My brothers Edwin and Cedric for always being there for me. My mother who has shown nothing but unconditional love for me and my brothers.

ABSTRACT

Anthropogenic gas- and particle-phase emissions affect the climate by absorbing and scattering radiation, and have been linked to adverse health effects. Black carbon (BC), a by-product of incomplete combustion, is the most potent light-absorbing component of atmospheric aerosols, with a top-of-the atmosphere direct radiative forcing estimated to be only second to CO_2. However, there is a large uncertainty associated with BC's total direct and indirect radiative forcings due to uncertain source emissions and optical properties and complex interactions with clouds.

In this dissertation we investigate the direct radiative impact of two of the most important sources of BC particles: biofuel combustion and vehicles. Together these sources contribute around 40% of the global atmospheric BC burden. Recently, both of these energy sources are undergoing rapid technology changes, and the climate impacts from the emissions of these newly adopted technologies remain uncertain. We also investigate the role of atmospheric processing on the optical properties and growth rates of particles.

This dissertation first assesses the climate impacts of aerosol emissions of two rapidly emerging technologies: improved cookstoves and gasoline direct injection (GDI) vehicles. We performed extensive measurements of gas- and particle emissions and optical properties of emissions from both these sources. Our data suggests that improved rocket cookstoves have, on average, a factor of two lower particulate matter (PM) emissions compared to traditional cookstoves but only a 4% climate benefits associated with their emissions. In contrast, we estimated a 30% climate benefit from switching traditional cookstoves to gasifier ones. Of all the stoves tested, charcoal stoves had the lowest emissions and climate impacts. Our data suggests the widespread deployment of improved

cookstoves to replace existing, inefficient, traditional cookstoves will likely result in health and climate co-benefits. Similarly, we estimated that the rapid adoption of GDI vehicles to replace existing port fuel injection (PFI) vehicles will likely result in reduced warming from emissions. This is due to the higher fuel economy of GDI engines; we measured an average CO2 reduction of 57 g/mi, from switching engine technologies. GDI engine emissions had higher PM emissions compared to PFI engines, similar to previous findings. In addition, our data suggests that newer GDI engines have a factor of two lower PM emissions compared to older GDI engines. These improvements in emissions may enable GDI-equipped vehicles to meet the new Federal Tier 3 PM standard of 3.0 mg/mi without gasoline particulate filters (GPF, which would reduce their fuel economy).

To better constrain the large uncertainty of radiative forcing associated with cookstove emissions, this dissertation examines emissions and optical properties from several cookstove and fuel combinations. We performed extensive laboratory measurements of the optical properties of fresh cookstove emissions using the newly developed firepower sweep protocol. Current model treatments of the optical properties of cookstove emissions assume: (1) complete internal mixture between BC and non-BC material and (2) absorption properties of organics based on parametrizations developed for biomass burning emissions. These assumptions do not accurately represent optical properties of fresh cookstove emissions. We developed new parametrizations of optical properties (BC-mass absorption cross section (MAC_{BC}), absorption angstrom exponent (AAE), and single scattering albedo (SSA)) of aerosol emissions from cookstoves as a function of the BC-to-PM mass ratio. These parametrizations are designed for use in climate models to more rigorously assess the global climate implications from adoption of improved stove technologies.

Upon entering the atmosphere aerosol emissions undergo complex chemical transformations. Aerosol optical properties depend on their atmospheric processing which controls the amount of coating the particles accumulate and their lifetime. To assess the effects of coating on the optical properties, we performed targeted experiments using real world, size selected, BC particles emitted from a rocket improved cookstove, and coated with biogenic secondary organic aerosol (SOA) material. These experiments explicitly target to evaluate measurements and modeling using simple formulation like Mie theory. Measurements of MAC_{BC} and the mass scattering cross section (MSC) of coated BC particles were in good agreement with Mie predictions when the organic-to-BC mass ratio>5. Scattering (but not absorption) was sensitive to BC fractal-like morphology; Mie theory under-predicted measured scattering of fresh emissions. Our data suggest that Mie theory can be used in climate models to approximate the optical properties of coated BC particles emitted from cookstoves, if the mixing-state of BC particles is known.

In this dissertation, we present initial evidence that particle growth rates depend on seed composition and gas-phase supersaturation. Current models do not account for seed-dependent growth rates. We conducted experiments to investigate the growth of diesel and biogenic SOA particles. Both seeds were exposed to the same gas-phase supersaturation, which allows us to accurately retrieve differences in growth rates and decouple the effects of surface activity and accommodation coefficients. We estimated that the accommodation coefficients of condensing material was 10% to 30% lower on the diesel particles compared to the SOA particles. Moreover, we measured larger surface activity of condensing material on the diesel particles, potentially due to less-miscible condensing vapors in the diesel particles compared to the SOA particles. Our data suggest that growth of BC (diesel) particles in the atmosphere is likely slower compared to SOA particles. Accurately

representing these processes is important to estimate the lifetime and absorption enhancement from coated BC particles, as they compete with other particles for condensable vapors.

TABLE OF CONTENTS

LIST OF ABBREVIATIONS

a: activity

a_s: average surface albedo

AAE: absorption angstrom exponent

AMS: aerosol mass spectrometer

b_{abs}: absorption coefficient

b_{sca}: scattering coefficient

BC: black carbon

BrC: brown carbon

BTEX: benzene, toluene, ethyl-benzene, and xylenes

C_{fuel}: fuel consumption rate

CCN: cloud condensation nuclei

CH_4: methane

CO: carbon monoxide

CO_2: carbon dioxide

CPMA: centrifugal particle mass analyzer

CVS: constant volume sampler

d_{me}: mass equivalent diameter

d_{mob}: mobility diameter

d_{va}: vacuum aerodynamic diameter

DMA: differential mobility analyzer

dSFE: spectral simple forcing efficiency

$dSFE_{measure}$: spectral simple forcing efficiency inferred from measurements

$dSFE_{Mie}$: spectral simple forcing efficiency calculated using Mie theory

$dSFE_{RDG}$: spectral simple forcing efficiency calculated using the Raleigh-Debye-Gans formulation

EC: elemental carbon

EEPS: engine exhaust particle sizer

EF: emission factor

f_c: carbon fraction

F_c: cloud fraction

FID: flame ionization detection

FP: firepower

FS: Fuchs-Sutugin correction factor

FTP: Federal test procedure

GDI: gasoline direct injection

GHG: greenhouse gases

GR: growth rate

GWP: global warming potential

HEPA: high efficiency particulate air

LEV: low emission vehicles

MAC: mass absorption cross section

MAC_{BC}: black carbon mass absorption cross section

MCE: modified combustion efficiency

MSC: mass scattering cross section

MSS: micro soot sensor

NMOG: non-methane organic gas

MY: model year

n_{BC}: black carbon refractive index

n_{shell}: shell refractive index

NOx: nitrogen oxides

O_3: ozone

OA: organic aerosol

OC: organic carbon

OM: organic mass

PAX: photo-acoustic extinctiometer

PFI: port fuel injection

PM: particulate matter

POA: primary organic aerosol

PTR-MS: proton transfer reaction mass spectrometry

PZEV: partial-zero emission vehicles

rBC: refractory black carbon

RDG: Rayleigh-Debye-Gans

RSD: relative standard deviation

SAE: scattering angstrom exponent

SE: standard error

SFE: simple forcing efficiency

SFE_{cook}: simple forcing efficiency associated with an hour-long cooking session

SI: supplementary information

SMPS: scanning mobility particle sizer

SOA: secondary organic aerosol

SP2: single particle soot photometer

SSA: single scattering albedo

SULEV: super-ultra-low emission vehicles

TEM: transmission electron microscopy

THC: total hydrocarbons

UC: unified cycle

ULEV: ultra-low emission vehicles

UV: ultra violet

VOC: volatile organic compounds

x: size parameter

α: mass accommodation coefficient

αp: alpha pinene

β: backscatter fraction

γ: number of hot miles driven to required to match cold-start emissions

ρ: density

σ: one-standard deviation

τ_{atm}: atmospheric transmissivity

χ: shape factor

LIST OF TABLES

LIST OF FIGURES

CHAPTER 1
INTRODUCTION

1.1 Motivation

The industrial revolution dramatically increased anthropogenic emissions of gas- and particle-phase pollutants, which have perturbed our climate system. These emissions include greenhouse gases (GHG, such as CO_2, CH_4, and N_2O) and particulate matter (PM, or aerosols). Aerosol directly affect the radiative balance of the earth by absorbing and scattering radiation. Aerosols also affect the climate via indirect effects, such as in acting as cloud condensation nuclei (CCN, particles that act as seeds for cloud droplets) which when changed can affect the lifetime, brightness, and precipitation patterns of clouds (Twomey, 1977; Lohmann and Lesins, 2002; Rosenfeld, 2006). The climate impacts of increased GHG emissions are unequivocal: global temperatures are on the rise (IPCC, 2013). However, the contributions of aerosol are more uncertain. The Intergovernmental Panel on Climate Change estimates that the overall radiative forcing of aerosol is likely negative (i.e., net cooling), but for biomass burning emissions (the dominant global source of absorbing aerosols), even the sign of their radiative forcing is uncertain (Bond et al., 2013; Kodros et al., 2015; Saleh et al., 2015). This dissertation investigates some key uncertainties regarding aerosol emissions from energy systems on climate. These include: incomplete inventories and uncertain representations of optical properties.

In addition to their impacts on climate, aerosols also cause substantial adverse health effects (Pope and Dockery, 2006; Di et al., 2017). Exposure to elevated levels of PM can lead to severe pulmonary and cardiovascular disease. For example, particle emissions from indoor cooking and heating is estimated to be responsible for more than 3 million deaths worldwide (WHO, 2014).

Anthropogenic aerosols are comprised of sulfates, nitrates, organics, and black carbon (BC). Except for BC, these aerosol components predominantly scatter radiation back to space (Charslon et al., 1992). However, particles that contain BC and brown carbon (BrC, which refer to light-absorbing organics) are potent light-absorbers. Major sources of absorbing particles are biomass burning, biofuel burning for indoor cooking (cookstoves) and heating, and on-road and off-road diesel engines (Andreae and Gelencsér, 2006; Bond et al., 2013; Saleh et al., 2013). BC is the most potent light-absorbing component of atmospheric aerosols, with a top of the atmosphere direct radiative forcing only second to CO_2 (IPCC, 2013). However, there is a large uncertainty in BC's total direct and indirect radiative forcings due to uncertain source emissions and optical properties and complex interactions with clouds (Bond et al., 2013). BC emissions inventories are likely incomplete (Bond et al., 2013). This dissertation focuses on two important sources of BC particles: biofuel combustion and vehicles.

There is growing evidence of the importance of biofuel emissions and their climate effects (Saleh et al. 2015; Kodros et al. 2015). Combustion of biofuels for residential heating and cooking (cookstoves) may contribute to 25% of BC emissions globally (Bond et al., 2013). Moreover, indoor cooking using inefficient stove designs often creates high PM levels and subsequent health impacts. To address this urgent problem, improved cookstoves with lower emissions and higher efficiencies are being deployed as cleaner alternatives to traditional designs.

There is a possibility of air quality and climate co-benefits from deploying these improved cookstoves. Improved cookstoves can reduce (sometimes only modestly) overall PM emissions compared to traditional ones (Roden et al., 2009; Coffey et al., 2017; Grieshop et al., 2017; Wathore et al., 2017). However, aerosol emissions from improved

cookstoves can contain a larger fraction of BC (MacCarty et al., 2008; Just et al., 2013; Grieshop et al., 2017). Hence, the large-scale deployment of improved cookstoves could have important adverse climate implications. In addition, there is significant variability in the emitted fraction of BC particles depending on operation (user, fuel, and burning conditions), and cookstove design (Jetter et al., 2012; Grieshop et al., 2017). This variability is expected given poorly controlled combustion conditions, but makes it hard to incorporate emissions in models for assessment of climate impacts from cookstoves. Therefore, we need to understand and explain the variability in emissions and optical properties to assess the global climate impacts from shifting cookstove technologies.

Vehicles are also undergoing technology transitions to meet newly promulgated emissions standards. The United States Corporate Average Fuel Economy (CAFE) standard was increased to 37.8 mpg starting 2016 (NHTSA, 2010), to reduce anthropogenic CO_2. To meet the new CAFE standard, car manufactures are deploying more gasoline direct injection (GDI) engines which offer higher fuel economy compared to the more widely used port fuel injection (PFI) engines (Zhao et al., 1999). The market share of GDI engines is rapidly increasing; 50% of gasoline vehicles sold in 2016 were equipped with a GDI engine, and their market share is expected to continue rising in the coming decade (Zhang and Mcmahon, 2012; Davis et al., 2015). However, changes in technology affects emissions. GDI engines have (1) higher BC emissions compared to PFI engines due to incomplete fuel volatilization and mixing in the combustion zone and (2) higher fraction of BC in emissions (Liang et al., 2013; Bahreini et al., 2015; Zimmerman et al., 2016). Increasing BC emissions from gasoline vehicles, due to shifting engine technology, will offset some of the climate benefits from improved fuel economy (decreased CO_2 emissions).

To assess the climate implications from the widespread adoption of GDI engines, we need emissions data from newly manufactured GDI vehicles; but these data are sparse (Zhang and Mcmahon, 2012; Bahreini et al., 2015). It is important to characterize emissions from recently manufactured GDI-equipped vehicles because GDI engine design (wall-guided versus spray-guided) and calibration are changing to meet the newly promulgated (Tier 3) Federal emission certifications. Changing engine technologies can change emission composition, which may in turn alter secondary PM and ozone formation with important health and climate implications (Odum et al., 1997; Kirchstetter et al., 1999; May et al., 2014; Jathar et al., 2016).

In addition to investigate two important source categories, this dissertation also investigates some key uncertainties associated with optical properties of aerosol emissions from combustion systems. Direct radiative forcing (DRF) of BC particles depends on the emissions rate, optical properties, and lifetime, each of which is uncertain. The optical properties of BC particles are often simplistically represented in climate models, potentially leading to poor model performance. For example, there is a factor of two discrepancy between satellite retrieved and model estimates of the BC radiative forcing (Chung et al., 2012; IPCC, 2013; Xu et al., 2016). Although this discrepancy can be accounted for by scaling up BC inventories (Bond et al., 2013), accounting for changes in morphology of the BC particles and for coating around the BC particles can also contribute to narrowing gap between measurements and models (Peng et al., 2016). BC particles is often mixed with non-BC material – so-called mixing state – depending on the source and atmospheric processing (Schwarz et al., 2008; Subramanian et al., 2010). This mixing creates coatings around a BC core which enhances BC's absorption properties (Schnaiter, 2005; Shiraiwa et al., 2010; Saliba et al., 2016), and therefore intensifies their warming

4

radiative impact (Jacobson, 2001; Ramanathan and Carmichael, 2008). Moreover, BC are fractal-like particles rendering their necessary radiative treatment more challenging (Sorensen, 2001). Changes in BC shape as a result of coating also affects their optical properties (Chakrabarty et al., 2007). However, variability in the BC mixing state and particle morphology are rarely accounted for in radiative models, which usually treat BC as spherical particles that are completely internally mixed with non-BC material, in a core-shell geometry (Jacobson, 2001; Kodros et al., 2015; Saleh et al., 2015).

Variability in the optical properties from source emissions are driven by variable combustion conditions. These changes ultimately can be linked to detailed changes in the BC mixing state and morphology. However, it is too computationally expensive to track these properties in climate models. Therefore, source-dependent parametrizations of optical properties as a function of performance metrics are needed. However, such parametrizations require comprehensive measurements of source operation. Such measurements are scarce for sources like cookstoves because field measurements have largely characterized PM and CO emissions (Roden et al., 2009; Coffey et al., 2017; Grieshop et al., 2017; Wathore et al., 2017), with many fewer studies measuring optical properties (Roden et al., 2006; Grieshop et al., 2017).

To understand the impact of aerosol emissions from energy systems on climate, we also need to understand their atmospheric evolution. After entering the atmosphere, BC particles evolve including changes their surface's chemical composition by oxidation and/or by addition of material via condensational growth (coating). Therefore, atmospheric processing affects both the optical properties of BC particles and their lifetime in the atmosphere through dry and wet deposition. This transformation happens on timescale of hours to days (Riemer et al., 2004; Moffet and Prather, 2009; Subramanian et al., 2010).

5

Fresh BC particles are usually poor CCNs (Weingartner et al., 1997), but atmospheric transformation increases their size and their hygroscopicity (affinity to water vapor) and transforms BC to more efficient CCNs (Kuwata et al., 2009). Condensational growth of BC particles (and other particles) depends on the condensate material, the seed, and supersaturation conditions (Seinfeld and Pandis, 2006), and is the chief driving force to growing ultrafine particles (< 100 nm) into CCN sizes (Riipinen et al., 2012).

Seed-dependent growth rates can have a direct impact on the survival probability of particles to grow to CCN sizes. However, climate models that account for particle growth do not differentiate growth rate based on seed composition. This is because atmospheric particles have a complex chemical composition (Jimenez and Canagaratna, 2009). The lack of direct measurements of growth rates from different particles means that we have limited knowledge of the role of seed and condensate material on their overall growth.

1.2 Objectives of Dissertation

The overarching goal of this dissertation is to quantify aerosol emissions from emerging energy technologies and to evaluate their potential climate impacts. We focus on two rapidly emerging technologies: improved cookstoves and gasoline direct injection (GDI) engines. We also developed parametrizations for the optical properties of fresh cookstove emissions to be used in climate models to assess the radiative impacts from stove emissions. Finally, we investigated how optical properties of these aerosol emission evolve in the atmosphere due to coating with condensable material.

The first objective of this dissertation is to assess the climate impacts of aerosol emissions from emerging energy technologies, improved cookstoves and gasoline direct injection (GDI) engines. We compared the radiative impacts of emissions from different

6

improved cookstove technologies, including wood-fueled rocket-style and gasifier cookstoves and charcoal-fueled cookstoves. Our estimates are based on newly developed parametrizations of optical properties from cookstove emissions combined with published emissions data. The parametrizations are derived from a large set of comprehensive emissions data collected as part of this work.

We also assessed the climate implications from the recent advent of GDI engines. We measured BC and CO_2 emission rates from a fleet of late-model GDI and PFI vehicles. We combined our new data with data collected as part of previous projects to create a database for 82 light-duty gasoline vehicles. All vehicles were tested using the cold-start Unified Cycle. The vehicles were equipped with GDI and PFI engine technologies and were certified to various emission standards (including the most stringent emission certifications). We used the data to assess the climate impacts of changing BC and CO_2 with transition from PFI and GDI equipped vehicles.

The second objective of this dissertation is to develop parametrizations of optical properties of aerosol emissions from cookstoves. We performed extensive laboratory measurements of intensive optical properties of aerosols emissions from several combinations of cookstove technologies and fuels. The tests were conducted using the newly developed firepower sweep protocol, which covers a wide range of operating conditions. We evaluated the role of stove technology, fuel, and performance metrics on the optical properties of the emissions. We used these to develop parametrizations for optical properties of cookstove emissions; the parameterizations are designed for use with existing emission inventories and atmospheric models. We evaluated the parametrizations with limited published data of optical properties from real-world cookstove emissions. We

also compared our new parametrizations against predictions from Mie theory (which assumes spherical particles and core-shell coated BC particles).

The third objective of this dissertation is to quantify the atmospheric evolution of aerosol emissions and their impact on optical properties. First, we evaluated the role of coating on the optical properties of BC particles. To that aim, we conducted experiments to measure absorption and scattering from nascent BC particles emitted from a rocket-style cookstove and coated with biogenic SOA. The measurements were then used to assess the performance of Mie and Rayleigh-Debye-Gans (RDG, simplest optical treatment of fractal-like particles) theories to predict the measured aerosol absorption and scattering from fresh and coated BC particles. To rigorously assess the performance of these models, the experiments featured: (1) size-selected nascent BC particles (2) a fully internal mixture of BC and non-BC materials (i.e., all coating material condensed on BC particles), and (3) non-absorbing coating material, to eliminate BrC contribution. This work addresses whether simple radiative formulations (such as Mie or RDG) can approximate the absorption and scattering of coated BC particles, under controlled laboratory conditions.

Second, we investigated the effects of aerosol seed composition (diesel and SOA particles) and gas-phase supersaturation on particle growth rate. Coating material around the BC particles affects their lifetime in the atmosphere. We conducted chamber experiments to compare the growth rates of two different seed particles simultaneously exposed to the same gas-phase supersaturation conditions. We investigated a range of growth rates, including typical atmospheric values.

1.3 Outline of Dissertation

In chapter 2, we present results from targeted experiments aimed at measuring absorption and scattering of atmospherically relevant BC particles emitted from a rocket-style improved cookstove and coated with SOA formed from the ozonolysis of alpha-pinene. The measurements are then used to evaluate the performance of Mie and RDG theories in predicting the radiative forcing of emissions from a rocket cookstove.

In chapter 3, we investigate the optical properties of fresh emissions from a wide range of cookstoves and operating conditions. The measurements are used to develop parametrizations for the mass absorption cross section (MAC, absorption per unit mass), the absorption angstrom exponent (AAE, the wavelength dependence of absorption) and the single scattering albedo (SSA, ratio of scattering to the sum of scattering and absorption). These parametrizations were combined with field emissions data to provide insight into the climate implications from several stove technologies. The proposed parametrizations are simple and fully describe the radiative properties of cookstove emissions; they can be used in climate models.

In chapter 4, we compare tailpipe emissions from PFI and GDI engines using data from 82 different light-duty gasoline vehicles tested on the cold-start Unified Cycle. We combined nealy collected gas- and particle-phase emissions data with published data from earlier projects to create a comprehensive database of vehicle emissions. The data were compared based on engine technology (PFI versus GDI) and emission certification. We used our comprehensive dataset of gas-phase emissions with the SAPRC-99 chemical mechanism to estimate the SOA and O_3 formation potentials (which have climate and health implications) from different engine technologies. Finally, climate implications from

switching engine technology are assessed using data for BC and CO_2 emission rates coupled with a Monte-Carlo simulation.

In chapter 5, we present results from experiments that investigated the particle seed composition on particle growth rates. We used diesel exhaust and biogenic SOA particles (formed from the ozonolysis of alpha-pinene) as the two seed particles. We coated the particles with alpha-pinene SOA and squalane as condensate materials. We combined measured growth rates with a condensational growth theoretical model to quantify the role of particle composition and supersaturation on particle growth rates.

Finally, chapter 6 summarizes the key findings of this dissertation and discusses future work.

1.4 References

Andreae, M. O.; Gelencsér, A. Black Carbon or Brown Carbon? The Nature of Light-Absorbing Carbonaceous Aerosols. *Atmos. Chem. Phys.* **2006**, *6* (3), 3419–3463.

Bahreini, R.; Xue, J.; Johnson, K.; Durbin, T.; Quiros, D.; Hu, S.; Huai, T.; Ayala, A.; Jung, H. Characterizing Emissions and Optical Properties of Particulate Matter from PFI and GDI Light-Duty Gasoline Vehicles. *J. Aerosol Sci.* **2015**, *90*, 144–153.

Bond, T. C.; Doherty, S. J.; Fahey, D. W.; Forster, P. M.; Berntsen, T.; DeAngelo, B. J.; Flanner, M. G.; Ghan, S.; Kärcher, B.; Koch, D.; et al. Bounding the Role of Black Carbon in the Climate System: A Scientific Assessment. *J. Geophys. Res. Atmos.* **2013**, *118* (11), 5380–5552.

Chakrabarty, R. K.; Moosmüller, H.; Arnott, W. P.; Garro, M. a; Slowik, J. G.; Cross, E. S.; Han, J.-H.; Davidovits, P.; Onasch, T. B.; Worsnop, D. R. Light Scattering and Absorption by Fractal-like Carbonaceous Chain Aggregates: Comparison of Theories and Experiment. *Appl. Opt.* **2007**, *46*, 6990–7006.

Charlson, R. J.; Schwartz, S. E.; Hales, J. M.; Cess, R. D.; Coakley, J. A.; Hansen, J. E.; Hofmann, D. J. Climate Forcing by Anthropogenic Aerosols. *Science (80-.).* **1992**, *255* (5043), 423–430.

Chung, C. E.; Ramanathan, V.; Decremer, D. Observationally Constrained Estimates of Carbonaceous Aerosol Radiative Forcing. *Proc. Natl. Acad. Sci. U. S. A.* **2012**, *109* (29), 11624–11629.

Coffey, E. R.; Muvandimwe, D.; Hagar, Y.; Wiedinmyer, C.; Kanyomse, E.; Piedrahita, R.; Dickinson, K. L.; Oduro, A.; Hannigan, M. P. Implications of New Emission Factors and Efficiencies from in-Field Measurements of Traditional and Improved Cookstoves. *Environ* **2017**.

Di, Q.; Wang, Y.; Zanobetti, A.; Wang, Y.; Koutrakis, P.; Choirat, C.; Dominici, F.; Schwartz, J. D. Air Pollution and Mortality in the Medicare Population. *N. Engl. J. Med.* **2017**, *376* (26), 2513–2522.

Feng, Y.; Ramanathan, V.; Kotamarthi, V. R. Brown Carbon: A Significant Atmospheric Absorber of Solar Radiation? *Atmos. Chem. Phys.* **2013**, *13* (17), 8607–8621.

Grieshop, A. P.; Jain, G.; Sethuraman, K.; Marshall, J. D. Emission Factors of Health- and Climate-Relevant Pollutants Measured in Home during a Carbon-Finance-Approved Cookstove Intervention in Rural India. *GeoHealth* **2017**, *1* (5), 222–236.

IPCC Working Group 1, I.; Stocker, T. F.; Qin, D.; Plattner, G.-K.; Tignor, M.; Allen, S. K.; Boschung, J.; Nauels, A.; Xia, Y.; Bex, V.; et al. IPCC, 2013: Climate Change 2013: The Physical Science Basis. Contribution of Working Group I to the Fifth Assessment Report of the Intergovernmental Panel on Climate Change. *IPCC* **2013**, *AR5*, 1535.

Jacobson, M. Z. Strong Radiative Heating due to the Mixing State of Black Carbon in Atmospheric Aerosols. *Nature* **2001**, *409*, 695–697.

Jathar, S. H.; Woody, M.; Pye, H. O. T.; Baker, K. R.; Robinson, A. L. Chemical Transport Model Simulations of Organic Aerosol in Southern California: Model Evaluation and Gasoline and Diesel Source Contributions. *Atmos. Chem. Phys. Discuss.* **2016**, No. December, 1–18.

Jetter, J.; Zhao, Y.; Smith, K. R.; Khan, B.; Decarlo, P.; Hays, M. D.; Drive, P.; Carolina, N.; States, U. Pollutant Emissions and Energy E Ffi Ciency under Controlled Conditions for Household Biomass Cookstoves and Implications for Metrics Useful in Setting International Test Standards. *Environ. Sci. Technol.* **2012**.

Jimenez, J.; Canagaratna, M. Evolution of Organic Aerosols in the Atmosphere. *Science (80-.).* **2009**, *326* (5959), 1525–1529.

Just, B.; Rogak, S.; Kandlikar, M. Characterization of Ultrafine Particulate Matter from

Traditional and Improved Biomass Cookstoves. *Environ. Sci. Technol.* **2013**, *47* (7), 3506–3512.

Kirchstetter, T. W.; Singer, B. C.; Harley, R. A.; Kendall, G. R.; Hesson, J. M. Impact of California Reformulated Gasoline on Motor Vehicle Emissions. 2. Volatile Organic Compound Speciation and Reactivity. *Environ. Sci. Technol.* **1999**, *33* (2), 329–336.

Kodros, J. K.; Scott, C. E.; Farina, S. C.; Lee, Y. H.; L'Orange, C.; Volckens, J.; Pierce, J. R. Uncertainties in Global Aerosols and Climate Effects due to Biofuel Emissions. *Atmos. Chem. Phys.* **2015**, *15* (15), 8577–8596.

Kuwata, M.; Kondo, Y.; Takegawa, N. Critical Condensed Mass for Activation of Black Carbon as Cloud Condensation Nuclei in Tokyo. *J. Geophys. Res. Atmos.* **2009**, *114* (20).

Liang, B.; Ge, Y.; Tan, J.; Han, X.; Gao, L.; Hao, L.; Ye, W.; Dai, P. Comparison of PM Emissions from a Gasoline Direct Injected (GDI) Vehicle and a Port Fuel Injected (PFI) Vehicle Measured by Electrical Low Pressure Impactor (ELPI) with Two Fuels: Gasoline and M15 Methanol Gasoline. *J. Aerosol Sci.* **2013**, *57*, 22–31.

Lohmann, U.; Lesins, G. Stronger Constraints on the Anthropogenic Indirect Aerosol Effect. *Science (80-.).* **2002**, *298* (5595), 1012–1015.

MacCarty, N.; Ogle, D.; Still, D.; Bond, T.; Roden, C. A Laboratory Comparison of the Global Warming Impact of Five Major Types of Biomass Cooking Stoves. *Energy Sustain. Dev.* **2008**, *12* (2), 56–65.

May, A. A.; Nguyen, N. T.; Presto, A. A.; Gordon, T. D.; Lipsky, E. M.; Karve, M.; Gutierrez, A.; Robertson, W. H.; Zhang, M.; Brandow, C.; et al. Gas- and Particle-Phase Primary Emissions from in-Use, on-Road Gasoline and Diesel Vehicles. *Atmos. Environ.* **2014**, *88*, 247–260.

Moffet, R. C.; Prather, K. a. In-Situ Measurements of the Mixing State and Optical Properties of Soot with Implications for Radiative Forcing Estimates. *Proc. Natl. Acad. Sci. U. S. A.* **2009**, *106*, 11872–11877.

NHTSA. *United States Department of Transportation, CORPORATE AVERAGE FUEL ECONOMY FOR MY 2011-2015 PASSENGER CARS and LIGHT TRUCKS*; 2010.

Odum, J. R.; Jungkamp, T. P.; Griffin, R. J.; Flagan, R. C.; Seinfeld, J. H. The Atmospheric Aerosol-Forming Potential of Whole Gasoline Vapor. *Science* **1997**, *276* (5309), 96–99.

Peng, J.; Hu, M.; Guo, S.; Du, Z.; Zheng, J.; Shang, D.; Levy Zamora, M.; Zeng, L.; Shao, M.; Wu, Y.-S.; et al. Markedly Enhanced Absorption and Direct Radiative Forcing of Black

Carbon under Polluted Urban Environments. *Proc. Natl. Acad. Sci.* **2016**, *113* (16), 4266–4271.

Pope, C. A.; Dockery, D. W. Health Effects of Fine Particulate Air Pollution: Lines That Connect. *J. Air Waste Manage. Assoc.* **2006**, *56* (6), 709–742.

Ramanathan, V.; Carmichael, G. Global and Regional Climate Changes due to Black Carbon. *Nature Geoscience*. 2008, pp 221–227.

Riemer, N.; Vogel, H.; Vogel, B. Soot Aging Time Scales in Polluted Regions during Day and Night. *Atmospheric Chemistry and Physics*. 2004, pp 1885–1893.

Riipinen, I.; Yli-Juuti, T.; Pierce, J. R.; Petäjä, T.; Worsnop, D. R.; Kulmala, M.; Donahue, N. M. The Contribution of Organics to Atmospheric Nanoparticle Growth. *Nat. Geosci.* **2012**, *5* (7), 453–458.

Roden, C. A.; Bond, T. C.; Conway, S.; Osorto Pinel, A. B. Emission Factors and Real-Time Optical Properties of Particles Emitted from Traditional Wood Burning Cookstoves. *Environ. Sci. Technol.* **2006**, *40*, 6750–6757.

Roden, C. A.; Bond, T. C.; Conway, S.; Osorto Pinel, A. B.; MacCarty, N.; Still, D. Laboratory and Field Investigations of Particulate and Carbon Monoxide Emissions from Traditional and Improved Cookstoves. *Atmos. Environ.* **2009**, *43* (6), 1170–1181.

Rosenfeld, D. Aerosol-Cloud Interactions Control of Earth Radiation and Latent Heat Release Budgets. *Space Sci. Rev.* **2006**, *125* (1–4), 149–157.

Saleh, R., M. Marks, J. Heo, P.J.Adams, N.M. Donahue, A. L. R. Contribution of Brown Carbon and Lensing to the Direct Radiative Effect of Carbonaceous Aerosols from Biomass and Biofuel Burning Emissions. *J. Geophys. Res. Atmos.* **2015**, 1–12.

Saleh, R.; Hennigan, C. J.; McMeeking, G. R.; Chuang, W. K.; Robinson, E. S.; Coe, H.; Donahue, N. M.; Robinson, a. L. Absorptivity of Brown Carbon in Fresh and Photo-Chemically Aged Biomass-Burning Emissions. *Atmos. Chem. Phys.* **2013**, *13* (15), 7683–7693.

Saliba, G.; Subramanian, R.; Saleh, R.; Ahern, A. T.; Lipsky, E. M.; Tasoglou, A.; Sullivan, R. C.; Bhandari, J.; Mazzoleni, C.; Robinson, A. L. Optical Properties of Black Carbon in Cookstove Emissions Coated with Secondary Organic Aerosols: Measurements and Modeling. *Aerosol Sci. Technol.* **2016**, *50* (11), 1–13.

Schnaiter, M. Absorption Amplification of Black Carbon Internally Mixed with Secondary Organic Aerosol. *J. Geophys. Res.* **2005**, *110* (D19), D19204.

Schwarz, J. P.; Gao, R. S.; Spackman, J. R.; Watts, L. A.; Thomson, D. S.; Fahey, D. W.; Ryerson, T. B.; Peischl, J.; Holloway, J. S.; Trainer, M.; et al. Measurement of the Mixing State, Mass, and Optical Size of Individual Black Carbon Particles in Urban and Biomass Burning Emissions. *Geophys. Res. Lett.* **2008**, *35* (13), 1–5.

Seinfeld, J. H.; Pandis, S. N. *Atmospheric Chemistry and Physics: From Air Pollution to Climate Change*; 2006.

Shiraiwa, M.; Kondo, Y.; Iwamoto, T.; Kita, K. Amplification of Light Absorption of Black Carbon by Organic Coating. *Aerosol Sci. Technol.* **2010**, *44* (1), 46–54.

Sorensen, C. M. Light Scattering by Fractal Aggregates: A Review. *Aerosol Sci. Technol.* **2001**, *35*, 648–687.

Stacy C. Davis; Susan E. Williams; Robert G. Boundy; Sheila Moore. *2015 Vehicle Technologies Market Report*; 2015.

Subramanian, R.; Kok, G. L.; Baumgardner, D.; Clarke, A.; Shinozuka, Y.; Campos, T. L.; Heizer, C. G.; Stephens, B. B. Black Carbon over Mexico: The Effect of Atmospheric Transport on Mixing State, Mass Absorption Cross-Section, and BC/CO Ratios. *Atmospheric Chemistry and Physics*. **2010**, *10*(1).

Twomey, S. The Influence of Pollution on the Shortwave Albedo of Clouds. *J. Atmos. Sci.* **1977**, *34* (7), 1149–1152.

Wathore, R.; Mortimer, K.; Grieshop, A. P. In-Use Emissions and Estimated Impacts of Traditional, Natural- and Forced-Draft Cookstoves in Rural Malawi. *Environ. Sci. Technol.* **2017**, *51* (3), 1929–1938.

Weingartner, E.; Burtscher, H.; Baltensperger, U. Hygroscopic Properties of Carbon and Diesel Soot Particles. *Atmos. Environ.* **1997**, *31* (15), 2311–2327.

Xu, Y.; Ramanathan, V.; Washington, W. M. Observed High-Altitude Warming and Snow Cover Retreat over Tibet and the Himalayas Enhanced by Black Carbon Aerosols. *Atmos. Chem. Phys.* **2016**, *16* (3), 1303–1315.

Zhang, S.; Mcmahon, W. Particulate Emissions for LEV II Light-Duty Gasoline Direct Injection Vehicles. *SAE Int. J. Fuels Lubr.* **2012**, *5* (2).

Zhao, F.; Lai, M. C.; Harrington, D. L. Automotive Spark-Ignited Direct-Injection Gasoline Engines. *Prog. Energy Combust. Sci.* **1999**, *25* (5), 437–562.

Zimmerman, N.; Wang, J. M.; Jeong, C.-H.; Ramos, M.; Hilker, N.; Healy, R. M.; Sabaliauskas, K.; Wallace, J. S.; Evans, G. J. Field Measurements of Gasoline Direct

Injection Emission Factors: Spatial and Seasonal Variability. *Environ. Sci. Technol.* **2016**, *50* (4), 2035–2043.

CHAPTER 2

OPTICAL PROPERTIES OF BLACK CARBON IN COOKSTOVE EMISSIONS COATED WITH SECONDARY ORGANIC AEROSOLS: MEASUREMENTS AND MODELING[1]

Abstract

Cookstoves are a major source of black carbon particles (BC) and associated organic compounds, which influence the atmospheric radiative balance. We present results from experiments that characterize BC emissions from a rocket stove coated with secondary organic aerosol. Optical properties, namely BC mass absorption cross section (MAC_{BC}) and mass scattering cross section (MSC), as a function of the organic-to-black carbon ratio (OA:BC) of fresh and aged cookstove emissions were compared with Mie and Rayleigh-Debye-Gans (RDG) calculations. Mie theory reproduced the measured MAC_{BC} across the entire OA:BC range. However, Mie theory failed to capture the MSC at low OA:BC, where the data agreed better with RDG, consistent with a fractal morphology of fresh BC aggregates. As the OA:BC increased, the MSC approached Mie predictions indicating that BC-containing particles approach a core-shell structure as BC cores become heavily coated. To gain insight into the implications of our findings, we calculated the spectral simple forcing efficiency (dSFE) using measured and modeled optical properties as inputs. Good agreement between dSFE estimates calculated from measurements and Mie-modeled dSFE across the entire OA:BC range, suggests that Mie theory can be used to simulate the optical properties of aged cookstove emissions.

2.1 Introduction

Combustion of biofuels for residential heating and cooking (cookstoves) contributes around 20% of both BC and primary organic aerosols emissions globally (Bond et al. 2013), with wide variability in total emissions of stoves depending on operation (user, fuel, and burning conditions), and design. Previous studies report data for emissions (Jetter et al. 2012; Just et al. 2013), optical properties (Preble et al. 2014; Chen et al. 2012), and climate implication (MacCarty et al. 2008) of fresh emissions from a variety of stove designs. Some "improved stoves" show lower PM emissions than the traditional three-stone fire (Adkins et al. 2010; Preble et al. 2014), though the reduced PM emissions may be relatively BC-rich (Preble et al. 2014). However, less work has examined the optical properties of aged cookstove emissions. The evidence for BC-rich PM emissions from improved cookstoves warrants the need for more study of these BC emitters.

The rocket stove is an "improved" stove design with lower overall PM emissions but relatively higher BC emission (Just et al. 2013), which can lead to stronger positive radiative forcing (Jacobson 2001; Ramanathan & Carmichael 2008; Bond et al. 2013). The improved efficiency is due to their small and insulated chimney (acting as the combustion chamber) and to the natural air draft through the chamber.

There is growing evidence of the importance of biofuel emissions and more specifically "improved" cookstove emissions and their climate effects (Wilson et al. 2016; Kodros et al. 2015; Saleh et al. 2015). However, there is substantial uncertainty associated with this effect partly due to the poorly constrained mixing state (the degree to which non-BC material is mixed with BC particles, the two extremes being homogeneous internal and an external mixture) and morphology (structure of the particles) of emitted BC particles as they age in the atmosphere. The initial morphology of BC aggregates is determined by the

combustion process; and then evolve in the atmosphere as BC particles mix with other components, which occurs on the time scale of hours or days after emissions (Riemer et al. 2004; Moffet & Prather 2009; Subramanian et al. 2010; Moteki et al. 2007; China et al. 2013). The presence of a coating can alter the morphology of a BC aggregate on the one hand by causing it to collapse (Reid & Hobbs 1998; Zhang et al. 2008; Cross et al. 2010; China et al. 2013), and increase the absorption efficiency of BC on the other hand, a phenomenon often referred to as lensing (Fuller 1995; Fuller et al. 1999; Lack & Cappa 2010). This absorption enhancement has been observed in field studies (Wang et al. 2014) as well as various laboratory studies for coated diesel and laboratory-generated BC aggregates (Schnaiter 2005; Zhang et al. 2008; Lack et al. 2009; Shiraiwa et al. 2010; Cross et al. 2010) though lensing from coated BC particles emitted from cookstoves has not been extensively investigated. However, the field measurements of urban aged BC particles by Cappa et al. (2012) showed negligible absorption enhancement, which was attributed to BC residing on the edge of the particles leading to minimal lensing effect (Fuller et al. 1999; Adachi et al. 2010; Sedlacek et al. 2012; Liu et al. 2015).

Even if the BC particle morphology is well constrained, computing exact electromagnetic solutions of optical properties for fractal aggregates is too computationally expensive to be incorporated into global radiative transfer models. Consequently, treatments of light-absorbing aerosols in radiative transfer models have been mostly based on Mie theory (Jacobson 2000; Jacobson 2001; Jacobson 2010; Feng et al. 2013; Saleh et al. 2015; Kodros et al. 2015), which assume that BC is compacted into homogeneous spheres coated with non-BC components in a core-shell morphology, or by applying a constant enhancement factor (Wang et al. 2014). However, these assumptions can lead to overestimation of absorption by BC (Fuller 1995; Fuller et al. 1999; Sorensen 2001; Adachi

18

et al. 2010; China et al. 2013; Scarnato et al. 2013). Another theoretical framework that could potentially capture the fractal nature of BC particles is the Rayleigh-Debye-Gans (RDG) model (Sorensen 2001; Chakrabarty et al. 2007), however its performance on coated BC particles has not been extensively reported in the literature.

Comparing measured optical properties with model predictions (such as Mie theory) provides a way to evaluate the applicability of either Mie theory or RDG in a modeling framework to determine atmospheric radiative impacts of cookstove emissions as they are emitted and then aged during atmospheric transformation. In this study, we measured optical properties, namely light-absorption and scattering coefficients, of fresh BC particles, emitted from a rocket stove, and subsequently coated with secondary organic aerosols (SOA) from the photo-oxidative ozonolysis of α-pinene. Unlike previous studies, we use measured BC core sizes as input to the Mie and RDG models; thus, the model results are independent of, and not forced to fit, the experimentally-observed optical properties. We then compare mass scattering cross section (MSC) and BC mass absorption cross section (MAC_{BC}) to predictions by both Mie and RDG models as the particles age and are coated with SOA. Finally, we examine the radiative impacts of cookstove emissions using the simple forcing efficiency.

2.2 Methods

Several studies have previously investigated BC coating process, but they either use flame-generated soot or other BC proxies (Lack et al. 2006; Cross et al. 2010; Shiraiwa et al. 2010) which may not be representative of cookstove emissions, and/or did not use advanced instruments for *in-situ* measurements of BC core size and optical properties which have become available only in the last few years (Schnaiter 2005). We investigated

the optical properties of fresh BC aggregates, emitted from a commercially available rocket stove (EnviroFit G-3300) using European White birch bark as a fuel. This work uses a more atmospherically relevant system (actual cookstove emissions) as a source of BC particles compared to other studies that have used other BC proxies. The use of a more complex fuel (wood bark) and nearly uncontrolled combustion conditions inside the cookstove, we believe, should produce more representative BC particles. Although emissions from the rocket stove may have varied substantially between experiments, in this study we were concerned with the characterization of intensive optical properties and not total emissions.

The experiments were conducted with size selected BC particles to simplify model calculations by constraining the mass distributions. This allowed us to systematically vary core sizes and coating thicknesses, thus allowing for a relatively direct comparison with Mie theory. To focus on BC emissions from cookstoves, we used pieces of European White Birch bark pieces (typically 1-2'' wide and a few inches long), which was experimentally found to produce sustained flaming combustion with BC-rich PM emissions (unlike the non-bark components of the fire wood). After characterization of the fresh emissions, the particles were then coated with secondary organic aerosol (SOA) formed from the photo-oxidative ozonolysis of α-pinene in a smog chamber.

We compared measured optical properties to model predictions (Mie and RDG) using an ensemble parameter: the total internally mixed organic aerosol to BC mass ratio (OA:BC), a measure of coating thickness. We chose the OA:BC ratio instead of the shell/core ratio (Bond et al. 2006) because it is trackable in climate models and is independent of the assumption of a core-shell particle morphology. The OA:BC ratio in

this study is also a surrogate for the non-BC to BC ratio in ambient aerosol where the non-BC material includes sulfates, nitrates, organic matter, and water.

2.2.1 Particle Generation and Coating

Figure 2.1 shows a schematic of the experimental setup. The rocket stove emissions were sampled using a diaphragm pump through an activated carbon denuder to reduce the co-emitted volatile organic compounds. Although there are some particle losses in the pump, this study characterizes intensive optical properties and not absolute emission rates. The emissions then passed through a DMA (Model 3080 TSI, Inc., Shoreview, MN, USA) used for size selection and into a $2m^3$ Teflon chamber. Experiments were performed with three different BC mobility diameters of: 140 nm (experiment 1), 210 nm (experiment 2), and 180 nm (experiment 3). Size distributions inside the chamber were measured using a Scanning Mobility Particle Sizer (SMPS, TSI, Inc., 3080/3771). Figure 2.2 shows a typical SMPS size distribution of fresh emissions, for experiment 1.
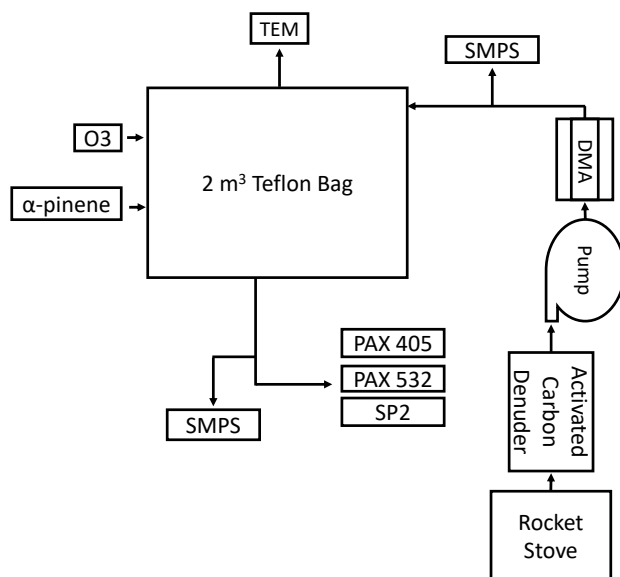
Figure 2.1 Experimental setup. TEM samples were taken from a separate set of experiments and are shown here for reference only.

After characterizing the fresh emissions in the chamber, we initiated SOA formation via the reaction of α-pinene with ozone (around 300 ppb) as well as photo-oxidation using UV lights following established procedures of (Presto et al. 2005; Presto & Donahue 2006). The OA:BC ratio (and thus coating thickness) was increased incrementally by sequentially injecting additional α-pinene into the chamber in a stepwise fashion.

We chose α-pinene SOA primarily due to its non-light absorptive properties (Schnaiter 2005), which enables us to reduce modeling complexity by focusing on lensing rather than effects such as brown carbon (Andreae & Gelencsér 2006; Saleh et al. 2014; Chakrabarty et al. 2016).

2.2.2 Absorption and Scattering Coefficients

Absorption and scattering coefficients were measured using two Photo-Acoustic Extinctiometers (PAX, Droplet Measurement Technologies) operating at wavelengths of

405 nm and 532 nm (Arnott et al. 1999). Scattering and absorption measurements of both PAXs were calibrated using PSL spheres and fullerene soot respectively. Briefly, scattering calibration was performed by nebulizing a high concentration of non-absorbing PSL spheres and comparing measured scattering coefficients with extinction coefficients calculated from the drop-in laser power within the extinctiometer cell. Absorption calibration was performed by nebulizing fullerene soot particles and comparing measured absorption coefficients with the difference between calculated extinction coefficients and calibrated scattering coefficients (Arnott et al. 2000; Sharma et al. 2013). Using fullerene soot instead of NO_2 gas for absorption calibration does not require accounting for NO_2 photo-dissociation, which occurs at wavelengths below ~ 420 nm (Roehl et al. 1994; Sharma et al. 2013; Arnott et al. 2000).

2.2.3 BC Mass and Size Distribution Measurements

We measured refractory BC (rBC) mass and size distributions using a Single Particle Soot Photometer (SP2, Droplet Measurement Technologies) (Schwarz et al. 2006; Moteki & Kondo 2010; Subramanian et al. 2010), which was calibrated using Fullerene soot (Gysel et al. 2011). The calibration was verified with targeted experiments using a Centrifugal Particle Mass Analyzer (CPMA, Cambustion) (Olfert & Collings 2005). Good agreement between the SP2 rBC mode mass and the CPMA mode mass was observed as shown in Figure S1 in the SI with a linear regression slope of 1.1 (R^2 = 0.99). For typical initial chamber concentrations of around 2,000 #/cm^3 we expect coincidence errors inside the SP2 to be negligible, and this was verified using the code from Holder et al. (2014) (Figure S2 in the SI).

2.2.4 Estimating Organic Mass of BC-containing Aerosols

To determine the mass scattering cross-section and the OA:BC ratio of each experiment, we need the organic aerosol mass of BC-containing aerosols. This OA mass was estimated based on the difference between the total mass concentrations, inferred from SMPS measurements, and the BC mass concentrations from SP2 measurements. The challenge is that the SMPS measures electrical mobility diameter, and thus the inferred mass concentrations are sensitive to particle morphology. We consider two limiting cases to constrain the OA mass concentrations, and report the OA mass and the resulting OA:BC ratio as the average of these two cases (the two bounds are shown as error bars in Figures 2.4, 2.5, and 2.6 and measurement uncertainty of OA mass is discussed in section 7 in the SI). These cases provide conservative bounds of the true OA:BC ratio.
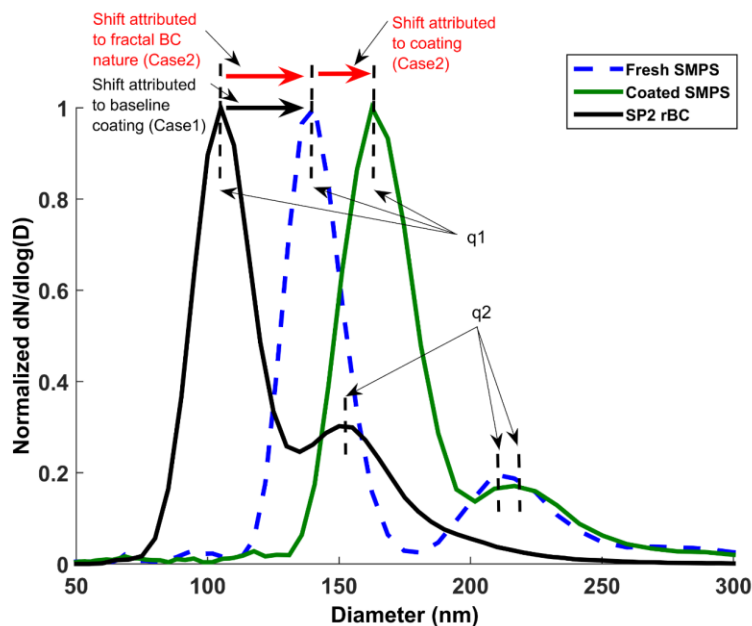
Figure 2.2 Normalized size distribution of rBC (SP2, black line), fresh SMPS (dashed blue line) and SMPS after first coating (green line) for experiment 1. The main peaks in all distributions are singly charged (q1) particles and the second peaks on the right are doubly charged (q2) particles. For Case 1 OA mass calculations, any difference between the SP2 and SMPS distributions is attributed to non-BC coating. For Case 2 OA mass calculations, fresh emissions are assumed to consist only of BC particles with a mobility size distribution equal to the fresh SMPS distribution, hence the difference between fresh SMPS and coated SMPS distributions is attributed to coating.

In the first case (referred to as case 1) we assume that nascent BC particles are spherical and void-free, with a material density of ρ_{BC}^{mat}=1.8 g.cm^{-3} (Bond & Bergstrom 2006). Consequently, any difference between SMPS and SP2 size distributions is solely attributed to coating (Figure 2.2). Case 1 minimizes the contribution of BC to the total volume measured by the SMPS and thus represents the upper limit on chamber OA mass concentrations. We therefore, can simply compute the OA mass concentration by subtracting the total rBC volume ($V_{rBC}(t) = \frac{m_{rBC}(t)}{\rho_{BC}^{mat}}$) from the total SMPS volume and multiplying the difference by the OA material density assumed to be ρ_{OA}=1.2 g.cm^{-3}.

$$m_{OA}^{case1}(t) = \rho_{OA} \left(\sum \frac{\pi}{6} d_{mob}^3 dN_i(t) - \frac{m_{rBC}(t)}{\rho_{BC}^{mat}} \right) \tag{2.1}$$

Case 2 represents the lower limit on OA mass concentrations by maximizing the potential contribution of BC particles to the total volume measured by the SMPS. We assume that BC particles are spherical with a diameter equal to the mobility diameter obtained from the SMPS size distribution of the fresh emissions, i.e., we assume that fresh emissions consist solely of BC. We also assume that BC particles do not restructure as a result of coating (i.e., the effective density of BC particles remains constant and does not increase due to compaction during later coating events). Then, the difference between the SP2 and SMPS size distributions for fresh emissions is only due to the fractal nature of BC aggregates (Figure 2.2). We constrain the BC effective density (ρ_{BC}^{eff}) as (DeCarlo & Slowik 2004),

$$\rho_{BC}^{eff} = \frac{m_{rBC}}{V_{fresh}^{SMPS}} < \frac{m_{rBC}}{V_{fresh}^{BC}} = \rho_{BC}^{eff,true} \tag{2.2}$$

We then calculate the OA mass concentrations during subsequent SOA coating events by subtracting the rBC volume ($V_{rBC}(t) = \frac{m_{rBC}(t)}{\rho_{BC}^{eff}}$) from the total SMPS particle volume and multiplying the difference by the OA material density.

$$m_{OA}^{case2}(t) = \rho_{OA}\left(\sum \frac{\pi}{6}d_{mob}^3 dN_i(t) - \frac{m_{rBC}(t)}{\rho_{BC}^{eff}}\right) \tag{2.3}$$

Case 2 $V_{rBC}(t)$ is equal to the wall-loss uncorrected fresh SMPS volume. We wrote Equation 2.3 in terms of $V_{rBC}(t)$ and not V_{fresh}^{SMPS} because we use the total measured SMPS particle volume at later times which is not wall-loss corrected. As BC particles are coated by sequential α–pinene injections, imbalances in capillary forces can cause the BC aggregate to collapse to create a more spherical and compacted geometry as found also in the atmosphere, due to the condensation of different materials, including water (Schnaiter 2005; Cross et al. 2010; Schnitzler et al. 2014). Thus, true chamber OA:BC will always be smaller than, but will converge towards, the OA:BC calculated using case 1, if collapse of the BC aggregates were to occur.

2.2.5 Optical Properties from Measurements

The absorption and scattering efficiencies of cookstove emissions were quantified as MAC_{BC} and MSC ($m^2.g^{-1}$). MAC_{BC} is the absorption cross section per unit BC mass; the MSC is the scattering cross section per unit total mass. We calculated MAC_{BC} and MSC as the ratio of the PAX absorption (b_{abs}) and scattering (b_{scat}) to the SP2 rBC mass and the average (from case 1 and case 2) SMPS volume-based total mass, respectively. Measurement uncertainties of both MAC_{BC} and MSC are discussed in section 7 in the SI.

$$MAC_{BC} = \frac{b_{abs}}{m_{rBC}}, \quad MSC = \frac{b_{scat}}{m_{tot}} \tag{2.4}$$

2.3 Theoretical Calculations

2.3.1 Mie Theory

Mie theory assumes that the BC core and non-BC coating have a core-shell morphology of isotropic concentric spheres (Bohren & Huffman 1983). In this study, we used a Mie model based on the formulation of Bohren and Huffman (1983) to calculate optical properties at two wavelengths: 405 nm and 532 nm. Inputs for Mie calculations are: 1) the core (BC) size distribution (SP2), 2) the shell diameter for every core size (i.e., the coated distribution). 3) the core (BC) refractive index $n_{BC} = 1.95 - 0.79i$, which represents BC with little or no voids (Bond & Bergstrom 2006). Mie calculations are performed independently of the two cases presented in section 2.2.4, and the use of the BC "void-free" refractive index is justified because we use as input to Mie calculations the SP2-based BC mass-equivalent number distributions (which assume a bulk density of 1.8 g.cm^{-3} closer to void-free BC). 4) the shell refractive index assumed to be $n_{shell} = 1.5 - 0i$, i.e., a non-absorbing shell (Schnaiter 2005).

To model optical properties (MAC$_{BC}$ and MSC) as a function of the OA:BC ratio, we need to compute the coated number distribution at every OA:BC ratio. To do this, we calculate the shell diameter ($d_{shell,i}$) for every core diameter in the SP2 distribution ($d_{BC,i}$) assuming complete internal mixture, a BC material density of 1.8 g.cm^{-3}, and an OA material density of 1.2 g.cm^{-3},

$$d_{shell,i} = d_{BC,i} \cdot \sqrt[3]{\left(\frac{\rho_{BC}^{mat}}{\rho_{OA}} \cdot \frac{OA}{BC} + 1\right)} \tag{2.5}$$

2.3.2 Rayleigh-Debye-Gans (RDG) Theory

RDG assumes that each monomer in the aggregate interacts independently with radiation, by neglecting multiple scattering and shadowing (Farias et al. 1996; Sorensen 2001; Moosmüller & Arnott 2009). Absorption is an incoherent process and as a result the absorption of the aggregate is equal to the number of monomers, N, times the absorption of a single monomer. Consequently, MAC_{BC}^{agg} of the aggregate is equal to MAC_{BC}^{m} of a single monomer and the mass absorption cross section of a fractal like aggregate is independent of the aggregate size.

Transmission Electron Microscopy (TEM) imaging suggests that the fresh soot emissions are composed of primary spherules with a diameter of 33.2 ± 5.4 nm (average ± standard deviation, see section 3 in the SI for more information). Hence, we use a simplified RDG treatment by assuming that: 1) the monomers scatter in the Rayleigh regime, i.e., have a size parameter, x_m, small compared to unity ($x_m \ll 1$) and 2) the structure factor of the BC aggregate is unity (Sorensen 2001). This implies that scattering of the aggregate is independent of the exact arrangement of the monomers in the aggregate and is equal to N^2 times scattering of a single monomer. For RDG model to be a viable alternative to Mie theory in climate calculations, RDG scattering calculations need to be treated in this or another simplified form since the detailed treatment requires knowledge of the structure factor of the BC aggregates which is not available for large scale climate calculations.

As the coating thickness around the monomer increases, the Rayleigh scattering assumption, thus RDG, breaks down. Also, as the size of the aggregate increases, monomer interactions become more prevalent and the central assumptions that all monomers scatter in-phase becomes less robust. However, during our experiments the highest measured OA:BC was less than 10, for which the coated monomer size parameter, x_m, is 0.46 at 532

nm. Previous comparison of RDG with more exact numerical solutions have reported that the error associated in treating the monomer as scattering in the Rayleigh regime, for $x_m <$ 0.3, is small for coated monomers with a clear coating, and RDG may still be applicable even up to $x_m < 0.5$ (Farias et al. 1996).

RDG calculations were performed using the Mie code based on the formulation of Bohren & Huffman (1983) and using the same input parameters (refractive indices of both the core and the shell) as Mie calculations (section 2.3.1) with the exception of the BC core distribution, which is replaced with the mode monomer diameter (d_m) from TEM measurements. MSC is proportional to the number of monomers (N) forming the BC aggregate, thus RDG modeling of the MSC requires the input of N for each experiment. The total number of monomers, N, is calculated by dividing the BC aggregate mass (from SP2) by the mass of a single monomer. We calculate an average number of monomer per aggregate, N, of 30, 60, and 100 for experiments 1, 2, and 3 respectively.

2.4 Results and Discussions

Figure 2.3 shows the results from a typical experiment, with time series of absorption coefficients (b_{abs}) measured by the PAXs at two wavelengths of 405 nm and 532 nm. Superimposed on the same graph are rBC mass concentrations, measured by the SP2. The absorption coefficients (b_{abs}) and rBC mass concentrations decrease over time due to particles loss to the chamber walls. Gaps in the PAX data correspond to α-pinene injections when samples were not drawn from the chamber to preserve sample volume inside the chamber.
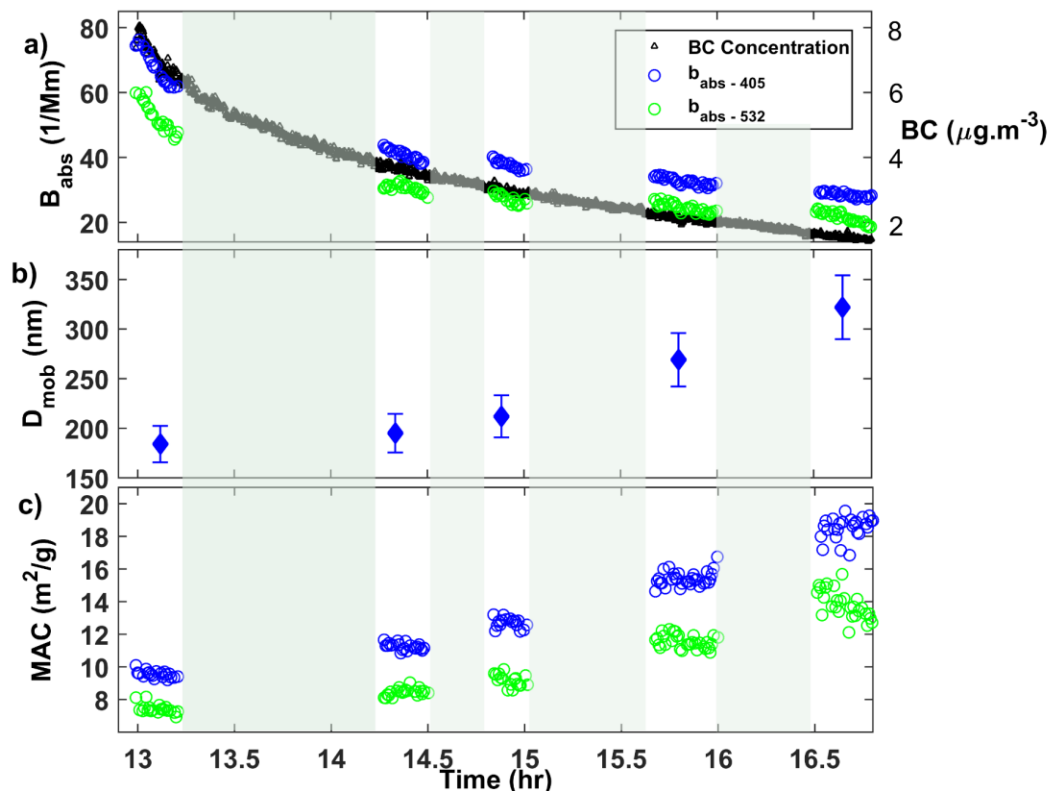
Figure 2.3 Time series for absorption coefficients (a), mobility diameter (b), and MAC (c). Absorption coefficients (Mm^{-1}) at wavelengths of 405 nm and 532 nm measured with PAXs and BC mass concentration measured with SP2. Gaps in the PAX data indicate periods of α-pinene and ozone injections (shown by vertical light olive bars in all panels) when the PAXs were not sampling from the chamber (b) Mobility diameter as a function of time. Each point corresponds to the average data for each α-pinene injection, and error bars indicate a ±10% uncertainty in mobility diameter. (c) MAC time series calculated at 405 nm and 532 nm. The decrease in measured MAC$_{BC-532}$ after the last injection period could potentially be due to a noisier 532 nm laser at low chamber b$_{abs}$

Figure 2.3b shows the increase in SMPS measured mode mobility diameter (D_{mob}) indicating that the α-pinene SOA coats the BC aggregates. Increase in mobility diameter as a result of coagulation is expected to be negligible under our experimental conditions. In this experiment, the mode of the mobility diameter increased from 180 ± 18 nm (fresh emissions) to 322 ± 32 nm after four α-pinene injections.

2.4.1 Fresh OA:BC

For experiments 1, 2, and 3 the OA:BC ratio of fresh emissions was 0.34, 0.44, and 0.56 respectively, calculated as the average of the two limiting cases (see section 2.2.4). These values are broadly consistent with values reported in the literature given the known variability in emissions with cookstove operation (Roden et al. 2009), fuel (Li et al. 2009; L'Orange et al. 2012), and stove design (Preble et al. 2014; Jetter et al. 2012). For example, MacCarty et al. (2008) report that elemental carbon (EC) contributes 68% of total particulate matter (PM) emissions of a rocket stove operating in flaming conditions which translates to a non-EC to EC mass ratio of 0.47. Similarly, Just et al. (2013) report that EC constitutes around 53% of total PM emitted from a rocket stove, corresponding to a non-EC to EC mass ratio of 0.88.

2.4.2 Measured Optical Properties

Fresh emissions exhibited single scattering albedo (SSA) – ratio of scattering to extinction – of 0.16, 0.26, and 0.20 at 532 nm for experiments 1, 2, and 3 respectively. These values agree with the range reported in Bond & Bergstrom (2006) of 0.2-0.3 for fresh BC and are lower than the SSA of 0.36 for the Berkley-Darfur Stove measured by Preble et al. (2014), as expected since our experiments are focused on BC-rich emissions. Also, we measured a fresh MAC_{BC-532} of 8.5 m^2.g^{-1}, 7.2 m^2.g^{-1}, and 7.4 m^2.g^{-1} for experiments 1, 2, and 3 respectively, which are similar to central values reported by Bond & Bergstrom (2006) of 7.5 ± 1.2 m^2.g^{-1} at 550 nm for fresh combustion soot (assuming an inverse wavelength dependence). These results indicate that fresh emissions consisted mainly of BC.

The measured MAC_{BC} time series are shown in Figure 2.3c. The first segment of data corresponds to MAC_{BC} of fresh emissions and the other segments correspond to MAC_{BC} after different amounts of SOA formation. Condensation of SOA on the BC seeds increased the average MAC_{BC-532} by a factor of two, from 7.4 ± 0.35 m^2.g^{-1} to 14.4 ± 0.7 m^2.g^{-1}, indicating absorption enhancement by lensing induced by the SOA coating. The increase is most dramatic at low OA:BC ratios. Similar enhancement has been reported by previous laboratory studies, including diesel engine BC particles coated with α-pinene SOA (Schnaiter 2005), and ethylene flame BC particles coated with dioctyl sebacate (DOS) (Cappa et al. 2012).

Figures 2.4 and 2.5 show the MAC_{BC-532} and MSC at 532 nm versus the OA:BC each averaged over time intervals between different injection periods. We focus on results at 532 nm in the main text because the Rayleigh criterion ($x_m \ll 1$) is more robust at 532 nm than at 405 nm. Results for 405 nm are shown in Figures S5 and S6 in the SI. At small OA:BC ratios (OA:BC < 2), the MSC (Figure 2.5) exhibits a sharp increase. However, as the OA:BC (coating thickness) further increases, MSC plateau and then starts to decrease.

2.4.3 Comparison of Measured and Modeled Optical Properties

In this section, we compare Mie and our simplified RDG predictions to the measured absorption and scattering efficiencies. MAC$_{BC}$ modeled with Mie theory depends on the initial BC size distribution and therefore varied from experiment to experiment. However, MAC$_{BC}$ predicted from RDG theory only depends on the monomer diameter, hence a single RDG calculation line represents all three experiments. MSC modeled with the simplified RDG theory depends on the number of monomers, which were different across

experiments; therefore, three different calculation lines represent the three different experiments.

2.4.3.1 Absorption

Comparison between measured and Mie-predicted MAC_{BC-532} as a function of OA:BC is shown in Figure 2.4 (results at 405 nm are shown in Figure S5). For all experiments, Mie theory MAC$_{BC-532}$ are within 2% ($R^2 = 0.91$, see Figure S7) of measured MAC$_{BC-532}$. Mie predictions underestimate measured MAC$_{BC-405}$ by 12% ($R^2=0.93$, see Figure S7). The better agreement of measured fresh MAC$_{BC-532}$ with Mie prediction, for experiment 1 (magenta data points), may reflect differences in particle shape.
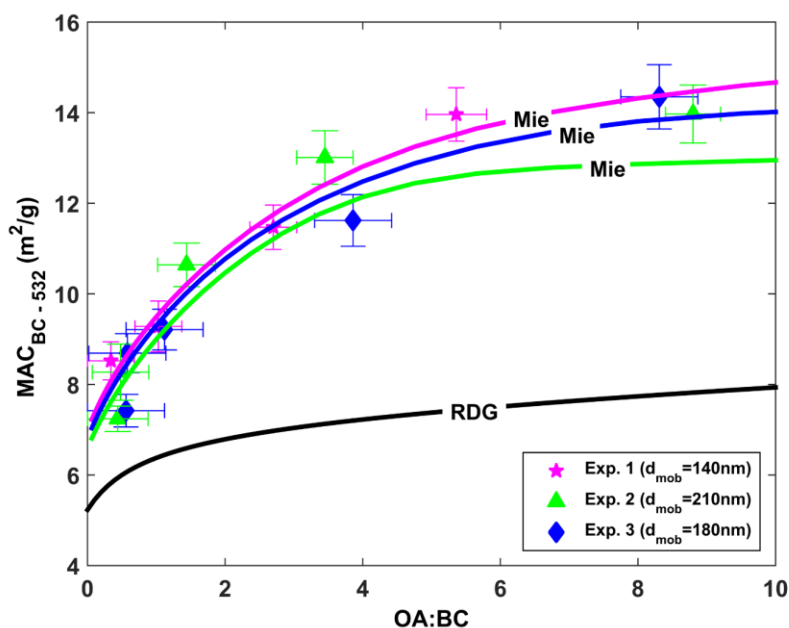
Figure 2.4 Measured and modeled mass absorption cross section, at 532 nm, as a function of the OA:BC ratio. Data points represent measured MAC$_{BC-532}$. Horizontal error bars correspond to the OA:BC range from cases 1 and 2, and vertical error bars correspond to measurement uncertainty in MAC$_{BC}$ calculations. Measurements uncertainty on the OA:BC ratio is around 30% of the plotted values and are not shown on this plot. Magenta, green, and blue data points correspond to experiment 1, 2, and 3 respectively. Similarly, colored solid lines correspond to Mie calculations for the respective experiments. Solid black line corresponds to RDG MAC$_{BC}$ calculations, which are only dependent on the monomer diameter and common for all experiments. Across the entire OA:BC range measured absorption is consistent with Mie theory predictions.

Figure 2.4 also shows the RDG predictions of MAC_{BC-532} (comparison at 405 nm is shown in Figure S5). The divergence between Mie and RDG MAC_{BC} predictions in Figure 2.4 for nascent BC particles (OA:BC→0) agrees with Bond & Bergstrom (2006). Measured values for fresh MAC_{BC-532} fall between RDG and Mie prediction lines for experiments 2 and 3 (blue and green data points) and are higher than RDG predictions by up to 20%. This agrees with Farias et al. (1996) who report (for N between 30 and 100, $|n_{BC} - 1| = 1.23$, and $x_m = 0.2$) that the error in using RDG for absorption treatment is between 10% to 30% of more exact model calculations. As the OA:BC ratio increases, RDG under-predicts the measured absorption, indicating that the absorption behavior of BC particles follows that of a core-shell morphology.

2.4.3.2 Scattering

Figure 2.5 shows a comparison of measured and modeled MSC using Mie and the simplified RDG simulations at 532 nm (results at 405 nm are shown in Figure S6 of the SI). When OA:BC > 2, Mie theory reproduces the measured MSC from experiments 1 and 3 (magenta and blue data points in Figure 2.5). Similar behavior is observed for experiment 2 (green data points), however, Mie theory only reproduced the data at a higher OA:BC (OA:BC > 4). This could be due to BC particles from experiment 2 having a more fractal-like shape (lower fractal dimension) than BC aggregates from the other experiments, as fresh BC aggregates from experiment 2 had the largest difference between their fresh mobility diameter (210 nm) and their fresh mass equivalent diameter (130 nm). Similarly, at 405 nm (Figure S6), measured MSC converges towards Mie prediction lines for OA:BC > 5.
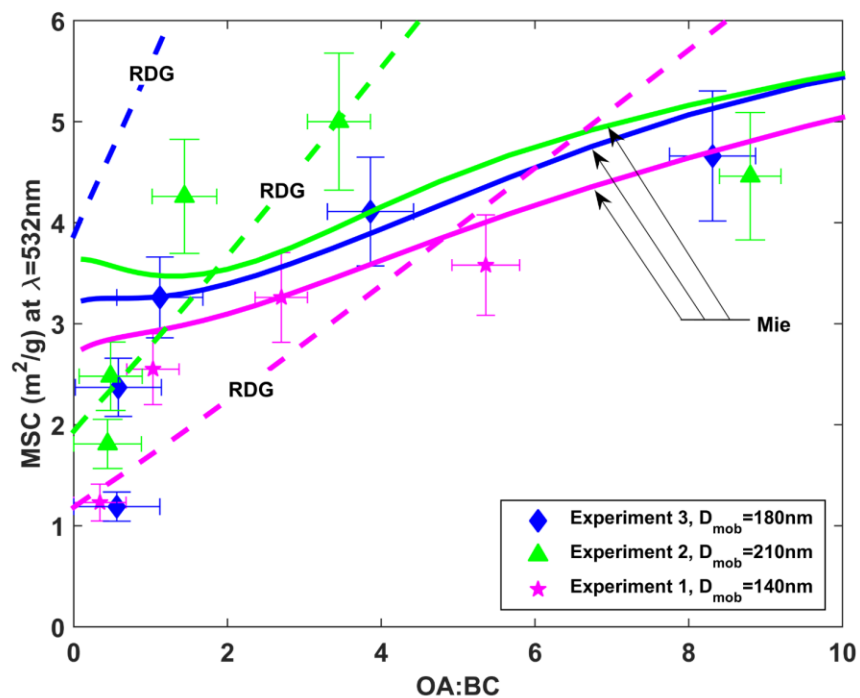
Figure 2.5 Measured and modeled mass scattering cross section, at 532 nm, as a function of the chamber OA:BC. Symbols represent average measured MSC after each α–pinene injection. Horizontal error bars correspond to the OA:BC range from cases 1 and 2, and vertical error bars correspond to measurement uncertainty in MSC. Measurement uncertainty on the OA:BC is around 30% of the plotted values and are not shown on this plot. Colored solid lines correspond to Mie calculations and dashed colored lines correspond to RDG calculations. MSC of fresh stove emissions fall below Mie predictions, presumably due to the fractal shape of the aggregates. As non-BC coating thickness increases, MSC converges towards Mie predictions, suggesting that the BC-containing particles assume a spherical geometry.

We also compare the simplified RDG predictions to the measured MSC, at 532 nm, for small OA:BC ratios where Mie theory fails to capture the sharp increase in MSC, presumably due to the fractal shape of the BC containing particles at small coating thicknesses (Figure 2.5). The simple RDG formulation is able to capture measured MSC for experiments 1 and 2 (magenta and green data points in Figure 2.5), consistent with a fractal shape of fresh and lightly coated BC aggregates. The better RDG agreement exhibited with measured MSC rather than with measured MAC_{BC} is potentially due to a higher sensitivity of scattering on shape, which RDG is able to capture. RDG predictions

35

grossly over-predict measured MSC for experiment 3 (blue data points in Figure 2.5). This may be due to BC aggregates having the largest number of monomers (N=100), which makes our simplified RDG treatment less applicable (see section 2.3.2). As expected, at 405 nm (Figure S6), larger discrepancies are observed between measured and RDG predicted MSC. This is because the Rayleigh criteria is better satisfied at smaller monomer diameter to wavelength ratios ($x_m \ll 1$).

2.4.4 Radiative Forcing Implications

To illustrate the potential radiative forcing implications of our findings, we calculate the spectral simple forcing efficiency (dSFE) (Chylek & Wong 1995) using MAC and MSC values 1) derived from measurements, 2) calculated using Mie theory, and 3) calculated using RDG theory. dSFE is a simple representation based on a two layer radiative model and valid in the optically thin limit, but provides insight on the performance of the optical models (Chen & Bond 2010; Saleh et al. 2014; Hassan et al. 2015). Spectral SFE (dSFE) is given by (Chylek & Wong 1995):

$$\frac{dSFE}{d\lambda} = -\frac{1}{4}\frac{S(\lambda)}{d\lambda}\tau_{atm}^2(\lambda)(1-F_c)[2(1-a_s)^2\beta(\lambda).\text{MSC}(\lambda) - 4a_s.\text{MAC}(\lambda)] \quad (2.6)$$

Where $\frac{S(\lambda)}{d\lambda}$ is the spectral solar irradiance (taken to be 1.85 W.m^{-2}.nm^{-1} and 1.75 W.m^{-2}.nm^{-1} at 532 nm and 405 nm respectively). The other parameters in Equation 2.6 are the atmospheric transmissivity (τ_{atm}: 0.79), the cloud fraction (F_c: 0.6), the average surface albedo (a_s: 0.19) (Chen & Bond 2010). The backscatter was assumed to be wavelength and size independent ($\beta(\lambda)$: 0.15).
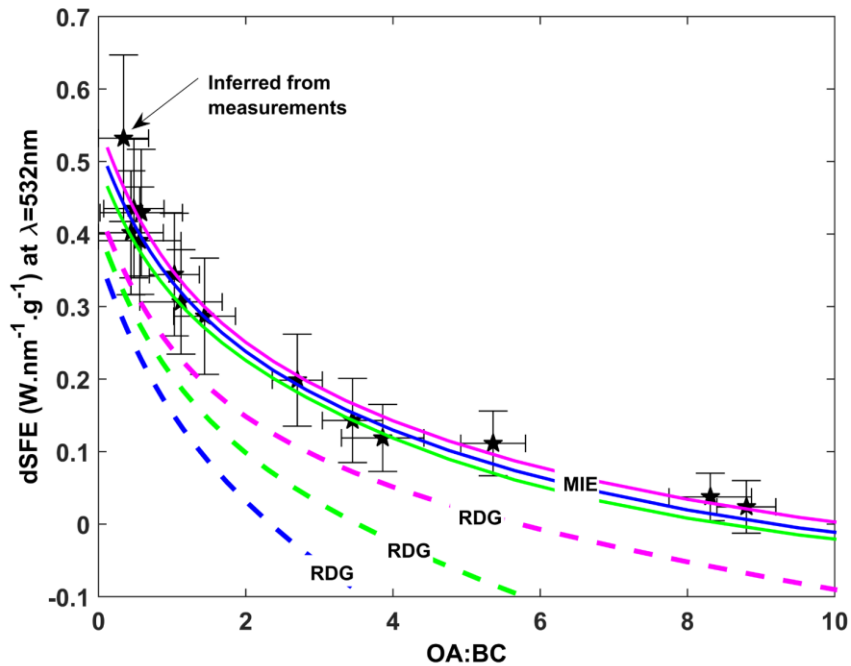
Figure 2.6 Spectral Simple Forcing Efficiency (dSFE), at 532 nm, as a function of the chamber OA:BC. Symbols indicate estimates derived from measured data (dSFE_measure) for all experiments. Magenta, green, and blue solid/dashed colored lines correspond to predictions from Mie theory (dSFE_Mie)/RDG theory (dSFE_RDG) for experiments 1, 2, and 3 respectively. Magenta, green, and blue RDG model lines represent experiments with increasing number of monomers per aggregates (N=30, 60, and 100 for experiments 1, 2, and 3 respectively). Mie theory simple forcing estimates are in good agreement across the entire OA:BC ratio. RDG forcing estimates increasingly overestimate the cooling effect of coated BC particles, and this is because our simple RDG formulations breaks down at high OA:BC ratios.

   Figure 2.6 shows the comparison between dSFE calculated MAC and MSC inferred from measurements (dSFE_measure) and dSFEs calculated using modeled MAC and MSC from Mie (dSFE_Mie) and RDG (dSFE_RDG) theories at 532 nm for all experiments (results at 405 nm are shown in Figure S8). Fresh cookstove emissions exhibited strong positive forcing. However, as we coated (aged) the emissions with α-pinene SOA, forcing of aged rocket stove emissions decreases, approaching a zero net radiative effect at OA:BC ratios close to 10.

Across the entire OA:BC range, dSFE$_{measure}$ and dSFE$_{Mie}$ agree. This is not surprising for OA:BC > 2, since Mie theory reproduced measured MAC and MSC of aged BC aggregates. However, the good agreement at lower OA:BC is somewhat unexpected since Mie theory failed to reproduced the sharp increase in measured MSC, however, scattering has a smaller multiplier than absorption in dSFE calculations, given the choice of constants in Equation 2.6.

In contrast to Mie theory, the simplified RDG under-predicts the spectral forcing efficiency of BC particles emitted from cookstove operation, across the entire OA:BC range. This is not surprising at high OA:BC where the Rayleigh assumption breaks down. However, at low OA:BC where RDG is in relatively good agreement with measured MSC we expected better agreement. The poor agreement between dSFE$_{RDG}$ and dSFE$_{measure}$ is due to the poor agreement between RDG-predicted MAC and measurements, since dSFE has a stronger dependence on absorption than on scattering.

One potential weakness of these RDG simulations is that the monomer sizes were obtained from a separate set of experiments (see section 3 in the SI), and the evaluation would have been more rigorous with TEM images captured during these particular set of experiments. However, the ability of a simple model – Mie theory – to better reproduce observed experimental results perhaps obviates the need for a rigorous examination of RDG when considering aged cookstove BC.

2.5 Conclusion

We characterized the optical properties of BC-rich particle emissions from a rocket stove operating under flaming conditions, both in the fresh state and coated with α–pinene SOA (representative of non-absorbing OA) to reflect atmospherically aged BC. We explored a wide range of OA:BC ratios encompassing most of the variability of atmospheric values, which can vary substantially depending on the source and location (Schwarz et al. 2008; Cappa et al. 2012). BC emitted from the cookstove exhibited lensing when coated with α-pinene SOA, which enhanced the absorption potency of BC particles by up a factor of about two and the scattering up to a factor of about four.

The simplified RDG treatment exhibited relatively good agreement with the MSC inferred from measurements, at 532 nm, for BC aggregates with N < 60 (the simplified RDG scattering predictions degraded for BC aggregates with N = 100) and at low coating thicknesses, unlike Mie theory which did not capture the initial sharp increase in MSC. This is likely due to the fractal shape of fresh and lightly coated BC aggregates. However, RDG greatly underestimated measured MAC$_{BC}$ across the entire OA:BC range. Mie theory exhibited good agreement with the measured MAC_{BC} across the entire measurement range, and MSC for OA:BC > 4 (for all experiments). Although good agreement between measured and Mie-modeled MSC is exhibited at OA:BC > 4, it must be emphasized that larger OA:BC values are more representative of aged carbonaceous aerosols in the atmosphere. Cappa et al. (2012) measured non-BC to BC ratios greater than 3 (for fresh emissions) and up to 15 (for aged BC containing particles) in California. Similarly, Saleh et al. (2015) calculated that BC-containing particles emitted from biomass burning had non-BC:BC ratios greater than 3. This indicates that away from sources, BC particles emitted from cookstove emissions will be heavily coated, supporting the simple core-shell

morphology as being a good representation of aged cookstove emissions in regional air masses.

Mie-Modeled dSFE exhibited good agreement with dSFE calculated from measured quantities across the entire OA:BC range. Although this simple forcing estimate lacks spatial and temporal resolutions, it still sheds light on the poor performance of our simplified RDG formulation. The simplified RDG model degrades as the coating thickness around the aggregates increases (increasing OA:BC) and as the number of monomer per-aggregate (N) increases. Previous studies reported good agreement between RDG and measured absorption for fresh diesel soot (Adler et al. 2009) and BC from inverted burner (Chakrabarty et al. 2007). However, our results indicate that our simplified RDG treatment is not a viable alternative to Mie theory to estimate forcing of aged and coated cookstove soot particles (which are generally larger than diesel soot particles) in climate models.

2.6 References

Adachi, K., Chung, S.H. & Buseck, P.R., 2010. Shapes of soot aerosol particles and implications for their effects on climate. *Journal of Geophysical Research: Atmospheres*, 115, pp.1–9.

Adkins, E. et al., 2010. Field testing and survey evaluation of household biomass cookstoves in rural sub-Saharan Africa. *Energy for Sustainable Development*, 14(3), pp.172–185.

Adler, G. et al., 2009. Effect of intrinsic organic carbon on the optical properties of fresh diesel soot. *Proceedings of the National Academy of Sciences*, 107(15), pp.6699–6704. Available at: http://www.pnas.org/cgi/doi/10.1073/pnas.0903311106 [Accessed June 30, 2015].

Andreae, M.O. & Gelencsér, A., 2006. Black carbon or brown carbon? The nature of light-absorbing carbonaceous aerosols. *Atmospheric Chemistry and Physics Discussions*, 6(3), pp.3419–3463.

Arnott, W.P. et al., 1999. Photoacoustic spectrometer for measuring light absorption by aerosol: Instrument description. *Atmospheric Environment*, 33, pp.2845–2852.

Arnott, W.P., Moosmüller, H. & Walker, J.W., 2000. Nitrogen dioxide and kerosene-flame soot calibration of photoacoustic instruments for measurement of light absorption by aerosols. *Review of Scientific Instruments*, 71(12), p.4545. Available at: http://link.aip.org/link/RSINAK/v71/i12/p4545/s1&Agg=doi.

Bohren, C.F. & Huffman, D.R., 1983. *Absorption and scattering of light by small particles*, Available at: http://adsabs.harvard.edu/abs/1983uaz..rept.....B.

Bond, T.C. et al., 2013. Bounding the role of black carbon in the climate system: A scientific assessment. *Journal of Geophysical Research: Atmospheres*, 118(11), pp.5380–5552. Available at: http://doi.wiley.com/10.1002/jgrd.50171 [Accessed July 11, 2014].

Bond, T.C. & Bergstrom, R.W., 2006. Light Absorption by Carbonaceous Particles: An Investigative Review. *Aerosol Science and Technology*, 40(1), pp.27–67. Available at: http://www.tandfonline.com/doi/abs/10.1080/02786820500421521 [Accessed July 15, 2014].

Bond, T.C., Habib, G. & Bergstrom, R.W., 2006. Limitations in the enhancement of visible light absorption due to mixing state. *Journal of Geophysical Research*, 111(D20), p.D20211. Available at: http://doi.wiley.com/10.1029/2006JD007315 [Accessed August 12, 2014].

Cappa, C.D. et al., 2012. Radiative absorption enhancements due to the mixing state of atmospheric black carbon. *Science (New York, N.Y.)*, 337(6098), pp.1078–81. Available at: http://www.ncbi.nlm.nih.gov/pubmed/22936774 [Accessed July 15, 2014].

Chakrabarty, R.K. et al., 2016. Brown carbon aerosols from burning of boreal peatlands: microphysical properties, emission factors, and implications for direct radiative forcing. *Atmospheric Chemistry and Physics*, 16(5), pp.3033–3040. Available at: http://www.atmos-chem-phys.net/16/3033/2016/.

Chakrabarty, R.K. et al., 2007. Light scattering and absorption by fractal-like carbonaceous chain aggregates: comparison of theories and experiment. *Applied optics*, 46, pp.6990–7006.

Chen, Y. & Bond, T.C., 2010. Light absorption by organic carbon from wood combustion. *Atmospheric Chemistry and Physics*, 9, pp.1773 – 1787. Available at: http://www.atmos-chem-phys-discuss.net/9/20471/2009/.

Chen, Y., Roden, C.A. & Bond, T.C., 2012. Characterizing biofuel combustion with Patterns of Real-Time Emission Data (PaRTED). *Environmental Science and Technology*, 46(11), pp.6110–6117.

China, S. et al., 2013. Morphology and mixing state of individual freshly emitted wildfire carbonaceous particles. *Nature communications*, 4, p.2122. Available at: http://www.pubmedcentral.nih.gov/articlerender.fcgi?artid=3715871&tool=pmcentr ez&rendertype=abstract [Accessed April 28, 2015].

Chylek, P. & Wong, J., 1995. Effect of absorbing aerosols on global radiation budget. *Geophysical Research Letters*, 22, pp.929–931. Available at: http://doi.wiley.com/10.1029/95GL00800.

Cross, E.S. et al., 2010. Soot Particle Studies—Instrument Inter-Comparison—Project Overview. *Aerosol Science and Technology*, 44, pp.592–611.

DeCarlo, P. & Slowik, J., 2004. Particle morphology and density characterization by combined mobility and aerodynamic diameter measurements. Part 1: Theory. *Aerosol Science and …*, 38(12), pp.1185–1205. Available at: http://www.tandfonline.com/doi/abs/10.1080/027868290903907\nhttp://www.tandfo nline.com/doi/pdf/10.1080/027868290903907 [Accessed July 23, 2014].

Farias, T.L., Köylü, Ü.Ö. & Carvalho, M.G., 1996. Range of validity of the Rayleigh—Debye—Gans theory for optics of fractal aggregates. *Applied Optics*, 35, p.6560.

Feng, Y., Ramanathan, V. & Kotamarthi, V.R., 2013. Brown carbon: a significant atmospheric absorber of solar radiation? *Atmospheric Chemistry and Physics*, 13(17), pp.8607–8621. Available at: http://www.atmos-chem-phys.net/13/8607/2013/ [Accessed August 17, 2015].

Fuller, K.A., 1995. Scattering and absorption cross sections of compounded spheres. III. Spheres containing arbitrarily located spherical inhomogeneities. *Journal of the Optical Society of America A*, 12(5), p.893.

Fuller, K.A., Malm, W.C. & Kreidenweis, S.M., 1999. Effects of mixing on extinction by

carbonaceous particles. *Journal of Geophysical Research: Atmospheres*, 104(D13), pp.15941–15954. Available at: http://dx.doi.org/10.1029/1998JD100069.

Gysel, M. et al., 2011. Effective density of Aquadag and fullerene soot black carbon reference materials used for SP2 calibration. *Atmospheric Measurement Techniques*, 4(12), pp.2851–2858. Available at: http://www.atmos-meas-tech.net/4/2851/2011/ [Accessed April 12, 2015].

Hassan, T., Moosmüller, H. & Chung, C.E., 2015. Coefficients of an analytical aerosol forcing equation determined with a Monte-Carlo radiation model. *Journal of Quantitative Spectroscopy and Radiative Transfer*, 164, pp.129–136.

Holder, A.L. et al., 2014. On-road black carbon instrument intercomparison and aerosol characteristics by driving environment. *Atmospheric Environment*, 88, pp.183–191. Available at: http://dx.doi.org/10.1016/j.atmosenv.2014.01.021.

Jacobson, M.Z., 2000. A physically-based treatment of elemental carbon optics: Implications for global direct forcing of aerosols. *Geophys. Res. Lett.,*, 27, pp.217–220. Available at: http://dx.doi.org/10.1029/1999GL010968.

Jacobson, M.Z., 2010. Short-term effects of controlling fossil-fuel soot, biofuel soot and gases, and methane on climate, Arctic ice, and air pollution health. *Journal of Geophysical Research*, 115(D14), p.D14209. Available at: http://doi.wiley.com/10.1029/2009JD013795 [Accessed August 30, 2015].

Jacobson, M.Z., 2001. Strong radiative heating due to the mixing state of black carbon in atmospheric aerosols. *Nature*, 409, pp.695–697.

Jetter, J. et al., 2012. Pollutant Emissions and Energy E ffi ciency under Controlled Conditions for Household Biomass Cookstoves and Implications for Metrics Useful in Setting International Test Standards. *Environmental Science and Technology*.

Just, B., Rogak, S. & Kandlikar, M., 2013. Characterization of ultrafine particulate matter from traditional and improved biomass cookstoves. *Environmental Science and Technology*, 47(7), pp.3506–3512.

Kodros, J.K. et al., 2015. Uncertainties in global aerosols and climate effects due to biofuel emissions. *Atmospheric Chemistry and Physics*, 15(15), pp.8577–8596.

L'Orange, C., DeFoort, M. & Willson, B., 2012. Influence of testing parameters on

biomass stove performance and development of an improved testing protocol. *Energy for Sustainable Development*, 16(1), pp.3–12.

Lack, D. a. et al., 2009. Absorption Enhancement of Coated Absorbing Aerosols: Validation of the Photo-Acoustic Technique for Measuring the Enhancement. *Aerosol Science and Technology*, 43(10), pp.1006–1012. Available at: http://www.tandfonline.com/doi/abs/10.1080/02786820903117932 [Accessed August 30, 2015].

Lack, D. a. et al., 2006. Aerosol Absorption Measurement using Photoacoustic Spectroscopy: Sensitivity, Calibration, and Uncertainty Developments. *Aerosol Science and Technology*, 40(9), pp.697–708. Available at: http://www.tandfonline.com/doi/abs/10.1080/02786820600803917 [Accessed September 5, 2014].

Lack, D.A. & Cappa, C.D., 2010. Impact of brown and clear carbon on light absorption enhancement, single scatter albedo and absorption wavelength dependence of black carbon. *Atmospheric Chemistry and Physics*, 10(9), pp.4207–4220.

Li, X. et al., 2009. Carbonaceous aerosol emissions from household biofuel combustion in China. *Environmental Science and Technology*, 43(15), pp.6076–6081.

Liu, S. et al., 2015. Enhanced light absorption by mixed source black and brown carbon particles in UK winter. *Nature communications*, 6, p.8435. Available at: http://www.pubmedcentral.nih.gov/articlerender.fcgi?artid=4598716&tool=pmcentr ez&rendertype=abstract [Accessed November 9, 2015].

MacCarty, N. et al., 2008. A laboratory comparison of the global warming impact of five major types of biomass cooking stoves. *Energy for Sustainable Development*, 12(2), pp.56–65.

Moffet, R.C. & Prather, K. a, 2009. In-situ measurements of the mixing state and optical properties of soot with implications for radiative forcing estimates. *Proceedings of the National Academy of Sciences of the United States of America*, 106, pp.11872–11877.

Moosmüller, H. & Arnott, W.P., 2009. Particle Optics in the Rayleigh Regime. *Journal of the Air & Waste Management Association*, 59(9), pp.1028–1031. Available at: http://www.tandfonline.com/doi/abs/10.3155/1047-3289.59.9.1028 [Accessed

October 20, 2015].

Moteki, N. et al., 2007. Evolution of mixing state of black carbon particles: Aircraft measurements over the western Pacific in March 2004. *Geophysical Research Letters*, 34.

Moteki, N. & Kondo, Y., 2010. Dependence of Laser-Induced Incandescence on Physical Properties of Black Carbon Aerosols: Measurements and Theoretical Interpretation. *Aerosol Science and Technology*, 44(8), pp.663–675.

Olfert, J.S. & Collings, N., 2005. New method for particle mass classification—the Couette centrifugal particle mass analyzer. *Journal of Aerosol Science*, 36, pp.1338–1352.

Preble, C. V. et al., 2014. Emissions and climate-relevant optical properties of pollutants emitted from a three-stone fire and the berkeley-darfur stove tested under laboratory conditions. *Environmental Science and Technology*, 48(11), pp.6484–6491.

Presto, A.A. & Donahue, N.M., 2006. Investigation of alpha-pinene + ozone secondary organic aerosol formation at low total aerosol mass. *Environmental science & technology*, 40, pp.3536–3543.

Presto, A.A., Huff Hartz, K.E. & Donahue, N.M., 2005. Secondary organic aerosol production from terpene ozonolysis. 2. Effect of NOx concentration. *Environmental Science and Technology*, 39, pp.7046–7054.

Ramanathan, V. & Carmichael, G., 2008. Global and regional climate changes due to black carbon. *Nature Geoscience*, 1(4), pp.221–227.

Reid, J.S. & Hobbs, P. V., 1998. Physical and optical properties of young smoke from individual biomass fires in Brazil. *Journal of Geophysical Research*, 103, p.32013.

Riemer, N., Vogel, H. & Vogel, B., 2004. Soot aging time scales in polluted regions during day and night. *Atmospheric Chemistry and Physics*, 4, pp.1885–1893.

Roden, C.A. et al., 2009. Laboratory and field investigations of particulate and carbon monoxide emissions from traditional and improved cookstoves. *Atmospheric Environment*, 43(6), pp.1170–1181.

Roehl, C.M. et al., 1994. Temperature dependence of the quantum yields for the photolysis of NO2 near the dissociation limit. *The Journal of Physical Chemistry*,

98(32), pp.7837–7843. Available at:
http://pubs.acs.org/doi/abs/10.1021/j100083a015\nhttp://pubs.acs.org/doi/pdf/10.102
1/j100083a015.

Saleh, R. et al., 2014. Brownness of Organics in Aerosols from Biomass Burning Linked
to their Black Carbon Content. *Nature Geoscience*, 7, pp.1–4. Available at:
http://www.nature.com/doifinder/10.1038/ngeo2220.

Saleh, R., M. Marks, J. Heo, P.J.Adams, N.M. Donahue, A.L.R., 2015. Contribution of
Brown Carbon and Lensing to the Direct Radiative Effect of Carbonaceous Aerosols
from Biomass and Biofuel Burning Emissions. *J. Geophys. Res. Atmos.*, pp.1–12.

Scarnato, B. V. et al., 2013. Effects of Internal Mixing and Aggregate Morphology on
Optical Properties of Black Carbon Using a Discrete Dipole Approximation Model.
Atmospheric Chemistry and Physics, 13(10), pp.5089–5101.

Schnaiter, M., 2005. Absorption Amplification of Black Carbon Internally Mixed with
Secondary Organic Aerosol. *Journal of Geophysical Research*, 110(D19),
p.D19204. Available at: http://doi.wiley.com/10.1029/2005JD006046 [Accessed
August 11, 2014].

Schnitzler, E.G. et al., 2014. Soot Aggregate Restructuring due to Coatings of Secondary
Organic Aerosol Derived from Aromatic Precursors. *Environmental Science and
Technology*, 48(24), pp.14309–14316.

Schwarz, J.P. et al., 2008. Measurement of the Mixing State, Mass, and Optical Size of
Individual Black Carbon Particles in Urban and Biomass Burning Emissions.
Geophysical Research Letters, 35(13), pp.1–5.

Schwarz, J.P. et al., 2006. Single-Particle Measurements of Midlatitude Black Carbon
and Light-Scattering Aerosols from the Boundary Layer to the Lower Stratosphere.
Journal of Geophysical Research, 111(D16), p.D16207. Available at:
http://doi.wiley.com/10.1029/2006JD007076 (Accessed April 12, 2015).

Sedlacek, A.J. et al., 2012. Determination of and Evidence for Non-Core-Shell Structure
of Particles Containing Black Carbon Using the Single-Particle Soot Photometer
(SP2). *Geophysical Research Letters*, 39.

Sharma, N. et al., 2013. Photoacoustic and Nephelometric Spectroscopy of Aerosol

Optical Properties with a Supercontinuum Light Source. *Atmospheric Measurement Techniques*, 6(12), pp.3501–3513.

Shiraiwa, M. et al., 2010. Amplification of Light Absorption of Black Carbon by Organic Coating. *Aerosol Science and Technology*, 44(1), pp.46–54. Available at: http://www.tandfonline.com/doi/abs/10.1080/02786820903357686 (Accessed July 30, 2015).

Sorensen, C.M., 2001. Light Scattering by Fractal Aggregates: A Review. *Aerosol Science and Technology*, 35, pp.648–687.

Subramanian, R. et al., 2010. Black Carbon Over Mexico: The Effect of Atmospheric Transport on Mixing State, Mass Absorption Cross-Section, and BC/CO Ratios. *Atmospheric Chemistry and Physics.* **2010**, *10*(1).

Wang, Q. et al., 2014. Mixing State of Black Carbon Aerosol in a Heavily Polluted Urban Area of China: Implications for Light Absorption Enhancement. *Aerosol Science and Technology*, 48(7), pp.689–697. Available at: http://www.tandfonline.com/doi/abs/10.1080/02786826.2014.917758 [Accessed August 10, 2014].

Wang, X. et al., 2014. Exploiting Simultaneous Observational Constraints on Mass and Absorption to Estimate the Global Direct Radiative Forcing of Black Carbon and Brown Carbon. *Atmospheric Chemistry and Physics*, 14, pp.10989–11010. Available at: http://www.scopus.com/inward/record.url?eid=2-s2.0-84908464735&partnerID=tZOtx3y1

Wilson, D.L. et al., 2016. Avoided Emissions of a Fuel-Efficient Biomass Cookstove Dwarf Embodied Emissions. *Development Engineering*, 1, pp.45–52. Available at: http://dx.doi.org/10.1016/j.deveng.2016.01.001

Zhang, R. et al., 2008. Variability in Morphology, Hygroscopicity, and Optical Properties of Soot Aerosols During Atmospheric Processing. *Proceedings of the National Academy of Sciences of the United States of America*, 105, pp.10291–6. Available at: http://www.pnas.org/content/105/30/10291.full.

CHAPTER 3

AEROSOL OPTICAL PROPERTIES AND CLIMATE IMPLICATIONS OF EMISSIONS FROM TRADITIONAL AND IMPROVED COOKSTOVES[2]

Abstract

Cookstove emissions are a major global source of black carbon (BC) but their impact on climate is uncertain because of limited understanding of their optical properties. We measured optical properties from fresh aerosol emissions from 32 different stove/fuel combinations, ranging from simple open fires to high-performing forced-draft stoves. Stoves were tested in the laboratory using the firepower sweep protocol, which measures emissions performance across the entire range of functional firepower. There is large variability in measured optical properties across the entire range of firepower. Variations in optical properties were strongly correlated with black carbon-to-particulate matter mass ratio (BC/PM), consistent with Mie theory predictions for coated particles. In contrast, we found that stove type, fuel, and other operational metrics like the modified combustion efficiency and firepower were all poor predictors of optical properties. We developed parametrizations of the mass absorption cross section per unit BC mass (MAC_{BC}) and per unit PM mass (MAC_{PM}), the absorption angstrom exponent (AAE), and the single scattering albedo (SSA) of fresh emissions as a function of BC/PM. Our data indicate that: (1) for relevant operating cookstove conditions, absorption enhancement from emissions is dominated by the BC mixing-state and lensing and not brown carbon. (2) Current model treatments of the optical properties of cookstove emissions likely overestimate the direct

---

[2] To be submitted to Environmental Science and Technology

radiative forcing. We combined our new parametrizations of intensive optical properties with literature data of real-world cooking emissions to estimate the direct radiative effect of emissions for different stove technologies. Our data suggest only 20% CO_2 equivalent emission reductions (i.e., climate benefits) from so-called "improved" stoves compared to traditional ones.

3.1 Introduction

Aerosol emissions contribute to climate change by absorbing and scattering outgoing and incoming radiation (Jacobson 2001). Cookstoves are important global sources of light-absorbing aerosol such as black carbon (BC) (Bond et al. 2013) and brown carbon (BrC) (Andreae & Gelencsér 2006; Kirchstetter et al. 2004; Chen & Bond 2010; Saleh et al. 2014). Indoor pollution from cookstove emissions contribute to more than four million annual deaths worldwide (Lim et al. 2012). To reduce climate, health, and environmental impacts, so-called "improved" stoves are being promoted as cleaner alternatives to traditional technologies. Improved stove designs range from adding a combustion chamber (natural-draft rocket-style stove) to including an electric fan (forced-draft stove). These changes can improve combustion efficiency and heat transfer to the cook-piece and therefore reduce emissions. Field studies indicate that improved stoves have modestly lower particulate matter (PM) mass emissions compared to traditional stoves (Roden et al. 2009; Grieshop et al. 2017; Wathore et al. 2017; Coffey et al. 2017); however, improved stoves can also emit higher BC fractions due to their altered combustion conditions (MacCarty et al. 2008; Grieshop et al. 2017; Just et al. 2013; Garland et al. 2017). Therefore, the large-scale deployment of improved stoves could have important climate implications.

Predicting the future climate impacts of newer stove technologies requires accurate emission inventories and correct representation of the optical properties of their emissions (Bond et al. 2013). The limited published data reveal significant variability in the optical properties of stove emissions (Roden et al. 2006; Grieshop et al. 2017; Preble et al. 2014). For example, emissions from traditional stoves tested in Honduras had a factor of two greater absorption (per BC mass) compared to stoves tested in Malawi (Roden et al. 2006; Grieshop et al. 2017). The causes of these differences are not well understood; they are likely due to the complex interplay between optical properties and stove type/fuel/fire conditions. Misrepresenting optical properties of stoves emissions can lead to a dramatically different predictions of climate impacts. For example, assuming a complete internal mixture between BC and non-BC material and treating the organics as "brown" can change the direct radiative forcing of biomass burning and stove emissions from negative (net cooling) to positive (net heating) compared to a baseline scenario of a complete external mixture with non-absorbing organic material (Kodros et al. 2015; Saleh et al. 2015).

Previous studies have tried to develop parametrizations to explain the variability in optical properties of cookstove emissions. One approach is to use the modified combustion efficiency (MCE, ratio of background corrected CO_2 emissions to background corrected $CO+CO_2$ emissions), which is a measure the completeness of combustion for converting carbonaceous fuel into CO_2. This approach has been used to parametrize aerosol absorption and scattering from cookstove (Grieshop et al. 2017) and biomass burning emissions (Pokhrel et al. 2016; McMeeking et al. 2014; Liu et al. 2014) with moderate to poor correlations. Another parameter of potential importance is the ratio of black carbon mass-to-total particulate matter mass (BC/PM). BC/PM may indicate coating thickness around

the BC particles, which can directly affect their radiative properties (Fuller et al. 1999). Several studies report good correlation between the BC/PM and optical properties such as the mass absorption cross section (MAC_{PM}, absorption per unit PM mass), the absorption angstrom exponent (AAE) and the single scattering albedo (SSA, ratio of scattering to extinction) for cookstove (Roden et al. 2006; Grieshop et al. 2017) and biomass/biofuel burning emissions (Habib et al. 2008; McMeeking et al. 2014; Saleh et al. 2014; Pokhrel et al. 2016; Holder et al. 2016). However, these studies only considered a limited number of stove technologies because of sampling in specific field locations. Although comprehensive parametrizations of aerosol optical properties exist for biomass burning emissions (Pokhrel et al. 2016), we are not aware of similar parametrizations for cookstove emissions.

In this study, we report measurements of aerosol intensive optical properties (MAC_{BC}, SSA, and AAE) of emissions from 18 different cookstoves operating on two different fuels (wood and charcoal). All the stoves were tested in the laboratory using the firepower sweep protocol, which systematically spans the range of functional stove firepowers (Bilsback et al, *in preparation*). Using our dataset of 32 stove/fuel combinations, we investigate the role of stove technology, fuel, and operational metrics (firepower, MCE, and BC/PM) on measured optical properties. We develop parametrizations for these properties as a function of BC/PM. We then combine our new parametrizations with field emission data to estimate the direct radiative forcing from emissions of different stove technologies.

3.2 Methods

3.2.1 Stoves, Fuels, and the Firepower Sweep Protocol

We measured emissions from 18 different stoves operated in the laboratory using the firepower sweep protocol. Compared to previous studies (Roden et al. 2006; Grieshop et al. 2017; Preble et al. 2014; Wathore et al. 2017) reporting optical properties from stove emissions, we tested a much wider range of stove technologies including: three-stone fire, Justa, sunken pot, clay/metal traditional stoves, metal/ceramic charcoal stoves, rocket-style stoves, natural- and forced-draft gasifiers. In total, 32 individual tests were performed; they are detailed in Table S1 in the supporting information (SI). The stoves tested nearly span the ISO total emission's tiers of performance (ISO 2012), from the highest emitting Tier 0 stoves to cleaner Tier 3 stoves. We did not test any Tier 4 stoves, the lowest emitting category. For discussion, the stoves are separated into two major categories: wood and charcoal stoves. These two categories contained multiple sub-categories based on emission certifications. Wood stoves were separated into three categories: traditional (Tier 0), rocket-style (Tier 2), and gasifier (Tier 3) stoves. Similarly, charcoal stoves were segregated into three categories: metal (Tier 0), ceramic (Tier 0), and improved (Tier 2) stoves.

The stoves were tested using different fuels to investigate the effects of fuel type on optical properties. We burnt two different charcoal fuels: coconut and lump-hardwood, and four different wood fuels: red oak, Douglas fir, Eucalyptus, and wood pellets.

To investigate the role of operating conditions, each stove was tested using the firepower sweep protocol. The firepower sweep protocol consists of a startup phase followed by systematic sweeps in firepower and finally a shutdown phase (Bilsback et al. 2017, *in preparation*). Firepower was changed by controlling the rate at which the fuel was

added or removed from the combustion chamber. The firepower sweep protocol has 5 to 7 intermediate fire power steps or holds that span the full range of functional firepower that is feasible for a given stove type in addition to startup and shutdown phases. Each firepower step is intended to represent different cooking practices (e.g., high firepower is often used for boiling water while low firepower is common during simmering). During each five- to ten-minute firepower step there is quasi-steady operations conditions over which we average emissions data. This allows us to systematically investigate emissions over a wide range of operating conditions for the same stove (versus simply integrating the data over the entire test).

3.2.2 Experimental Setup

The experimental setup is show in Figure S1. The entire emissions were captured and diluted inside a constant flow hood. At the hood outlet, a sample of diluted exhaust was drawn into a suite of gas and particle instruments (the latter through an isokinetic inlet). Gas measurements included CO and CO_2 (Siemens ULTRAMAT gas analyzer). Refractory BC (rBC) particle mass concentrations and size distributions were measured using a single-particle soot photometer (SP2 [DMT]). The SP2 uses a 1064 nm laser to incandesce rBC particles which is calibrated to rBC mass (Moteki & Kondo 2010; Schwarz et al. 2006). Particle light-scattering and absorption coefficients were measured using two photo-acoustic extinctiometers (PAX [DMT]) operating at 405 and 532 nm. Prior to sampling with the particle-phase instruments, the emissions were diluted by an additional factor of 99:1 using two Dekati diluters in series (Figure S1). The SP2 was calibrated using size-selected fullerene soot particles (Gysel et al. 2011). The PAXs were calibrated using PSL

spheres for scattering and fullerene soot for absorption, following the manufacturer's recommendation. The data from all instruments were averaged on a one-minute time basis.

Teflon filters were also collected at the hood outlet to determine gravimetric PM mass emissions during each firepower step and for startup and shutdown phases (but not for the entire test). Filters were equilibrated for 24 hours before weighing in a temperature and relative humidity-controlled environment.

3.2.3 Stove Operational Metrics and Aerosol Optical Properties

We examined the influence of three operational metrics on aerosol optical properties: the firepower, the MCE, and the BC/PM. Firepower and MCE are measures of the combustion conditions. MCE is the ratio of background corrected CO_2 concentrations to background corrected $CO+CO_2$ concentrations (MCE=ΔCO_2/($\Delta CO+\Delta CO_2$)). Background signal was very small compared to cookstove emissions. Firepower (FP) is the fuel energy content (e_{fuel}) multiplied by the fuel feed rate. Fuel feed rate is calculated using emission rates of CO (ER_{CO}) and CO_2 (ER_{CO2}) and assuming carbon fraction in the fuel (f_c) of 0.5 g-C/g-fuel for wood and 0.7 g-C/g-fuel for charcoal (Roden et al. 2009).

$$FP = e_{fuel}.1/f_c.\left(ER_{CO}.\left(\frac{M_C}{M_{CO}}\right) + ER_{CO_2}.\left(\frac{M_C}{M_{CO_2}}\right)\right) \tag{3.1}$$

Where M_C, M_{CO}, and M_{CO2}, are the molar masses for carbon, CO, and CO_2 respectively. Emission rates for CO and CO_2 are determined using the measured total hood and instrument flow rates. Energy densities of the fuels (e_{fuel}) were: 16.6 MJ/kg for coconut, 18.6 MJ/kg for Douglas Fir, 19.4 MJ/kg for Eucalyptus, and 28.6 MJ/kg for lump hardwood. The BC/PM is a commonly measured characteristic of the aerosol emissions and may indicate coating around BC particles which can influence aerosol optical

properties. The BC/PM was calculated using filter-based gravimetric PM (collected for each firepower step) and SP2-based rBC (integrated for each firepower step).

One-minute (and for each firepower step) BC-mass absorption cross-sections (MAC_{BC}) were calculated by dividing the absorption coefficients measured by the PAX (b_{abs}) by rBC mass measured using the SP2 ($MAC_{BC}=b_{abs}/rBC$); MAC per total PM mass were calculated for each power step period as: $MAC_{PM}=b_{abs}/PM$. Mass scattering cross-sections (MSC_{PM}) were calculated for each firepower step period by dividing the PAX measured scattering coefficients (b_{sca}) by gravimetric PM mass ($MSC_{PM} =b_{sca}/PM$). The absorption angstrom exponent (AAE, wavelength dependence of absorption) was calculated using the PAX absorption measurements at 405 (b_{abs}^{405}) and 532 nm (b_{abs}^{532}), as shown in Equation 3.2.

$$AAE = -\frac{\log\left(\frac{b_{abs}^{405}}{b_{abs}^{532}}\right)}{\log\left(\frac{405}{532}\right)} \tag{3.2}$$

The single scattering albedo (SSA) is the ratio of scattered to extinguished light (sum of scattering and absorption) that is incident upon a particle. SSA is an estimate of the overall radiative impact from emissions (SSA>0.85 is usually associated with net cooling and SSA<0.85 generally implies net warming).

Another estimate of the direct radiative forcing from emissions, is the simple forcing efficiency (SFE) (Chylek & Wong 1995). The SFE is calculated assuming specific external parameters (such as cloud coverage and surface albedo) and using a simple two-layer atmosphere

$$\frac{dSFE}{d\lambda} = -\frac{1}{4}\frac{S(\lambda)}{d\lambda}\tau_{atm}^2(\lambda)(1 - F_c)$$

$$\times [2(1 - a_s)^2\beta(\lambda).MSC_{PM}(\lambda) - 4.a_s.MAC_{PM}(\lambda)] \tag{3.3}$$

$\frac{S(\lambda)}{d\lambda}$ is the spectral solar irradiance (1.85 W/m^2-nm at 532 nm). The other parameters are the atmospheric transmissivity (τ_{atm}=0.79), the cloud fraction (F_c=0.6), the average surface albedo (a_s=0.19), and the backscatter (β=0.15).(Chen & Bond 2010) The MAC$_{PM}$ term in Equation 3.3 is the absorption coefficient per total mass (MAC$_{PM}$=b_{abs}/PM), and not MAC$_{BC}$.

3.2.4 Particle Mixing-state

We investigated the BC mixing-state using single-particle lag-time information from the SP2. As BC particles travel through the SP2 laser, they scatter and incandesce light (Schwarz et al. 2006; Moteki & Kondo 2010; Subramanian et al. 2010). The temporal difference in detecting both signals is referred to as "lag-time" and provides an estimate of the BC-mixing-state. We use a threshold lag-time value of +2.0 µs to indicate "thickly" coated BC particles. We only used positive lag-time values (i.e., scattering occurs prior to incandescence) which are associated with thickly coated BC particles in a concentric-shell geometry (Sedlacek et al. 2012). Although a large fraction of BC aerosol (>50%) was associated with negative lag-time (BC-particle likely on edge of coating), we assumed there was no absorption amplification (e.g., due to the presence of coating, or lensing effect) from these particles (Cappa et al. 2012).

3.2.5 Fuel-based Emission Factors

Fuel-based emission factors (EF: emitted pollutant 'i' mass per mass of fuel burnt) were calculated using a carbon mass balance on fuel-carbon, as shown in Equation 3.4.

$$EF_i = \frac{99*\sum \Delta C_i.f_C}{\sum \left\{ ER_{CO}\left(\frac{M_C}{M_{CO}}\right) + ER_{CO_2}\left(\frac{M_C}{M_{CO_2}}\right) \right\}} \tag{3.4}$$

ΔC_i are the background corrected, measured, one-minute averaged, emission rates of pollutant 'i', ER_{CO} and ER_{CO_2} are CO and CO_2 emission rates respectively, and f_C is the carbon fraction in the fuel. For BC, the numerator of Equation 3.4 was multiplied by 99:1 to account for dilution. We neglected the carbon contribution from hydrocarbons and PM which creates a 1% to 4% error in calculated emission factors for cookstoves (Roden et al. 2006).

3.2.6 Test-to-test Variability

For six fuel/stove combinations we conducted repeat tests following the same protocol. For these replicates, measured test-integrated emission factor for CO, BC, MAC_{BC}, SSA agree to a factor of two (Figure S2), with average relative standard deviations (one-standard deviation (σ) divided by the average (μ) and expressed as a percentage; RSD=100*σ/μ), across all repeat tests of 17%, 22%, 21%, and 11% for CO, BC, MAC_{BC}, and SSA respectively. This variability likely reflects the challenge of exactly reproducing the same firepower profile between tests.

3.3 Results and Discussion

A time series of one-minute averaged data for a representative test is shown in Figure 3.1. Firepower and MCE are shown in Figure 3.1a; rBC and gravimetric PM emission factors are shown in Figure 3.1b; MAC_{BC} and SSA at 405 nm are shown in Figure 3.1c.
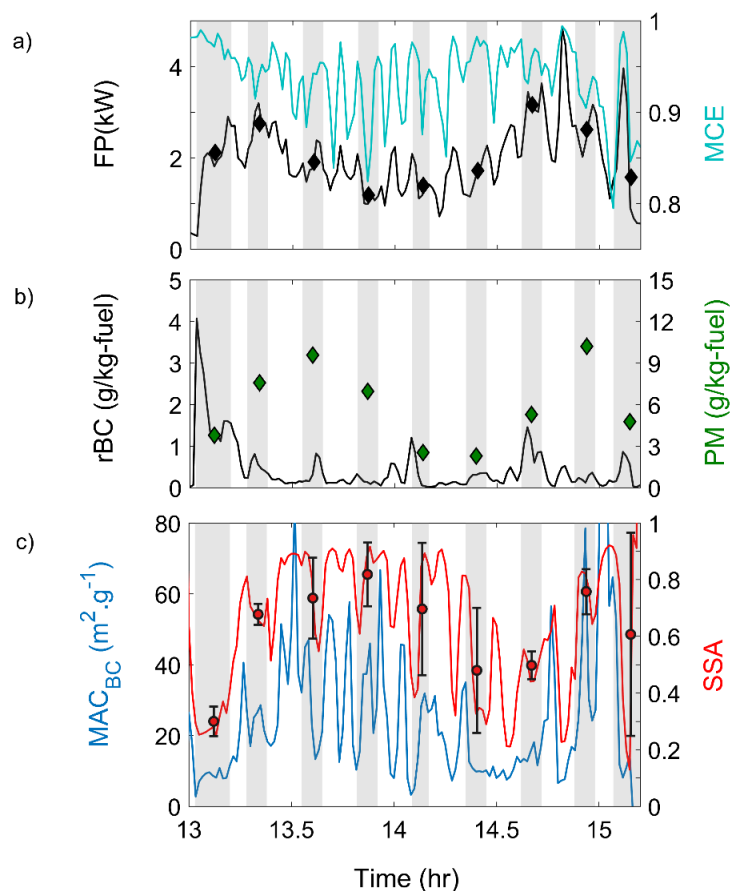
Figure 3.1 Time-series of one-minute averaged data for a representative test: (a) MCE (cyan line) and firepower (FP, black line); (b) filter-based PM emission factors (green data points) and refractory BC mass emission factors (black line); (c) mass absorption cross-section at 405 nm (MAC$_{BC}$, blue line) and single scattering albedo at 405 nm (SSA, red line). Shaded grey areas correspond to firepower steps (the first and last shaded areas correspond to startup and shutdown phases respectively and the rest correspond to firepower holds). Black diamond data points in (a) are average FP over each hold period. Circles in (c) are integrated SSA over each FP hold and error bars correspond to one-standard deviation of the one-minute SSA data over each power hold.

The firepower holds ranged from 1 to 3 kW. The different firepower holds span a wide range of fire conditions; for example, MCE varied between 0.79 and 0.99 for the test shown in Figure 3.1a. As a result, we captured a wide range of optical properties; for this test, the SSA at 405 nm ranged between 0.3 and 0.8 across the firepower holds (one-minute SSA ranged between 0.13 to 0.96). During periods of low SSA, measured MAC$_{BC}$ at 405 nm was ~10 m^2/g, consistent with nascent BC particles (Bond & Bergstrom 2006), but

exceeded 40 m^2/g during periods with strong scattering. We observed similar variability during other tests.

Although the firepower hold periods are intended to be quasi-steady, there is some variability in both fire power and other performance metrics during these periods reflecting the poorly controlled and dynamic nature of cookstove combustion. For example, for all firepower holds periods, the median (interquartile range) firepower RSD was 55% (31% – 98%). We also measured variability in the optical properties during the firepower hold periods; for all firepower hold periods, the 75th percentile of the RSD were 29% for SSA and 60% for MAC_{BC}. The higher variability in MAC_{BC} compared to SSA could be due to the SP2 lower detection limit of ~0.7 fg rBC mass (Schwarz et al. 2010), which increases the variability in SP2 data during tests with low BC emissions (mainly gasifiers and charcoal stoves).

3.3.1 Influence of Stove Technology and Fuels on Optical Properties

In this section, we examine the effects of stove technology and fuel on optical properties (SSA and MAC_{BC}) and on operational metrics (MCE and BC/PM). Figure 3.2 shows the interquartile range for MAC_{BC} at 405 nm (Figure 3.2a), SSA at 405 nm (Figure 3.2b), MCE (Figure 3.2c), and BC/PM (Figure 3.2d) for the different stove categories. The data in Figure 3.2 are a compilation from all the firepower hold and startup/shutdown periods. We removed data points (59 of the original 213 data points) for which: SSA exceeded unity and/or MCE exceeded unity, and/or BC/PM exceeded unity. Almost all the excluded data are from very low emitting stoves (mainly gasifiers and charcoal stoves) for which the signal-to-noise ratio was low, resulting in physically unrealistic values. Data for

operational metrics and optical properties, for all firepower steps, are presented in Table S2.
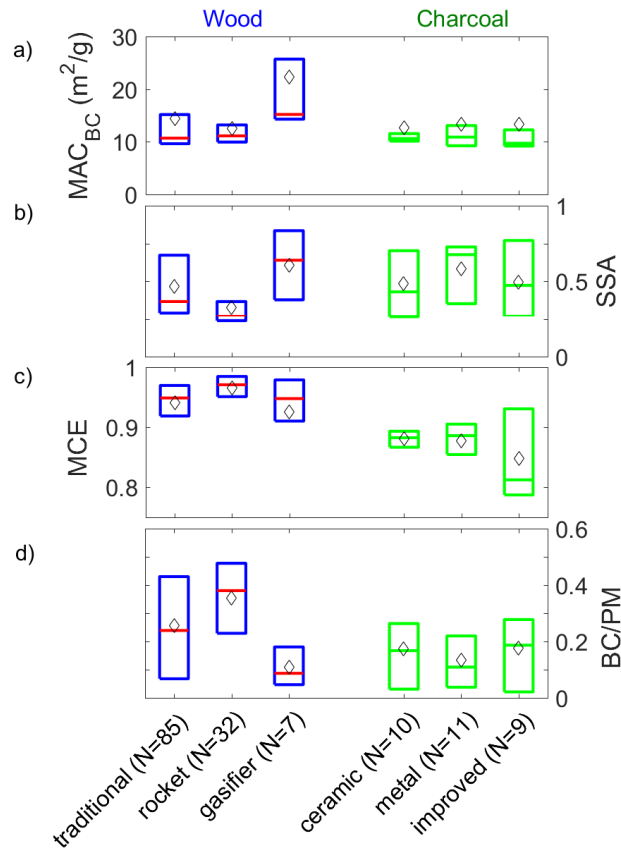
Figure 3.2 Median and interquartile range for: (a) MAC$_{BC}$ at 405 nm, (b) SSA at 405 nm, (c) MCE, and (d) BC/PM from all tests for all firepower holds and startup/shutdown periods (154 total data points). Blue and green colored boxes are data for wood and charcoal stoves respectively. Horizontal line in box is the median and black diamonds are the mean for each stove category. The number of data points in each category is indicated by the numbers N in x-axis labels.

Gasifiers had higher MAC$_{BC}$ than traditional and rocket stoves: average (interquartile range) of 22.3 m^2/g (14.3 – 25.7) for gasifiers (N=7) versus 13.9 m^2/g (9.7 – 14.3) for traditional and rocket stoves (N=117), p-value on two tail t-test of p=0.01. Although there are statistically significant differences in MAC$_{BC}$ between these stove categories, there is almost a factor of two variability within each category. This indicates that the optical properties also depend on other factors in addition than stove technology.

We measured no statistically significant differences in optical properties for stoves operated on different fuels. For example, the average MAC_{BC} at 405 nm was 14.5 m^2/g (9.8 – 14.8) for all wood stoves (N=124) versus 12.9 m^2/g (9.1 – 12.2) for all charcoal (N=30) stoves, p=0.4. Similarly, we found no statistically significant differences between SSA for wood and charcoal stoves. This contrast with laboratory data for biomass burning which shows some relationship between optical properties and fuels (McMeeking et al. 2014). However, we considered a limited range of fuels: we mostly tested Douglas fir (evergreen conifer) and Eucalyptus (myrtle family) woods which might not exhibit significant differences in their emissions.

During firepower holds, one-minute MAC_{BC} and SSA data were more variable for charcoal stoves compared to wood stoves: the 75th percentile of the RSD for MAC_{BC} was 36% for wood stoves compared to 205% for charcoal stoves for all firepower holds (75th percentile of the RSD for SSA was 21% for wood stoves compared to 78% for charcoal stoves). The higher variability in optical properties from charcoal stoves is likely due to the combination of their low emissions and instrument detection limits.

MCE exhibited the strongest dependence on fuel (wood versus charcoal). For example, average (interquartile range) MCE was 0.95 (0.93 – 0.97) for wood (N=124) and 0.87 (0.83 – 0.90) for charcoal stoves (N=30), p<0.001. Similarly, charcoal stoves span a narrower range of operational firepower (FP) compared to wood stoves; FP ranged between 0.6 to 3 kW for charcoal stoves compared to 0.6 to 9 kW for wood stoves, as shown in Figure 3.3.

We also measured difference in BC/PM based on fuel; wood stoves (except gasifiers) have a higher fraction of BC in their emissions: average (interquartile range) BC/PM of 0.28 (0.09 – 0.44) for traditional and rocket stoves (N=117) compared to 0.16 (0.03 – 0.26) for all charcoal stoves (N=30), p<0.001 (Figure 3.2d). However, both charcoal and wood

stoves spanned the same range of BC/PM (Figure 3.3). This was not true for MCE and firepower metrics.

3.3.2 Influence of Operational Metrics on Optical Properties

Given the weak relationships between optical properties and stove technology and fuel, we also investigated relationships between optical properties and three different operational metrics. In Figure 3.3, we plot the SSA, MAC_{BC}, and AAE as a function of MCE, FP, and BC/PM. These types of metrics have been previously used to parametrize variations in optical properties (Pokhrel et al. 2016; Liu et al. 2014; Grieshop et al. 2017).

Optical properties are correlated strongly with BC/PM (Figures 3.3c, 3.3f, 3.3i) with an R^2=0.9 for MAC_{BC} and SSA at 405 nm versus BC/PM, regardless of stove category or operating condition (see Table S3). For example, MAC_{BC} increases as BC/PM decreases and the particles become dominated by non-BC material. An increasing MAC_{BC} means that per unit mass of BC the particle absorbs more light; this phenomenon is commonly referenced to as an absorption enhancement (or lensing). The high correlation of optical properties with BC/PM is expected from Mie theory, if BC and non-BC material form an internal mixture (Bohren & Huffman 1983). We quantified the particle mixing-state using the SP2 lag-time information (Figure 3.4); our data suggest the fraction of BC particles that are thickly coated in a core-shell geometry varies with BC/PM, from 2% at BC/PM>0.4 to more than 25% at low BC/PM (organic-rich emissions).
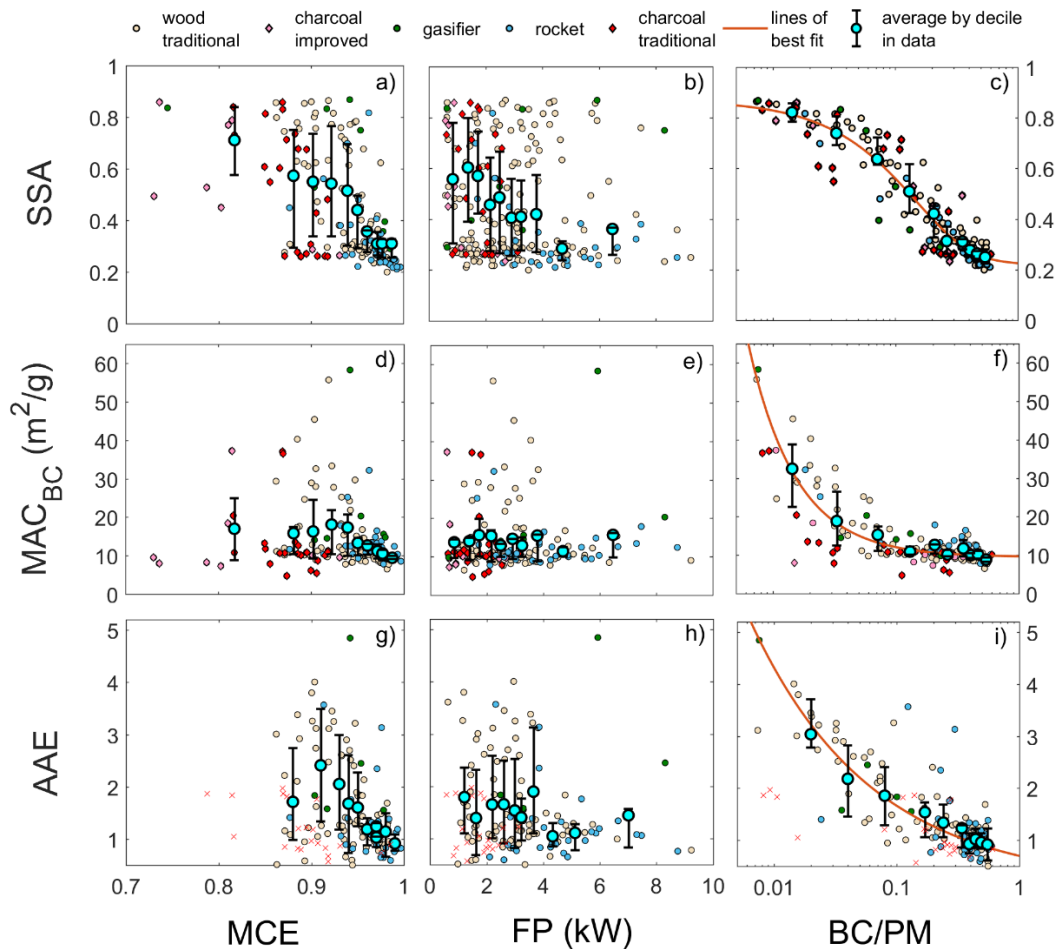
Figure 3.3 Optical properties as a function of different operational metrics. (a) SSA (at 405 nm), (d) MAC$_{BC}$ (at 405 nm), and (g) AAE versus MCE. (b) SSA (at 405 nm), (e) MAC$_{BC}$ (at 405 nm), and (h) AAE versus firepower (FP). (c) SSA (at 405 nm), (f) MAC$_{BC}$ (at 405 nm), and (i) AAE versus BC/PM. Small data points are data over all firepower holds and startup/shutdown periods (circles for wood stoves and diamonds for charcoal stoves), and are colored by stove category. In Figure 3.3i, we did not include charcoal data (marked as red crosses) to parametrize AAE because the AAE data from these stoves had very low signal-to-noise. Filled large cyan circles data points are average of each decile of data to visually highlight trends, and error bars correspond to the interquartile range over each decile. Solid lines in (c), (f), and (i) are our parametrizations for SSA at 405nm (SSA=$0.63e^{-6.7(BC/PM)}$ +$0.24e^{-0.065(BC/PM)}$, R^2=0.94), MAC$_{BC}$ at 405 nm (MAC$_{BC}$ = 0.20(BC/PM)$^{-1.11}$ + 9.5, R^2=0.90), and AAE (AAE = 0.63(BC/PM)$^{-0.41}$ +0.09, R^2=0.80) respectively. The fits were made using MATLAB robust (with a bisquare weighing function) non-linear least square regressions to reduce the influence of outliers (Table S3).

For BC dominated particles (first decile in BC/PM data), we measured average (interquartile range) for SSA at 405 nm, MAC$_{BC}$ at 405 nm, and AAE of: $2.5 \cdot 10^{-1}$ ($2.3 \cdot 10^{-}$

^{1} – $2.8\cdot10^{-1}$), 8.8 m^2/g (8.2 – 9.4), and 0.9 (0.7 – 1.1). These values indicate that BC particles at high BC/PM are largely uncoated, consistent with SP2 data (Bond & Bergstrom 2006; Bergstrom et al. 2002). As BC/PM→0 (organic-dominated emissions) average SSA, MAC$_{BC}$, and AAE increased to: $8.2\cdot10^{-1}$ ($7.9\cdot10^{-1}$ – $2.5\cdot10^{-1}$), 32.5 m^2/g (22.6 – 38.8), and 3.0 (2.75 – 3.7) for the last decile in BC/PM (average BC/PM of $1.5\cdot10^{-2}$).

The factor of roughly three absorption enhancement in the measured MAC$_{BC}$ at 405 nm between BC- and organic-rich emissions is larger than the factor of two usually measured for BC particles heavily coated with non-absorbing material (Schnaiter 2005; Cross et al. 2010; Shiraiwa et al. 2007; Saliba et al. 2016). This suggests the presence of other light-absorbing compounds (BrC) in organic-dominated emissions (BC/PM→0). BrC strongly absorbs at shorter wavelengths (Kirchstetter et al. 2004). Additional evidence for BrC in organic-dominated emissions is the increase in AAE with decreasing BC/PM. The AAE for wood stoves increased from ~0.9 to ~5 with decreasing BC/PM (AAE data for charcoal stoves had very low signal-to-noise: ~40% of charcoal AAE data were negative). Nascent BC particles have an AAE of ~1; AAE>2 usually indicates the presence of BrC (Kirchstetter et al. 2004; Lewis et al. 2008; Sun et al. 2007). Therefore, the trends in AAE indicate that there are increasing amounts of BrC in fresh cookstove emissions with lower BC/PM, consistent with field measurements of cookstove emissions (Roden et al. 2006). In contrast to AAE, we measured a weak dependence of the scattering angstrom exponent (SAE, same as AAE but using scattering coefficients instead of absorption coefficients) with BC/PM; the average ± one-standard deviation SAE was 2.6±0.8 across the range of measured BC/PM.

Optical properties for transient operations, such as startup and shutdown periods, also follow similar trends with BC/PM compared to optical properties measured during

firepower hold periods. This indicates that transient operations (important part of real-world cooking) are represented in the firepower sweep protocol.

Figure 3.3 indicates little correlation of optical properties with MCE ($R^2 < 0.3$) and FP ($R^2 \sim 0.1$). Although MCE has been used to parametrize optical properties of biomass burning emissions (Pokhrel et al. 2016; Liu et al. 2014), it does not explain the variability in optical properties from cookstove emissions measured here. The increases in MAC_{BC}, SSA, and AAE with decreasing MCE are not nearly as sharp as their increase with decreasing BC/PM. FP also does not explain optical properties; we measured an overall increase in SSA with decreasing FP, but Figure 3.3 indicates there are no clear trends between MAC_{BC} and AAE with FP.

3.3.3 Parametrizing Optical Properties with BC/PM

The strong dependence of optical properties with BC/PM is expected from Mie theory given the measured mixing between BC and non-BC material (Figure 3.4). Coating around BC particles creates lensing. At high organic loadings there is also BrC. Both of these factors contribute to the measured absorption enhancement. We therefore investigated whether Mie theory quantitatively explains the measured changes in MAC_{BC} with BC/PM.

In Figure 3.4 we compare the measured MAC_{BC} to Mie predictions for different particle mixing-states and with and without BrC (5 different cases, detailed in the caption for Figure 3.4) at 405 nm. Some of the cases represent current model treatment of the optical properties from cookstove emissions (e.g., internal mixture/external mixture of all BC and non-BC material and with/without BrC) (Kodros et al. 2015).
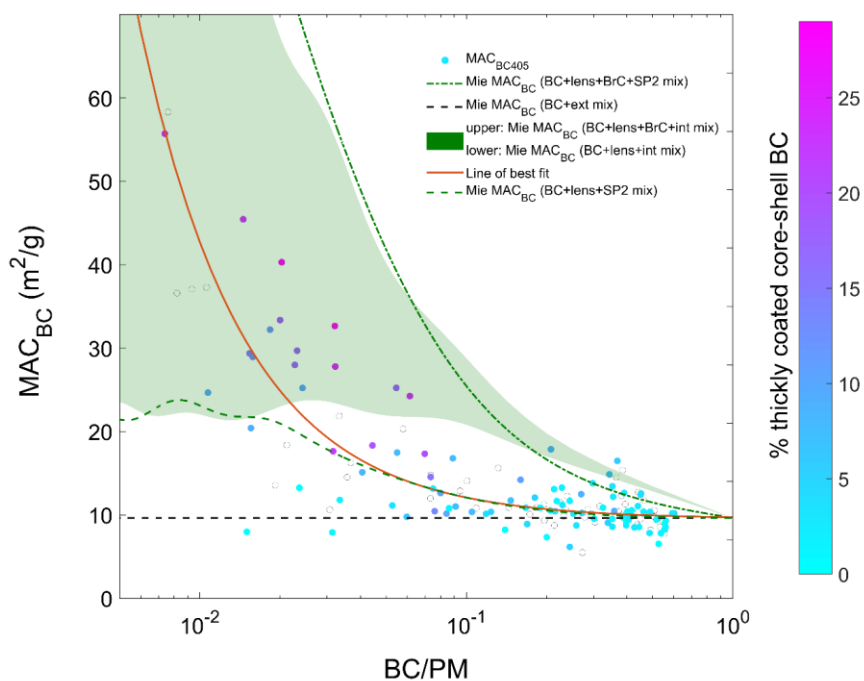
Figure 3.4 MAC$_{BC}$ at 405 nm versus the BC/PM for each firepower hold. The data are colored by the SP2 positive lag-time information (when available). A value of 0% indicates an external mixture of BC and non-BC materials; a value of 100% indicates that all the BC particles are thickly coated. The solid brown line is our parametrization (see Figure 3.3). Five different Mie MAC$_{BC}$ calculations are also shown: (1) assuming complete internal mixture of BC and non-BC material and no BrC ({BC+lens+int mix}: lower limit of green shaded area), (2) same as previous case but with BrC ({BC+lens+BrC+int mix}: upper limit of green shaded area), (3) assuming a mixing-state measured by the SP2 and no BrC ({BC+lens+SP2 mix}: lower dashed green line), (4) same as previous case but with BrC ({BC+lens+BrC+SP2 mix}: upper green dashed line), and finally (5) assuming an external mixture of BC and non-BC materials and no BrC ({BC+ext mix}: horizontal dashed black line). See SI for additional details of Mie theory calculations.

Figure 3.4 demonstrates that Mie theory reproduces some of the trends in the measured optical properties. However, as expected based on our previous discussion, the data fall into different regimes. For examples, the Mie predicted MAC$_{BC}$ using the BC mixing-state inferred from SP2 measurements and assuming the non-BC material is purely scattering ({BC+lens+SP2 mix} case, Figure 3.4) agrees with the measured increase in MAC$_{BC}$ from high to low BC/PM until a BC/PM ~0.05. This supports the conclusion that over this range

66

of BC/PM the measured absorption enhancement is driven by lensing. However, when BC/PM<0.05 (organic-dominated emissions), the measured MAC_{BC} increasingly deviates from the Mie predicted MAC_{BC} case, indicating increased contribution of BrC to the measured absorption.

Current model treatments of the aerosol optical properties of cookstove emissions assume a completely internal mixture of BC and non-BC material and estimate the absorption of BrC using parametrizations developed for biomass burning (Kodros et al. 2015) ({BC+lens+BrC+int mix} case, Figure 3.4). However, the range of BC/PM measured from cookstove emissions in field studies is ~0.1 – 0.3 (Bond et al. 2013), therefore our data suggest that lensing likely dominates absorption enhancement and not BrC in real-world emissions. If there BrC contribution to absorption is small, then models may be overestimating direct radiative impacts from stove emissions.

The fact that Mie theory does not perfectly reproduce the data is not surprising. It reflects the underlying uncertainties in mixing-state and BrC used as input for the model. Given these uncertainties, we developed semi-empirical parameterizations for intensive optical properties: MAC_{BC}, SSA, and AAE of fresh stove emissions as a function of BC/PM. The parameterizations are semi-empirical because they are motivated by the strong relationship between optical properties and BC/PM predicted by Mie theory. These parameterizations are designed for use with emissions inventories and climate models to estimate the optical properties (and subsequent forcing) from fresh emissions. BC/PM is a useful parameter because existing inventories contain both elemental carbon (EC) and PM emissions data, i.e., the inputs for the parametrizations are readily available.

Our parametrizations for SSA (at 405 nm), MAC_{BC} (at 405 nm), and AAE versus BC/PM are shown in Figure 3.3. MAC_{BC}, SSA, and AAE are strongly correlated with

BC/PM (R^2=0.9 for MAC$_{PM}$ and SSA versus BC/PM and R^2=0.80 for AAE versus BC/PM). Parametrizations for MAC$_{PM}$ (at 405 and 532 nm), MAC$_{BC}$ (at 405 and 532 nm), SSA (at 405 and 532 nm), and AAE are listed in Table S3.

In the limit of BC/PM=1 (pure BC particles), our parametrizations return values that agree with literature values for nascent BC (Bond & Bergstrom 2006). For example, in this limit, the MAC$_{BC}$ is 9.5 m^2/g at 405 nm (Figure 3.3f) and the AAE is 0.7 (Figure 3.3j). The limit for AAE is somewhat less than 1, the value associated with pure BC particles (Bergstrom et al. 2002; Schnaiter 2005; Kirchstetter et al. 2004).

Our parametrizations are based on laboratory data. Previous studies have raised concerns about the representativeness of laboratory data (Roden et al. 2009; Chen et al. 2012; Johnson et al. 2008). We therefore compared the prediction using our new parametrization to published field data (Roden et al. 2006; Grieshop et al. 2017).

In Figure 3.5, we compare our parametrizations to literature values for MAC$_{PM}$ and SSA at 532 nm. Our parametrization predict the SSA measured by Roden et al.(2006) for traditional stoves in Honduras to within 10% (R^2=0.96) (Roden et al. 2006). Our parametrizations somewhat underestimate their reported MAC$_{PM}$ by 30% (R^2=0.94). Our parametrization overestimate the MAC$_{PM}$ values from fresh stove emissions reported in Grieshop et al.(2017) by 18% (R^2=0.7) (Grieshop et al. 2017). We believe that this good agreement is because we are focused on intensive optical properties; the concerns raised by previous laboratory-field comparisons are based on comparisons of absolute emissions rates (extensive properties) (Roden et al. 2009; Johnson et al. 2008).
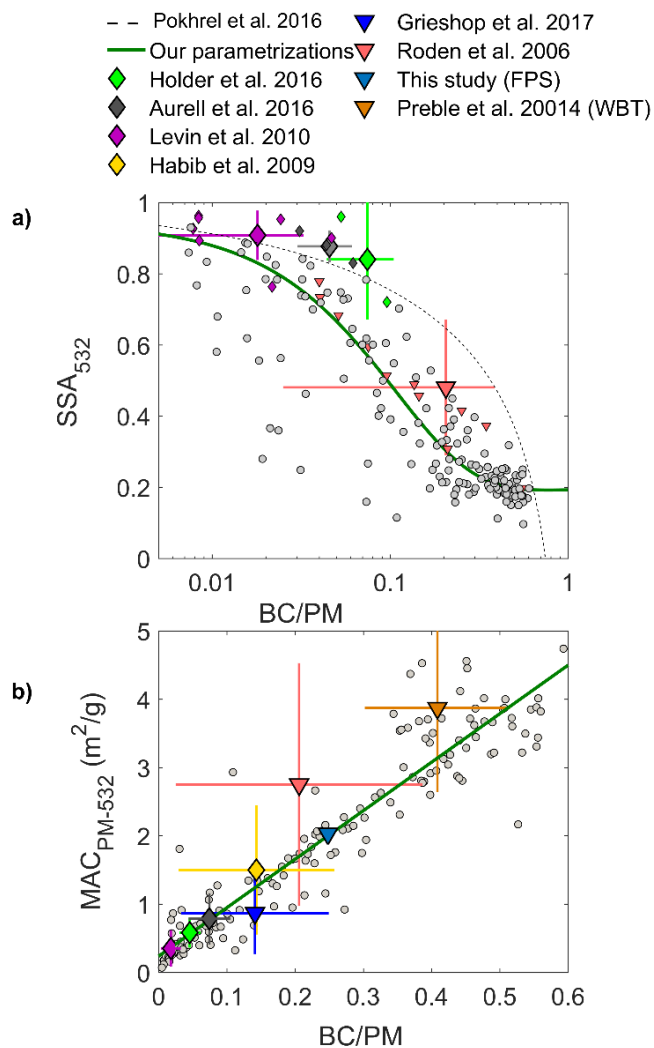
Figure 3.5 Comparison of our parametrizations for (a) SSA and (b) MAC_PM at 532 nm with literature data (Pokhrel et al. 2016; Holder et al. 2016; Aurell et al. 2015; Levin et al. 2010; Habib et al. 2008; Grieshop et al. 2017; Roden et al. 2006; Preble et al. 2014). Solid green lines are parametrizations derived from our data (small grey filled circles) for SSA and MAC_PM at 532 nm (Equations in Table S3). Large symbols are average data from different published studies with error bars being the one-standard deviation in the data. Triangular symbols indicate cookstoves; diamond symbols indicate biomass burning. We compared our measured data to optical properties from biomass burning emissions collected both in the laboratory (Pokhrel et al. 2016; Holder et al. 2016; Habib et al. 2008; Levin et al. 2010) and in the field (Holder et al. 2016). Our MAC_PM parametrization explains the large variability in literature data (R²=0.8, between our MAC_PM parametrization and average literature data). Also shown in (a) is the parametrization of SSA (at 532 nm) from Pokhrel et al. (2016) derived for biomass burning (dashed black line) (Pokhrel et al. 2016). FPS is firepower sweep protocol and WBT is water boil test.

3.3.4 Climate and Health Potential Implications

In this section we estimate the direct radiative forcing of fresh stove emissions for different stove technologies by combining our new parametrizations for intensive optical properties with absolute emissions data measured by field studies. For this analysis, we compiled field emissions data for 156 individual stoves from 6 studies conducted in 5 countries: 106 traditional wood stoves, 23 rocket stoves, 17 gasifiers, 7 traditional charcoal stoves, and 3 improved charcoal stoves (Roden et al. 2006; Grieshop et al. 2017; Wathore et al. 2017; Du et al. 2017; Coffey et al. 2017), (Eilenberg et al., *in preparation*). These data are listed in Table S4.

First, we only consider the effects of aerosol emissions on direct radiative forcing by calculating the SFE (Equation 3.3) for 5 different stove categories: traditional, rocket-style, and gasifier wood stoves as well as traditional and improved charcoal stoves. To estimate MAC_{PM} and SSA form particle-phase emissions, we used the average BC/PM measured in the field as input for our parametrizations. By using field inputs for our parametrizations, we hope to avoid previously reported biases in laboratory emissions data. Finally, we converted SFE to an activity basis (hours cooking; SFE_{cook}).

$$SFE_{cook} = SFE.PM.C_{fuel} \qquad (3.5)$$

Where PM are emission factors (g/kg-fuel) and C_{fuel} is the fuel consumption rate (in kg-fuel/hr, a measure of stove thermal efficiency), both based on field data. We derived fuel consumption rates from literature data: average ± one-standard deviation of 1.3±0.3 kg/hr for traditional wood stoves, 0.8±0.2 kg/hr for forced-draft gasifiers, 0.9±0.4 kg/hr for rocket-style stoves, 0.5±0.3 kg/hr for traditional charcoal stoves, and 0.3±0.2 kg/hr for improved charcoal stoves (Coffey et al. 2017; Garland et al. 2017; Wathore et al. 2017).

SFE$_{cook}$ (at 532 nm) and PM emissions rates for the different stove categories are shown in Figure 3.6. The data are rank-ordered from highest to lowest average SFE$_{cook}$, which also coincide with highest to lowest average PM emission rates.

PM emissions from traditional wood stoves have the largest positive radiative forcing with an average (interquartile range) of SFE$_{cook}$ = +0.7 W/nm-hr (+0.3 – +0.7) (N=106) as well as the highest PM emission rate: 10.4 g/hr (6.9 – 12.5). Since exposure to PM is a primary driver for air pollution health effects (Di et al. 2017), PM emission is a reasonable indicator of potential health impacts.

We present SFE$_{cook}$ values for so-called improved technologies, including rocket and gasifier stoves, Figure 3.6. Comparing their performance to traditional stoves provides an indication of the potential climate and health impacts associated with stove replacement policies. Rocket-style stoves have, on average, about 60% lower PM emission rates compared to traditional stoves (p<0.001). Therefore, we expect some health benefits from deployment of rocket-style stoves. However, the average SFE$_{cook}$ for rocket stoves is only 18% lower than traditional stoves, due to their higher BC/PM (average BC/PM of 0.26 for rocket stoves versus 0.13 for traditional stoves). This difference is not statistically significant (p=0.5); therefore, it is not clear if there are climate benefits associated with switching from traditional to rocket stoves. We predict similar results for gasifier stoves.
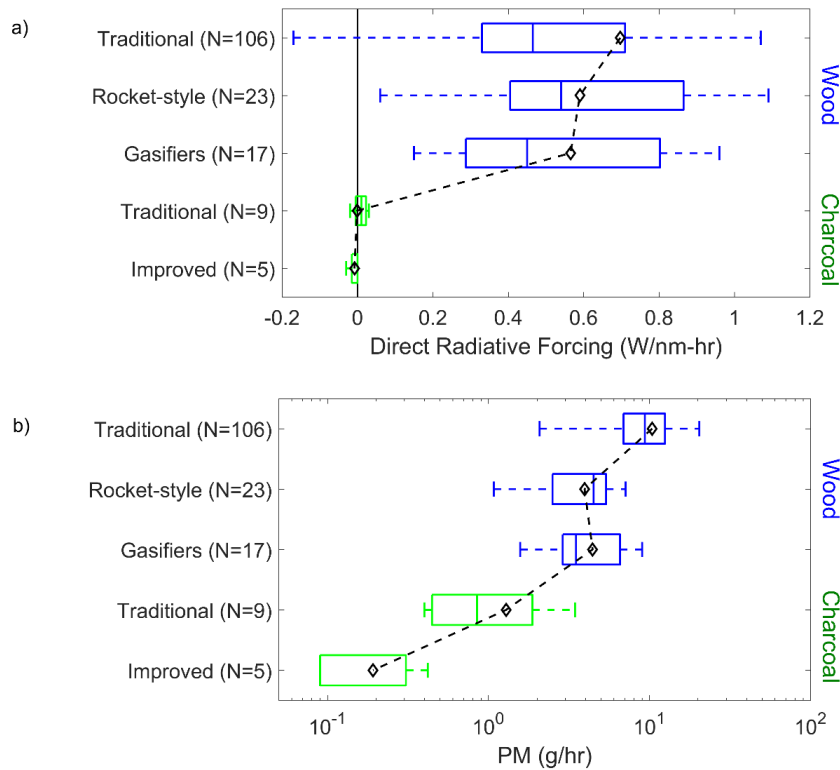
Figure 3.6 Box-whisker plots of (a) direct radiative forcing (SFE$_{cook}$) and (b) PM emission rates (on a per-hour cooking basis) for different stove categories. PM emissions data are from field measurements reported in the literature (Roden et al. 2006; Grieshop et al. 2017; Wathore et al. 2017; Du et al. 2017; Coffey et al. 2017), (Eilenberg et al., *in preparation***). Boxes are the interquartile range and the whiskers extend to approximately ±2.7σ of the data. The vertical lines in each box are the median and diamonds are the average for each stove category. The dashed black lines connect average values and is intended to guide the eye. The number of stoves in each category is indicated by "N" in the y-label axis. The vertical solid black line in (a) is the zero-net direct radiative effect. Positive values indicate net-warming from emissions and negative values indicate net-cooling from emissions.**

Compared to the other technologies, charcoal stoves appeared to have the most potential health and climate benefits. Charcoal stoves had the lowest PM emissions: 1.3 g/hr (0.4 – 1.9) for traditional stoves (N=7) and 0.2 g/hr (0.1 – 0.3) for improved stoves (N=3). Charcoal stoves also had the lowest direct radiative forcing (from particle-phase emissions) compared to other stove categories; average SFE$_{cook}$ was ~0.00 W/nm-hr (-0.01 – +0.02) for traditional charcoal stoves and ~0.00 W/nm-hr (-0.02 – +0.00) for improved charcoal stoves.

In addition to particles, cookstoves also emit greenhouse gases such as CO_2, CO, and CH_4, and non-methane organic carbon (NMOC). A comparison of gas and particle emissions from the different stove technologies on a CO_{2-eq} basis is shown in Figure S4. For this analysis we assume that the wood is non-renewably harvested, i.e. we included CO_2 emissions. Greenhouse gas emissions contribute substantially to the direct radiative forcing. If we include greenhouse gas emissions, we estimate 20% and 30% reductions in CO_{2-eq} emission from rocket-style and gasifier stoves compared to traditional stoves due to improved combustion and thermal efficiencies. Therefore, there appears to be some climate benefits associated with switching to these technologies.

Figure S4 indicates that greenhouse gas emissions dominate the direct radiative forcing from charcoal stoves. However, CO_{2-eq} emissions from charcoal stoves are more than 50% lower (cleaner) than gasifiers; therefore, charcoal stoves should have the most climate and health benefits, at least at the point of use. The additional emissions associated with charcoal production are not considered here. Substantial emissions are generated during charcoal production, which contribute to the lifecycle impacts of this technology on health and climate (Bertschi et al. 2003).

In this study we used metrics such as the SFE_{cook} and CO_{2-eq} to compare the direct radiative forcing of different stove technologies at a global scale. However, stove emissions also contribute to regional changes, especially in the southeast Asia, India, and Africa (Bond et al. 2013). For example, BC hotspots have been shown to invigorate convection and weaken subsidence, thereby altering precipitation patterns (Menon et al. 2002; Ramanathan et al. 2001). Our analysis suggests that improved stoves likely will not reduce these regional impacts. However, more work is needed to study regional impacts of changing cookstove technologies.

3.4 References

Andreae, M.O. & Gelencsér, A., 2006. Black carbon or brown carbon? The nature of light-absorbing carbonaceous aerosols. *Atmospheric Chemistry and Physics*, 6(3), pp.3419–3463.

Aurell, J., Gullett, B.K. & Tabor, D., 2015. Emissions from southeastern U.S. Grasslands and pine savannas: Comparison of aerial and ground field measurements with laboratory burns. *Atmospheric Environment*, 111, pp.170–178.

Bergstrom, R.W., Russell, P.B. & Hignett, P., 2002. Wavelength Dependence of the Absorption of Black Carbon Particles: Predictions and Results from the TARFOX Experiment and Implications for the Aerosol Single Scattering Albedo. *Journal of atmospheric Sciences*, pp.567–577.

Bertschi, I.T. et al., 2003. Trace gas emissions from the production and use of domestic biofuels in Zambia measured by open-path Fourier transform infrared spectroscopy. *Journal of Geophysical Research: Atmospheres*, 108(D13), p.n/a-n/a. Available at: http://doi.wiley.com/10.1029/2002JD002158.

Bohren, C.F. & Huffman, D.R., 1983. *Absorption and scattering of light by small particles*.

Bond, T.C. et al., 2013. Bounding the role of black carbon in the climate system: A scientific assessment. *Journal of Geophysical Research: Atmospheres*, 118(11), pp.5380–5552.

Bond, T.C. & Bergstrom, R.W., 2006. Light Absorption by Carbonaceous Particles: An Investigative Review. *Aerosol Science and Technology*, 40(1), pp.27–67.

Cappa, C.D. et al., 2012. Radiative absorption enhancements due to the mixing state of atmospheric black carbon. *Science (New York, N.Y.)*, 337(6098), pp.1078–81. Available at: http://www.ncbi.nlm.nih.gov/pubmed/22936774 [Accessed July 15, 2014].

Chen, Y. & Bond, T.C., 2010. Light absorption by organic carbon from wood combustion. *Atmospheric Chemistry and Physics*, 9, pp.1773–1787. Available at: http://www.atmos-chem-phys-discuss.net/9/20471/2009/.

Chen, Y., Roden, C.A. & Bond, T.C., 2012. Characterizing biofuel combustion with Patterns of Real-Time Emission Data (PaRTED). *Environmental Science and Technology*, 46(11), pp.6110–6117.

Chylek, P. & Wong, J., 1995. Effect of absorbing aerosols on global radiation budget. *Geophysical Research Letters*, 22, pp.929–931. Available at: http://doi.wiley.com/10.1029/95GL00800.

Coffey, E.R. et al., 2017. Implications of new emission factors and efficiencies from in-field measurements of traditional and improved cookstoves. *Environ*.

Cross, E.S. et al., 2010. Soot Particle Studies—Instrument Inter-Comparison—Project Overview. *Aerosol Science and Technology*, 44, pp.592–611.

Di, Q. et al., 2017. Air Pollution and Mortality in the Medicare Population. *New England Journal of Medicine*, 376(26), pp.2513–2522. Available at: http://www.nejm.org/doi/10.1056/NEJMoa1702747.

Du, W. et al., 2017. Comparison of air pollutant emissions and household air quality in rural homes using improved wood and coal stoves. *Atmospheric Environment*, 166, pp.215–223.

Fuller, K.A., Malm, W.C. & Kreidenweis, S.M., 1999. Effects of mixing on extinction by carbonaceous particles. *Journal of Geophysical Research: Atmospheres*, 104(D13), pp.15941–15954. Available at: http://dx.doi.org/10.1029/1998JD100069.

Garland, C. et al., 2017. Black carbon cookstove emissions: A field assessment of 19 stove/fuel combinations. *Atmospheric Environment*, 169, pp.140–149.

Grieshop, A.P. et al., 2017. Emission factors of health- and climate-relevant pollutants measured in home during a carbon-finance-approved cookstove intervention in rural India. *GeoHealth*, 1(5), pp.222–236. Available at: http://doi.wiley.com/10.1002/2017GH000066.

Gysel, M. et al., 2011. Effective density of Aquadag and fullerene soot black carbon reference materials used for SP2 calibration. *Atmospheric Measurement Techniques*, 4(12), pp.2851–2858.

Habib, G. et al., 2008. Chemical, microphysical and optical properties of primary particles from the combustion of biomass fuels. *Environmental Science and Technology*, 42(23), pp.8829–8834.

Holder, A.L. et al., 2016. Particulate matter and black carbon optical properties and emission factors from prescribed fires in the southeastern United States. *Journal of Geophysical Research*, 121(7), pp.3465–3483.

International Organization for Standardization, 2012. IWA 11: 2012 Guidelines for evaluating cookstove performance. , (February 2012). Available at: http://www.pciaonline.org/files/ISO-IWA-Cookstoves.pdf.

Jacobson, M.Z., 2001. Global direct radiative forcing due to multicomponent anthropogenic and natural aerosols. *Journal of Geophysical Research: Atmospheres*, 106(D2), pp.1551–1568. Available at: http://doi.wiley.com/10.1029/2000JD900514.

Johnson, M. et al., 2008. In-field greenhouse gas emissions from cookstoves in rural Mexican households. *Atmospheric Environment*, 42(5), pp.1206–1222.

Just, B., Rogak, S. & Kandlikar, M., 2013. Characterization of ultrafine particulate matter from traditional and improved biomass cookstoves. *Environmental Science and Technology*, 47(7), pp.3506–3512.

Kirchstetter, T.W., Novakov, T. & Hobbs, P. V., 2004. Evidence that the spectral dependence of light absorption by aerosols is affected by organic carbon. *Journal of Geophysical Research D: Atmospheres*, 109(21).

Kodros, J.K. et al., 2015. Uncertainties in global aerosols and climate effects due to biofuel emissions. *Atmospheric Chemistry and Physics*, 15(15), pp.8577–8596.

Levin, E.J.T. et al., 2010. Biomass burning smoke aerosol properties measured during Fire Laboratory at Missoula Experiments (FLAME). *Journal of Geophysical Research Atmospheres*, 115(18).

Lewis, K. et al., 2008. Strong spectral variation of biomass smoke light absorption and single scattering albedo observed with a novel dual-wavelength photoacoustic instrument. , 113, pp.1–14.

Lim, S.S. et al., 2012. A comparative risk assessment of burden of disease and injury attributable to 67 risk factors and risk factor clusters in 21 regions, 1990-2010: A systematic analysis for the Global Burden of Disease Study 2010. *The Lancet*, 380(9859), pp.2224–2260.

Liu, S. et al., 2014. Aerosol single scattering albedo dependence on biomass combustion efficiency: Laboratory and field studies. *Geophysical Research Letters*, 41(2), pp.742–748.

MacCarty, N. et al., 2008. A laboratory comparison of the global warming impact of five major types of biomass cooking stoves. *Energy for Sustainable Development*, 12(2), pp.56–65.

McMeeking, G.R. et al., 2014. Impacts of nonrefractory material on light absorption by aerosols emitted from biomass burning. *Journal of Geophysical Research*, 119(21), p.12,272-12,286.

Menon, S. et al., 2002. Climate Effects of Black Carbon Aerosols in China and India. *Science*, 297(5590), pp.2250–2253. Available at: http://www.jstor.org/stable/3832378%5Cnhttp://www.jstor.org/stable/3832378.

Moteki, N. & Kondo, Y., 2010. Dependence of Laser-Induced Incandescence on Physical Properties of Black Carbon Aerosols: Measurements and Theoretical Interpretation. *Aerosol Science and Technology*, 44(8), pp.663–675.

Pokhrel, R.P. et al., 2016. Parameterization of single-scattering albedo (SSA) and absorption Ångström exponent (AAE) with EC/OC for aerosol emissions from biomass burning. *Atmospheric Chemistry and Physics*, 16(15), pp.9549–9561.

Preble, C. V. et al., 2014. Emissions and climate-relevant optical properties of pollutants emitted from a three-stone fire and the berkeley-darfur stove tested under laboratory conditions. *Environmental Science and Technology*, 48(11), pp.6484–6491.

Ramanathan, V. et al., 2001. Aerosols, climate, and the hydrological cycle. *Science (New York, N.Y.)*, 294(5549), pp.2119–24. Available at:

http://www.ncbi.nlm.nih.gov/pubmed/11739947 [Accessed July 10, 2014].

Roden, C.A. et al., 2006. Emission factors and real-time optical properties of particles emitted from traditional wood burning cookstoves. *Environmental Science and Technology*, 40, pp.6750–6757.

Roden, C.A. et al., 2009. Laboratory and field investigations of particulate and carbon monoxide emissions from traditional and improved cookstoves. *Atmospheric Environment*, 43(6), pp.1170–1181.

Saleh, R., M. Marks, J. Heo, P.J.Adams, N.M. Donahue, A.L.R., 2015. Contribution of brown carbon and lensing to the direct radiative effect of carbonaceous aerosols from biomass and biofuel burning emissions. *J. Geophys. Res. Atmos.*, pp.1–12.

Saleh, R. et al., 2014. Brownness of organics in aerosols from biomass burning linked to their black carbon content. *Nature Geoscience*, 7, pp.1–4. Available at: http://www.nature.com/doifinder/10.1038/ngeo2220.

Saliba, G. et al., 2016. Optical properties of black carbon in cookstove emissions coated with secondary organic aerosols: Measurements and modeling. *Aerosol Science and Technology*, 50(11), pp.1–13. Available at: https://www.tandfonline.com/doi/full/10.1080/02786826.2016.1225947.

Schnaiter, M., 2005. Absorption amplification of black carbon internally mixed with secondary organic aerosol. *Journal of Geophysical Research*, 110(D19), p.D19204. Available at: http://doi.wiley.com/10.1029/2005JD006046 [Accessed August 11, 2014].

Schwarz, J.P. et al., 2006. Single-particle measurements of midlatitude black carbon and light-scattering aerosols from the boundary layer to the lower stratosphere. *Journal of Geophysical Research*, 111(D16), p.D16207. Available at: http://doi.wiley.com/10.1029/2006JD007076 [Accessed April 12, 2015].

Schwarz, J.P. et al., 2010. The Detection Efficiency of the Single Particle Soot Photometer. *Aerosol Science and Technology*, 44(8), pp.612–628. Available at: http://www.tandfonline.com/doi/abs/10.1080/02786826.2010.481298 [Accessed April 24, 2015].

Sedlacek, A.J. et al., 2012. Determination of and evidence for non-core-shell structure of particles containing black carbon using the Single-Particle Soot Photometer (SP2). *Geophysical Research Letters*, 39.

Shiraiwa, M. et al., 2007. Evolution of mixing state of black carbon in polluted air from Tokyo. *Geophysical Research Letters*, 34.

Subramanian, R. et al., 2010. Black carbon over Mexico: the effect of atmospheric transport on mixing state, mass absorption cross-section, and BC/CO ratios. *Atmospheric Chemistry and Physics*, 9, pp.219–237.

Sun, H., Biedermann, L. & Bond, T.C., 2007. Color of brown carbon: A model for

ultraviolet and visible light absorption by organic carbon aerosol. *Geophysical Research Letters*, 34(17).

Wathore, R., Mortimer, K. & Grieshop, A.P., 2017. In-Use Emissions and Estimated Impacts of Traditional, Natural- and Forced-Draft Cookstoves in Rural Malawi. *Environmental Science and Technology*, 51(3), pp.1929–1938.

CHAPTER 4
COMPARISON OF GASOLINE DIRECT-INJECTION (GDI) AND PORT FUEL INJECTION (PFI) VEHICLE EMISSIONS: EMISSION CERTIFICATION STANDARDS, COLD-START, SECONDARY ORGANIC AEROSOL FORMATION POTENTIAL, AND POTENTIAL CLIMATE IMPACTS[3]

Abstract

Recent increases in the Corporate Average Fuel Economy standards have led to widespread adoption of vehicles equipped with gasoline direct injection (GDI) engines. Changes in engine technologies can alter emissions. To quantify these effects, we measured gas- and particle-phase emissions from eighty-two light duty gasoline vehicles recruited from the California in-use fleet tested on a chassis dynamometer using the cold-start unified cycle. The fleet included 15 GDI vehicles, including 8 GDIs certified to the most stringent emissions standard, super-ultra-low-emission vehicles (SULEV). We quantified the effects of engine technology, emission certification standards, and cold-start on emissions. For vehicles certified to the same emissions standard, there is no statistical difference of regulated gas-phase pollutant emissions between PFIs and GDIs. However, GDIs had, on average, a factor of two higher particulate matter (PM) mass emissions than PFIs due to higher elemental carbon (EC) emissions. SULEV certified GDIs have a factor of two lower PM mass emissions than GDIs certified as ultra-low-emission vehicles (3.0 ± 1.1 mg/mi versus 6.3 ± 1.1 mg/mi) suggesting improvements in engine design and/or calibration.

Comprehensive organic speciation revealed no statistically significant differences in the composition of the volatile organic compounds emissions between PFI and GDIs, including benzene, toluene, ethylbenzene, and xylenes (BTEX). Therefore, the secondary organic aerosol and ozone formation potential of the exhaust does not depend on engine technology. Cold-start contributes a larger fraction of the total unified cycle emissions for vehicles meeting more stringent emission standards. Organic gas emissions were the most sensitive to cold-start compared to the other pollutants tested here. There were no statistically significant differences in the effects of cold-start on GDIs and PFIs. For our test fleet, the measured 14.5% decrease in CO_2 emissions from GDIs was much greater than the potential climate forcing associated with higher black carbon emissions. Thus switching from PFI to GDI vehicles will likely lead to a reduction in net global warming.

4.1 Introduction

Tailpipe emissions from light-duty gasoline vehicles are an important source of urban air pollution (Borbon et al., 2013; May et al., 2014; Worton et al., 2014). To reduce these emissions, vehicles have been required to meet increasingly strict emissions standards for particulate matter (PM), carbon monoxide (CO), total hydrocarbons (THC), and nitrogen oxides (NO_x = nitric oxide NO + nitrogen dioxide NO_2) over the last several decades. This has pushed the automotive industry to improve both engine design, engine calibration, and after-treatment technologies.

The Environmental Protection Agency (EPA) and the National Highway Traffic Safety Administration (NHTSA) issued a federal final rule to reduce greenhouse gas (GHG) tailpipe emissions and increase the fuel economy of light-duty gasoline vehicles manufactured starting in 2017 (EPA and DOT, 2012). Gasoline direct injection (GDI)

engines have higher fuel economy compared to the more widely used port fuel injection (PFI) engines (Zhao, Lai, & Harrington, 1999). Although real-world fuel economy improvements from GDI technology alone are close to 1.5%, they can reach 8% by downsizing and turbocharging the engine, which can be achieved on GDI engines without loss of power compared to PFI engines (National Research Council, 2011). As a result, the market share of GDI-equipped vehicles has increased dramatically over the past decade and is expected to reach 50% of new gasoline vehicles sold in 2016 (Stacy C. Davis, Susan E. Williams, Robert G. Boundy, & Sheila Moore, 2015; Zhang & McMahon, 2012; Zimmerman, Wang, Jeong, Ramos, et al., 2016). Widespread adoption of new engine technologies raises concerns about changes in emissions and their effects on air quality and the climate.

Recent studies have compared emissions of PFI and GDI vehicles, including particle number and mass (Bahreini et al., 2015; Fushimi et al., 2016; Khalek, Bougher, & Jetter, 2010; Liang et al., 2013; Zhang & McMahon, 2012; Zimmerman, Wang, Jeong, Ramos, et al., 2016), gaseous pollutants (Cole, Poola, & Sekar, 1998; Myung et al., 2012), and non-methane organic gas (NMOG) composition for a limited number of compounds (Zhang & McMahon, 2012 ; Liang et al., 2013 ; Cole et al., 1998 ; Myung et al., 2012). However, many of these studies only tested very small fleets (including single vehicles), making it difficult to draw conclusions about the effects of widespread adoption of GDI vehicles on the aggregate emissions from the entire vehicle fleet because of the vehicle-to-vehicle variability in tailpipe emissions (May et al., 2014). There is substantial variability in vehicle-to-vehicle emissions due to differences in engine design (PFI, spray-guided GDI, wall-guided GDI, etc.), engine calibration (spark timing, valve timing, etc.), emission control technologies, and vehicle age and maintenance history (May et al., 2014).

Previous studies have shown that GDI engines have higher PM mass (Bahreini et al., 2015; Khalek et al., 2010; Liang et al., 2013; Zimmerman, Wang, Jeong, Ramos, et al., 2016) and particle number (Braisher, Stone, & Price, 2010; Zhang & McMahon, 2012) emissions than PFI engines. A significant fraction of the GDI PM emissions is black carbon (BC), formed from incomplete fuel volatilization and mixing. GDI vehicles may have trouble meeting the recently promulgated Federal Tier3 and California LEV3 PM emissions standards. Manufacturers are investigating improved GDI engine designs and calibrations to reduce PM emissions; for example, different fuel injection strategies (spray versus wall-guided) have been shown to influence PM emissions (Bahreini et al., 2015; Choi et al., 2012; Price, Stone, Collier, & Davies, 2006; Zhang & McMahon, 2012). Gasoline particulate filters can also be used to control PM emissions from GDIs (Chan et al., 2013; Mamakos, Martini, Marotta, & Manfredi, 2013; Saito et al., 2011; Seo, Lee, Choi, Kim, & Yoon, 2013; Spiess, Wong, Richter, & Klingmann, 2013). Relatively little data have been reported for GDIs that meet the most stringent emission standards: super-ultra-low-emission vehicles (SULEV) and partial-zero-emission vehicles (PZEV) (Bahreini et al., 2015; Karavalakis et al., 2015; Li et al., 2014; Zhang & McMahon, 2012).

Improvements in engine and catalytic converter designs have dramatically lowered tailpipe emissions. For modern vehicles, the vast majority of emissions occur immediately after cold-start before the catalytic converter has reached operating temperature (Bahreini et al., 2015; Drozd et al., 2016; George et al., 2015; Li et al., 2014). Advances in engine technologies have also significantly decreased cold-start emissions, but a comparison of cold-start effects for gas- and particle-phase emissions from PFI and GDI equipped vehicles has not been reported.

PFI and GDI equipped vehicles must meet the same emissions standards, but these standards only apply to regulated emissions metrics. For example, regulations limit the total nonmethane organic gas emissions, but not their composition, except for a few species such as formaldehyde. The composition of the organic gas emissions can have important effects on ozone and secondary organic aerosol (SOA) formation (Kirchstetter, Singer, Harley, Kendall, & Hesson, 1999; Odum, Jungkamp, Griffin, Flagan, & Seinfeld, 1997). SOA contributes a large fraction of urban PM mass (Jimenez & Canagaratna, 2009), and gasoline vehicles are an important source of SOA precursors in urban environments (Jathar, Woody, Pye, Baker, & Robinson, 2016). Therefore, changes in exhaust composition that increase SOA and ozone formation may have important health implications.

The EPA GHG program is aimed at reducing tailpipe CO_2 emissions. The increased fuel economy of GDI engines means lower CO_2 emissions per mile; however, higher black carbon (BC) emissions (the most potent absorptive agent of anthropogenic PM) (Bond et al., 2013; Ramanathan & Carmichael, 2008) could potentially offset any climate benefits of reduced CO_2 emissions. Zimmerman et al. (2016) analyzed published BC emissions rates and concluded that a few percent increase in the fleet-average fuel economy is enough to offset the potential effects of increased BC emissions from GDI vehicles. However, more emissions data, especially from newer (SULEV) GDI vehicles, are needed to better quantify the potential future climate impacts of this technology.

In this study, we present a comprehensive database of emissions from a fleet of GDI and PFI equipped light duty gasoline vehicles tested on a chassis dynamometer over the cold-start unified cycle (UC). Measurements include gas- and particle-phase emissions, particle number, particle size distributions, and speciated NMOG emissions. We use the data to quantify the effects of engine technology, emission standards, and cold-start on

emissions. We estimate ozone and SOA formation potential. Finally, we analyze the potential climate effects of switching a PFI to a GDI fleet.

4.2 Methods

4.2.1 Fleet Overview

This study reports tailpipe emission data from eighty-two light duty gasoline vehicles. Data from nineteen vehicles tested in 2014 are combined with previously published data for sixty-three vehicles previously reported in May et al. (2014). The same protocols were used in both test campaigns. Information for all vehicles are listed in Tables S1 and S2 in the SI.

The test fleet was not designed to represent the distribution of vehicles in the current, in-use fleet. Instead vehicles were selected to span a wide range of model years (1988-2014), vehicle types (passenger cars and light-duty trucks), engine technologies (GDI and PFI), emission certification standards (Tier1 to SULEV), and manufacturers. The 2014 test fleet consisted of thirteen distinct vehicles with GDI engine technology: eleven wall-guided GDIs and two spray-guided GDIs. It also included six distinct vehicles with PFI engine technology. The May et al. (2014) fleet was comprised of sixty-one PFI and two GDI vehicles. Vehicles were recruited using a quasi-random process from the Southern California in-use fleet; we recruited vehicles from private citizens, rental car agencies, or the Air Resources Board fleet. Each vehicle was tested on the cold-start unified cycle (UC).

For discussion, the vehicles are grouped based on engine technology (PFI or GDI) and emission certification standard. The emission certification groups included: U.S. Tier1, California low-emission vehicle (LEV), California ultra-low-emission vehicle (ULEV),

84

and California super-ultra-low-emission vehicle (SULEV). Table S3 lists the certification standards for each of these groups.

Table S4 lists the number of vehicles in each engine-technology/certification-standard group. Some standards do not require emission reductions of every pollutant. Specifically, the NO_x standard changed for LEV1 and LEV2 vehicles but the standards for other pollutants did not. Therefore, slightly different groupings are used for NO_x versus other pollutants. We separate LEV and ULEV vehicles into two categories for NO_x: LEV1 (LEV1 and ULEV) and LEV2 (LEV2 and L2ULV), but group these vehicles into LEV (LEV1 and LEV2) and ULEV (ULEV and L2ULV) categories for all other pollutants. The SULEV category also includes vehicles certified as partial-zero-emission vehicles (PZEV) which also meet the SULEV tailpipe emissions standard. All SULEV PFI vehicles tested in the 2014 campaign were equipped with a hybrid engine technology.

4.2.2 Fuel

All the vehicles were tested using commercial gasoline that met the summertime CA fuel standards. All the 2014 vehicles were tested using the same fuel – a 10% ethanol blend (E10), with a carbon mass fraction of 0.82. Additional composition data are in Table S5. The composition of the 2014 fuel and that of the previous campaigns are very similar (May et al., 2014).

4.2.3 Vehicle Tests and Emission Measurements

A detailed description of the experimental setup and procedure is provided in May et al. (2014). Vehicles were soaked overnight prior to testing and then operated over a cold-start UC using a chassis dynamometer at the ARB Haagen-Smit Laboratory. The UC

consists of three distinct phases: the cold-start (bag 1), hot-stabilized operations (bag 2), and hot-start (bag 3). Vehicles were soaked for ten minutes between bags 2 and 3. The UC has a similar three phase structure as the Federal Test Procedure (FTP), but is more aggressive in an attempt to better simulate driving conditions in California.

The entire vehicle exhaust was diluted using a constant volume sampler (CVS) system. The dilution air was filtered using high efficiency particulate air (HEPA) filters. Gas-phase emissions were sampled into heated Tedlar© bags from which samples were taken to quantify CO, CO_2, CH_4, NO_x, and total hydrocarbons (THC) emissions for each UC phase. THC was measured using Flame Ionization Detection (FID) calibrated daily with a methane/propane blend. The Tedlar© bag samples were also analyzed offline for speciated hydrocarbons by UC phase using standard gas-chromatography (California Air Resources Board, 2007). Carbonyls emissions for each UC phase were measured by collecting 1,4-dinitrophenylhydrazine (DNPH) impregnated cartridge samples (Sep-Pak DNPH-Silica Cartridges Plus-Long Body, Waters Corporation) that were analyzed with high-performance liquid chromatography (California Air Resources Board, 2006). Non-methane organic gas (NMOG) is defined as THC plus carbonyls minus CH_4.

Particle-phase emissions were collected using three filter trains operating in parallel. Train 1 contained a single Teflon filter (47 nm, Pall-Gelman, Teflo R2PJ047). Train 2 contained two quartz filters (47 nm, Pall-Gelman, Tissuquartz 2500 QAOUP) in series. Train 3 contained a Teflon filter followed by a quartz filter. Teflon filters were weighed pre- and post-test in a temperature and humidity controlled room to determine gravimetric PM mass emissions (California Air Resources Board, 2011c). Teflon filters in Train 1 were extracted and analyzed by ion chromatography for water soluble anions (chloride, nitrate and sulfate) and cations (sodium, ammonium, potassium, magnesium and calcium)

(California Air Resources Board, 2011b). All quartz filters were analyzed for organic and elemental carbon (OC and EC) using the IMPROVE A protocol (California Air Resources Board, 2011a). One set of filter was collected for each test over the entire UC, not by individual UC phase at a constant flow rate.

4.2.4 Real-Time Measurements

Real-time measurements were made during the 2014 campaign. A fast response Engine Exhaust Particle Sizer (EEPS, TSI Inc.) measured particle number distributions from 6.4 to 523 nm (Ayala & Herner, 2005). A Micro Soot Sensor (MSS, AVL, Austria) was used to measure real-time black carbon (BC) concentrations. The MSS is a photo-acoustic instrument with an 808 nm laser. Figure S1 in the SI shows excellent agreement between filter based EC mass concentrations and the cycle-integrated MSS BC mass concentrations (slope = 1.08, R^2 = 0.94). The nonrefractory submicron particle mass and chemical composition were measured using a high-resolution time-of-flight aerosol mass spectrometer (HR-tof-AMS, Aerodyne, Inc., MA). Figure S2 shows good agreement between filter-based organic mass and cycle-integrated HR-tof-AMS-measured organic mass (slope = 1.2, R^2 = 0.9).

4.2.5 Emission Factors

Gas- and particle-phase emissions are reported as distance-based emission factors (mass of pollutant X emitted per mile driven).

$$EF_x = \frac{(C_x^m - C_x^b).V}{UC\ distance} \tag{4.1}$$

Where $C_x^m - C_x^b$ is the background corrected pollutant mass concentration inside the CVS, V is the total volume of air that passed through the CVS, and UC distance is the

length of the unified cycle (11 miles). We also report the measured fuel economy for each test so that the distance-based emission factors can be converted to fuel-based ones (Table S7).

Emission factors for gas-phase pollutants are corrected for background concentrations measured in the dilution air upstream of the mixing section of the CVS during each test. Background filter-based PM and EC mass concentrations were measured during separate dynamic blank experiments (CVS operated only on dilution air i.e., no exhaust); they were below method detection limits (e.g. 2 µg-C/sample for EC).

Unlike all other pollutants, dynamic blanks (but not handling blanks) for filter-based OC were comparable in magnitude to the OC concentration measured during tests of lower emitting vehicles. For example, the OC dynamic blanks correspond to 28% and 98% of OC mass concentrations collected on the bare quartz filters for Tier1 and SULEV certified PFI vehicles respectively. However, OC emission factors were not background corrected because the dynamic blank OC concentrations overestimate the OC that actually desorb from the CVS walls during an actual test due to differences in dilution conditions. During a dynamic blank, the CVS is operated on clean air with no emissions, which maximizes the evaporation of organics from the CVS walls. This causes the dynamic blank OC to exceed that collected on filters during tests of the lowest emitting vehicles due to organics desorbing from the CVS walls (May et al., 2014). For example, the average ± 1 standard deviation of OC dynamic blank was 15.4 ± 1.9 µg-C/sample, which corresponds to an emission factor of ~0.2 mg-C/mi; the lowest OC mass collected during an actual test was 11.4 µg-C/sample. Given this uncertainty, we did not correct the OC data for dynamic blanks, similar to other studies (Fujita et al., 2007; May et al., 2014). In addition, we

achieved good mass closure between the gravimetric mass and the sum of PM species with the non-dynamic blank corrected OC data (Figure S4).

4.2.6 Measurement Uncertainty and Statistical Significance

To characterize experimental uncertainty, we tested a subset of the vehicles multiple times using identical procedures. Table S6 lists the median test-to-test variability of the same vehicle expressed as a relative standard deviation (%RSD) for gas-phase (THC, CO, and NOx) and particle-phase (PM, EC, OC) pollutants. The median test-to-test variability of the same vehicle for gas-phase pollutants was 25% (90th percentile 57%); the median variability for particle-phase pollutants was 10% (90th percentile 40%) (Table S6 and Figure S3). When considered on a relative basis, emissions are somewhat more variable for newer (lower emitting) vehicles than older vehicles. However, on an absolute basis, the emissions from newer vehicles are less variable than older vehicles. Test-to-test variability of the same vehicle is an overestimate of actual measurement uncertainty because test-to-test differences in vehicle performance will also contribute to test-to-test variability, in addition to experimental uncertainty.

We report the mean or median emissions of each vehicle group $\pm$ standard error ($SE = \sigma/\sqrt{N}$, N and σ represent the number of vehicles and standard deviation of the group, respectively). The number of vehicles included in the average for each group varies by pollutant because not every pollutant was measured successfully for every test (e.g. speciated NMOG data are only available for 75% of the tests). To test for statistically significant differences between groups, we performed a Wilcoxon non-parametric rank-sum test which is suitable for small datasets. If the p-value was smaller than 0.05, the difference in median between two sets was considered statistically significant. Tests of

statistical significance were only performed when there were at least five vehicles in each group.

4.3 Results and Discussion

4.3.1 Gas- and Particle-Phase Emissions

Emissions of THC, CO, and NO_x (as NO_2) are plotted in Figure 4.1 (data are given in Table S7). The distribution of emissions for each vehicle class are shown using box-whisker plots. For vehicles tested multiple times, we report the average emissions over all tests, to isolate vehicle-to-vehicle differences.

Figure 4.1 indicates significant vehicle-to-vehicle variability in emissions within each class, with the data exhibiting RSD ranging from 100% to 300%. This vehicle-to-vehicle variability is much larger than differences measured in repeat tests with the same vehicle (section 4.3.5). The large vehicle-to-vehicle variability is expected; it reflects the effects of different engine calibration, emission control technologies, and vehicle age and maintenance history. There is similar vehicle-to-vehicle variability for GDI and PFI vehicles. Fortunately, for most pollutants, our fleet is large enough to draw statistically significant conclusions about differences in emissions between different classes of vehicles.
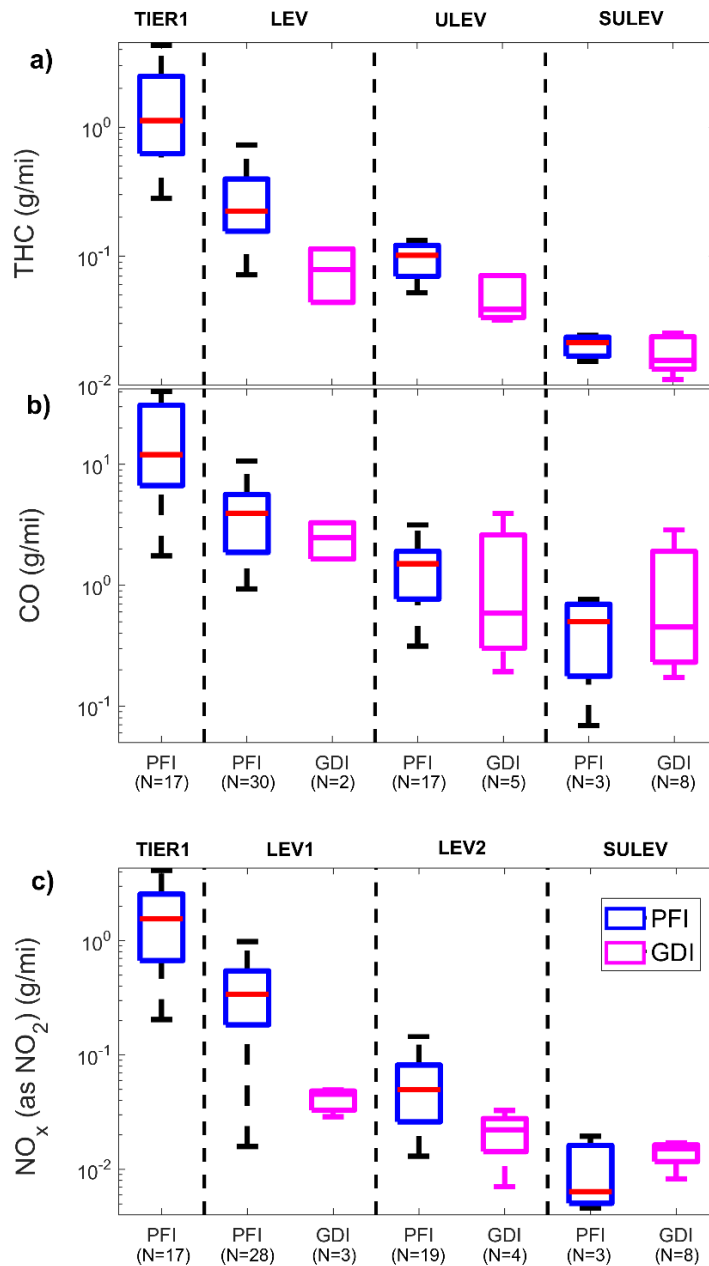
Figure 4.1 Emission factors for (a) THC, (b) CO, and (c) NOₓ (as NO₂) for different vehicle classes described in the text. The data are shown as box and whiskers to illustrate vehicle-to-vehicle variability in emissions for each class (the box represents the 25th to 75th percentiles, the horizontal line indicates the median, and the whiskers cover 99.3% of the data), with the exception of the LEV GDI category (N=2) for which the box shows the full range of emissions. Dashed vertical lines separate vehicles by emission standards.

As expected, Figure 4.1 shows lower tailpipe emissions of regulated pollutants (THC, CO, and NOₓ) from vehicles that meet more stringent emissions standards. These

91

differences are statistically significant for our fleet. Although Tier1 and LEV vehicles are certified to the same CO emissions standard (Table S3), these two categories were separated in Figure 4.1b to illustrate the advances in both engine and catalyst technology. The median distance-based CO emission factors for LEV PFIs (N=30) is a factor of three lower than for Tier 1 PFIs (N=17) – 5.3 ± 1.0 g/mi versus 12.0 ± 3.2 g/mi with a $p = 0.0003$. The large decrease in NO_x emissions between LEV1 to LEV2 vehicles, shown in Figure 4.1c, mirrors the sharp reduction in the NO_x emission standard (Table S3). We found no statistically significant differences in gas-phase emissions between ULEV GDIs (N=5) and ULEV PFIs (N=17).

Figure 4.2a shows PM emission factors for all vehicle categories with underlying data listed in Table S7. The gravimetric PM mass emissions are shown using box-whisker plots to illustrate the vehicle-to-vehicle variability for each vehicle class; also shown are the median EC and primary organic aerosol (POA) emission factors. POA is defined as quartz filter OC multiplied by 1.2 organic-matter-to-organic-carbon ratio, which is representative of fresh vehicle emissions (Turpin & Lim, 2001). Other studies have used slightly higher conversion factors: Cheung et al. (2009) assumed 1.4 and Short et al. (2016) used 1.5. Box-whiskers plots for EC and OC emissions factors are shown in Figure S4.

For vehicles certified as LEV2 or to a stricter standard, we measured higher PM mass emissions from GDI vehicles (4.2 ± 1.0 mg/mi, N=15) compared to PFI vehicles (2.6 ± 0.5 mg/mi, N=30). This difference is statistically significant (p=0.05). Similarly, median PM mass emissions from ULEV GDI vehicles (6.3 ± 1.1 mg/mi, N=5) are about a factor of 2 higher than ULEV PFI vehicles (3.8 ± 0.7 mg/mi, N=17). The median PM mass emission from ULEV GDIs are only 40% lower than the median PM mass fuel-based emission factors from 25+ year old Tier1 PFIs compared to a 70% reduction for ULEV PFIs. SULEV

GDIs have lower PM mass emissions (3.0 ± 1.1 mg/mi, N=8) compared to ULEV GDIs (6.3 ± 1.1 mg/mi, N=5) indicating reduced PM mass emissions from newer GDI engine technology. We measured even lower PM mass emission factors from the two spray-guided SULEV GDIs: 2.3 and 0.71 mg/mi respectively.
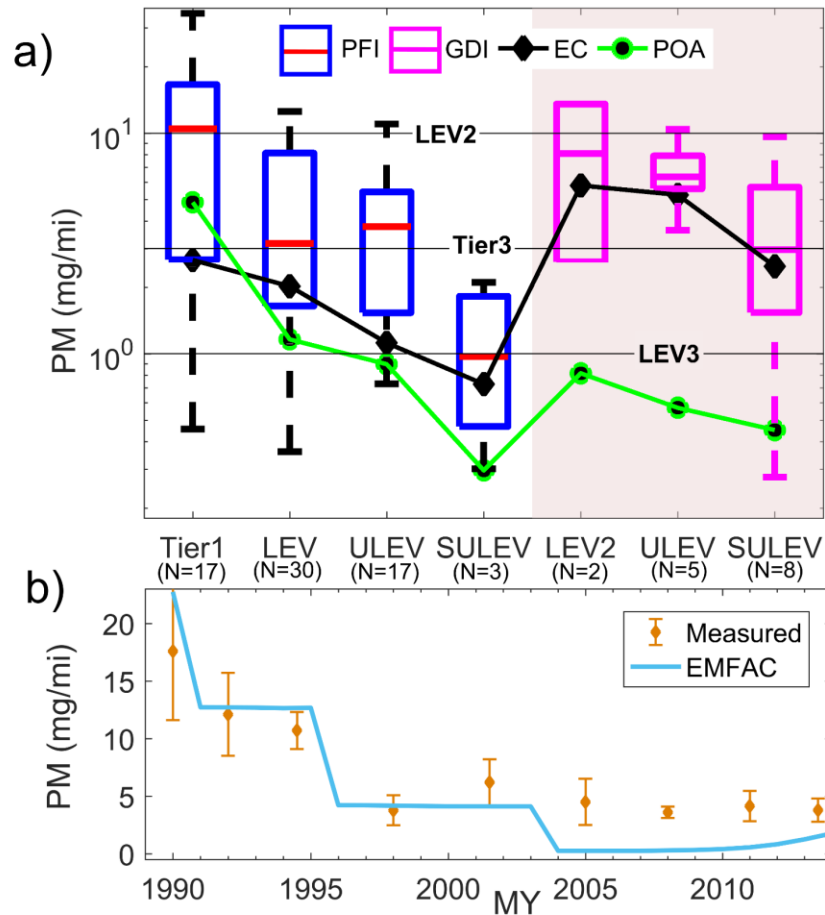
Figure 4.2 Panel (a) shows measured PM mass (shown in box whiskers), median EC (black diamond data points) and median POA (green circle data points) emission factors (mg/mi) for different vehicle classes. Horizontal lines in panel (a) indicate PM emission standards: current LEV2 regulation of 10 mg/mi; Tier3 and LEV3 regulations of 3 mg/mi; and LEV3 regulations of 1 mg/mi (starting 2025). Boxes represent the 25th to 75th percentiles, the horizontal line indicates the median, and the whiskers cover 99.3% of the data. Panel b shows measured (data points) and EMFAC2014-predicted (solid line) PM mass emission factors of fleet-average gasoline vehicle emissions by model year (MY). Error bars correspond to the standard error in the measurements.

Except for some older (Tier1) vehicles, PM mass emission factors are lower than the current standard of 10 mg/mi, even though they were tested on the more aggressive UC cycle. However, new Federal (Tier3) and California (LEV3) standards limit PM mass emissions to 3 mg/mi starting in 2017; the LEV3 regulation enforces an even tighter PM standard of 1 mg/mi starting in 2025. Unlike SULEV GDIs, all SULEV PFIs tested appear to meet both the Tier3 and LEV3 standard, assuming PM mass emissions from the UC are higher than from the FTP (Robert, VanBergen, Kleeman, & Jakober, 2007). Our data suggest that some additional reductions in PM mass emissions from GDIs will likely be needed to meet the stricter LEV3 standard in 2025.

Our differences in PM mass emissions between PFIs and GDIs are much smaller than the order of magnitude difference reported by Karavalakis et al. (2015). Karavalakis et al. (2015) tested one PFI that had very low PM mass emissions (~0.2 mg/mi) compared to our PFI fleet, which had PM mass emissions of 3.8 ± 0.7 mg/mi (N=17) and 1.0 ± 0.5 mg/mi (N=3) for ULEV and SULEV PFIs respectively.

Figure 4.2b compares measured PM mass emissions to predictions from EMFAC2014 (the ARB mobile source emissions inventory (California Air Resources Board, 2014)) for a fleet-average gasoline vehicle by model year (MY) for the California South Coast Air Basin. Model inputs and data are provided in Table S8. To estimate PM mass emissions of a fleet-average vehicle from our data, we averaged our data into MY bins (with several MYs in the same bin). We separately averaged PFI and GDI data, which were then weighted by the market share used by EMFAC.

For MY 2003 and older vehicles, there is good agreement between our data and EMFAC predictions. However, for MY 2004 and newer vehicles, EMFAC predicts dramatically lower running exhaust PM mass emissions (0.2 mg/mi in MY 2004 versus 3.2

mg/mi in MY 2003). This is due to predicted reductions in PFI PM mass emissions. Our fleet shows no evidence for such a large decrease in PM mass emissions for MY 2004 and newer PFIs. Our fleet is diverse and is comprised of a reasonable number of vehicles (27 PFIs are MY 2004 and newer), but it may not be representative of the California in-use fleet.

EMFAC predicts increased PM emissions of a fleet-average gasoline vehicle starting in MY 2007 due to the increasing market share of GDI vehicles. EMFAC assumes that GDIs have a PM mass emission of 4.0 mg/mi, which is consistent with our data (Figure 4.2a). Therefore, the differences between measured and predicted emissions in Figure 4.2b for MY 2004 and newer vehicles is due to differences in PFI not GDI emissions.

The comparison in Figure 4.2b suggests that EMFAC may underestimate the PM mass emissions for MY 2004-2014 gasoline vehicles. We quantified this discrepancy by multiplying the difference between measured PM and EMFAC-predicted PM (mg/mi) by the vehicle miles travelled in 2014 (VMT mi/yr) for each MY vehicle, and then summing over all MY between 2004 – 2014. It corresponds to 0.15 Gg in 2014, which is four times larger than the EMFAC predictions for all MY 2004-2014 gasoline-vehicles.

4.3.2 PM Composition

Figures 4.2a, S4, and S5 present PM composition data. Figure S5 indicates that the PM mass emissions are dominated by carbonaceous components (EC and POA). The fractional contribution of EC to the PM mass increases from about 0.4 for Tier1 PFIs to almost 0.8 for GDIs. There was good mass closure between gravimetric PM and speciated PM, with 61% of the data tests having a ratio of speciated PM to gravimetric PM between 0.8 and 1.2 (Figure S4).

Figure 4.2a shows that changes in PM mass emissions between PFIs and GDIs are driven by differences in EC emissions. For example, for vehicles certified as ULEV, we measured a 5-fold increase in median EC emission for GDIs (5.3 ± 0.8 mg/mi, N=5) compared to PFIs (1.1 ± 0.6 mg/mi, N=17) with a p=0.02. This increase is similar to a previous study (Zimmerman et al., 2016). For vehicles certified as SULEV, we measured a threefold increase in median EC mass emission (2.5 ± 0.8 mg/mi, N=8 for GDIs versus 0.8 ± 0.3 mg/mi, N=3 for PFIs). This is smaller than the 3- to 17-fold increase in BC emissions from two PZEV GDI vehicles compared to a single PFI reported in Bahreini et al. (2015). The PFI used in Bahreini et al. (2015) had lower EC emissions compared to our median ULEV PFI.

In contrast to EC, all newer vehicles (both GDI and PFI) have lower POA emissions. However, for vehicles certified as LEV2 or to a stricter standard, the average POA mass emissions of PFIs ((10.8 ± 1.3) x 10^{-1} mg/mi, N=30) is about a factor of two higher than GDIs ((5.4± 0.5) x 10^{-1} mg/mi, N=15) with a p=0.004. The steady decrease in POA mass emissions means that EC dominates PM emissions from vehicles certified to stricter emissions standards (Figure S5). The POA-to-EC ratio of GDI emissions is similar to diesel engines not equipped with diesel particulate filters (Bond et al., 2013; May et al., 2014). Therefore widespread adoption of GDIs will dramatically reduce the utility of EC as a marker for diesel exhaust in urban environments (Bond et al., 2013; NIOSH 1996).

The composition of primary organic aerosols (POA) emitted from the vehicle tailpipe was characterized using FTIR analysis of samples collected on Teflon filters (Liu et al., 2012; Russell et al., 2009). FTIR data indicate that POA composition does not vary between vehicle groups (Figure S6).

We calculated the POA-to-NMOG ratio to quantify the relative importance of gaseous versus semivolatile organics. The majority of the POA collected with a quartz filter is semivolatile organics, particle-phase organics plus some organic vapors adsorbed to the filter (May et al., 2014). The median POA-to-NMOG ratio for all vehicles is $(10.4 \pm 0.3) \times 10^{-3}$, indicating emissions of gas-phase organics dominate semivolatile organics. However, for vehicles certified to LEV2 or to a more stringent standard, the average POA-to-NMOG ratio is higher for GDIs ($(21.8 \pm 1.2) \times 10^{-3}$, N=12) compared to PFI vehicles ($(11.0 \pm 0.2) \times 10^{-3}$, N=23). The difference is statistically significant (p=0.03); it is more pronounced after correcting for dynamic blank OC concentrations measured (Figure S7).

4.3.3 Particle Number Emissions and Size Distributions

Particle number and size distributions were measured using an EEPS during the 2014 campaign. Figure 4.3 shows average measured size distributions from four GDIs (two ULEVs and two SULEVs) and five PFIs (two SULEVs, both hybrids, and a single ULEV, LEV and Tier1). The EEPS has a lower cutoff of 6.4 nm; therefore, the total number emissions reported here are particles greater than that size.
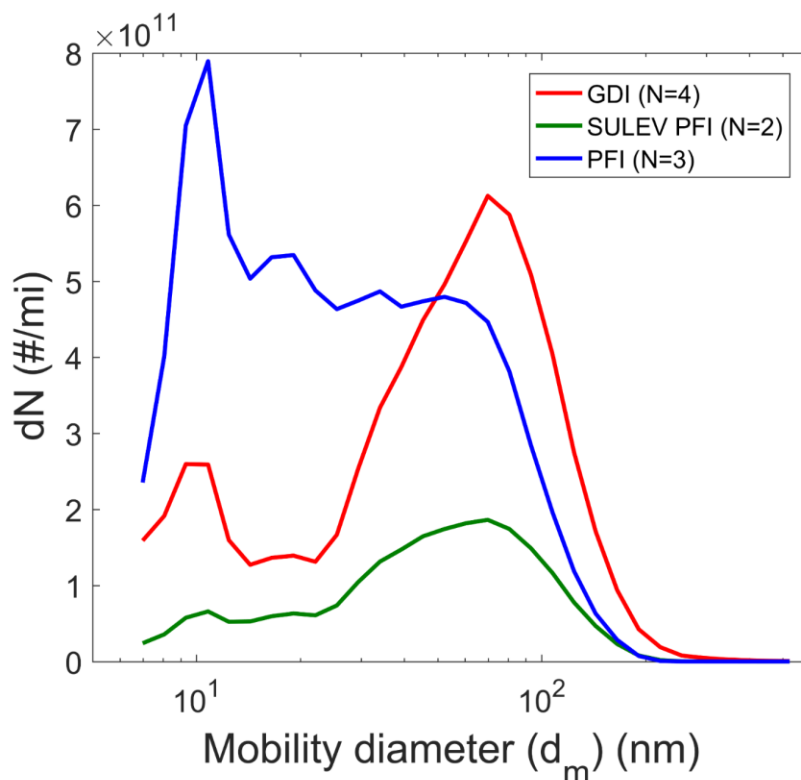
Figure 4.3 Average particle number emissions as a function of size measured over the entire UC cycle of four GDI vehicles (two ULEVs and two SULEVs; red line), three PFI vehicles (one ULEV, LEV and Tier1; blue line) and two SULEV hybrid PFI vehicles (green line).

Particle number emissions exhibited significant vehicle-to-vehicle variability. For our fleet, the GDIs had modestly higher average total particle number emissions than PFIs; $(7.1 \pm 2.6) \times 10^{12}$ #/mi versus $(6.7 \pm 2.5) \times 10^{12}$ particles/mi. The spray-guided SULEV GDI had a total number emission factor of 5.3×10^{10} particles/mi, much lower than the wall-guided GDIs (and comparable to a SULEV PFI). Our difference between PFI and GDI particle number emissions is comparable to results from Zhang and McMahon (2012). Our particle number emission factors for GDIs agree with those reported by Karavalakis et al. (2015), but our PFIs had higher particle number emissions compared to the PFIs tested by Karavalakis et al. (2015).

Figure S8 shows that gravimetric PM mass varies linearly with particle mobility-based volume, regardless of engine technology. The slope of the linear regression indicates an average effective particle density of 1.6 g/cm^3 (R^2 = 0.95, Figure S8). This value is close to the black carbon material density of 1.8 g/cm^3 (Bond et al., 2013), suggesting that black carbon particles emitted have a compacted morphology.

Figure 4.3 shows size distributions averaged over the entire UC for GDIs and two different groups of PFIs (SULEV certified and all other PFIs). Although our GDIs and PFIs had similar total number emissions, there are important differences in the PM size distributions, which must be accounted for when comparing total number emissions. For most vehicles, the measured number distribution was bimodal with a nucleation mode at ~10 nm and a soot mode at ~60-90 nm, consistent with previous studies (Karjalainen et al., 2014; Peckham, Finch, Campbell, Price, & Davies, 2011; Zhang & McMahon, 2012; Zimmerman et al., 2016).

Figure 4.3 indicates that GDI emissions are characterized by: (1) a soot mode mobility diameter that is shifted to larger sizes compared to that of older PFI emissions (mode mobility diameter of ~70 nm for GDIs versus ~50 nm for older PFIs; SULEV PFIs had a mode soot diameter of ~70 nm), and (2) higher particle number in the soot mode; average of (5.5 ± 1.8) x 10^{12} particles/mi for GDIs versus an average of (1.8 ± 1.7) x 10^{12} particles/mi for SULEV PFIs. Both factors contribute to higher PM mass emissions from GDIs compared to PFIs.

The non-SULEV PFIs had three times higher particle number emissions in the nucleation mode (particles with mobility diameter smaller than 20 nm) compared to GDIs. This is likely related to the differences in particle surface area. GDIs emit much more EC (and therefore particle surface area) than PFIs. EC is a sink for condensable vapors,

suppressing nucleation (Kerminen & Wexler, 1995). In comparison, SULEV PFIs have a nucleation mode that is significantly suppressed compared to other non-SULEV PFIs (an order of magnitude decrease in particle number). A challenge is that nucleation is very sensitive to dilution conditions (Abdul-Khalek, Kittelson, Brear, & Kittleson, 1999), making it difficult to extrapolate number emissions data measured in a CVS to the real world. Differences in sampling conditions also likely contribute to the differences in number emissions between vehicles and studies.

4.3.4 NMOG Speciation

The NMOG emissions from gasoline vehicles are comprised of very complex mixture of individual species. The impact of these emissions on ozone and secondary organic aerosol formation (SOA) depends on NMOG speciation. Individual NMOGs, such as benzene and formaldehyde, are also air toxics. Although many studies have reported detailed NMOG composition data for gasoline vehicle emissions (Drozd et al., 2016; May et al., 2014), relatively few compare data from PFIs and GDIs (Cole et al., 1998; Karavalakis et al., 2015; Zimmerman et al., 2016). Comprehensive NMOG speciation data is listed in Table S9.

Figure S10 groups the total organic gas composition data into three major categories: (1) methane (0.13 ± 0.05, mass fraction of total organic gas); (2) other speciated NMOG (206 compounds, 0.54 ± 0.08) and (3) unspeciated NMOG (0.33 ± 0.09), defined as the NMOG minus the sum of the speciated compounds. The contribution of these broad categories is consistent across the different vehicle groups.

Figure 4.4 shows the average composition of the speciated NMOG for each vehicle class. The speciation data are grouped into the following categories: C2-C6 straight and

branched paraffins, C7-C12+ straight and branched paraffins, olefins and naphthenes, cyclic olefins, polycyclic naphthenes, alkynes, single-ring aromatics, polycyclic aromatics, and oxygenated. The vehicle-to-vehicle variability in NMOG speciation is shown in Figures S11 and S12.
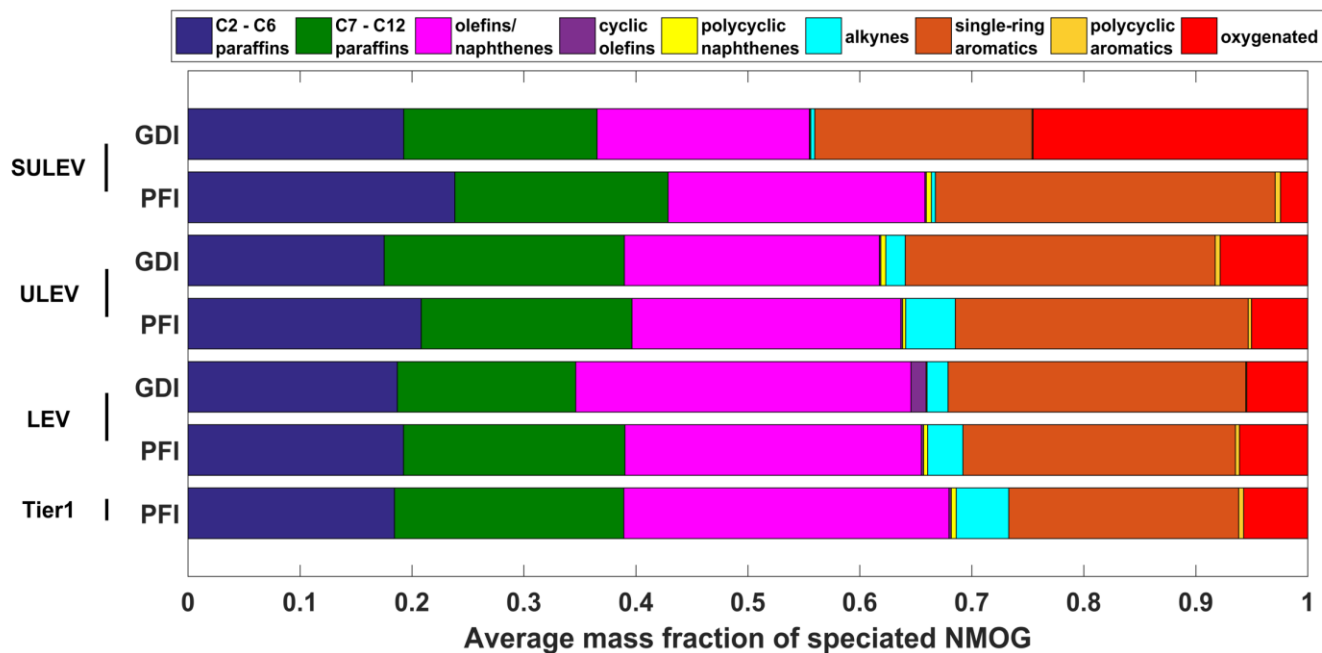
Figure 4.4 Major compound categories of NMOG emissions for different vehicle categories described in the text.

There were no statistically significant differences in NMOG composition between vehicle classes regardless of engine technology, except for relatively higher contributions of oxygenated compounds from SULEV GDIs compared to other vehicle categories. Oxygenated compounds contributed ~25% of the speciated NMOG emissions from SULEV GDIs versus ~5% for other vehicle categories. This shift was offset by lower contributions from olefins and naphthenes and single-ring aromatics.

Several non-aromatic carbonyls (formaldehyde, acetaldehyde, and acrolein) and single-ring aromatics are classified as priority mobile source air toxics (MSATs) (Federal

Highway Administartion, 2016). Emission factors for benzene, toluene, ethylbenzene, and xylenes (BTEX) are shown in Figure S13. BTEX emissions mirror THC emissions (Figure 4.1) with lower emissions from vehicles meeting more stringent emissions. There are negligible ethylbenzene emissions from newer vehicles. Zimmerman et al. (2016) reports elevated emissions of BTEX based on tests of seven Ford Focus GDI vehicles compared to the Toronto fleet. We found no statistically significant difference in BTEX compounds emission factors between GDIs and PFIs for our larger GDI vehicle fleet.

Acetaldehyde and formaldehyde dominate the emissions of oxygenated compounds. SULEV GDIs have 2 times higher formaldehyde emissions compared to ULEV GDIs; 2.1 ± 1.3 mg/mi for SULEV GDIs (N=6) versus 1.2 ± 0.4 mg/mi for ULEV GDIs (N=4). However, the high formaldehyde emissions from the SULEV GDIs are due to a single vehicle.

To quantify the effects of switching engine technologies (GDI vs. PFI) on ozone and SOA production, we calculate both the ozone and SOA formation potentials using NMOG composition data. Ozone formation potential (g-O_3/g-NMOG) is an estimate of the maximum amount of ozone formed per mass of reacted NMOG. We calculated this potential using maximum incremental reactivity (MIR) values (http://www.oal.ca.gov/CCR.htm (Carter, 1994)). For vehicles certified as LEV2 or to a more stringent standard, NMOG emissions from PFI (N=13) and GDI (N=23) vehicles have essentially the same ozone formation potential 3.0 ± 0.3 versus 2.8 ± 0.3 g-O_3/g-NMOG respectively (p=0.7).

We calculated the SOA formation potential using the high NO_x mass-yield data in CMAQv4.7 (Carlton et al., 2010) for speciated NMOG and the mass-yield data from Jathar et al. (2014) for unspeciated NMOG. The calculations assume an organic aerosol

concentration of 5 µg/m^3. Both technologies have essentially the same SOA formation potential with a median SOA mass-yield (mg-SOA/mg-NMOG) of 6.5 ± 0.7% and 6.9 ± 0.7% (p=0.8) for all PFI (N=17) and GDI (N=12) vehicles certified as LEV2 or to a stricter standard.

4.3.5 Cold-Start versus Hot-Stabilized Emissions

Cold-start contributes disproportionally to vehicle emissions, because the catalytic converter has not reached its operating temperature (Drozd et al., 2016; George et al., 2015; Weilenmann, Soltic, & Hausberger, 2013). We quantify the importance of cold-start using the ratio (γ),

$$\gamma = \frac{m_x^{bag1}}{EF_x^{bag2}} \tag{4.2}$$

where m_x^{bag1} is the total mass of emissions of pollutant x in UC bag 1 (cold start) and EF_x^{bag2} is the distance-based emissions factors of pollutant x in UC bag 2 (hot-stabilized operations). Therefore, γ represents the number of miles of hot-stabilized driving required to match cold-start (bag 1) emissions from the UC cycle. UC bag 1 corresponds to the first 300 seconds of the test cycle (1.2 miles of driving); UC bag 2 is 1135 seconds long (8.6 miles of driving). Therefore, γ also approximately indicates the ratio of bag 1 to bag 2 emission factors (it is 20% higher).
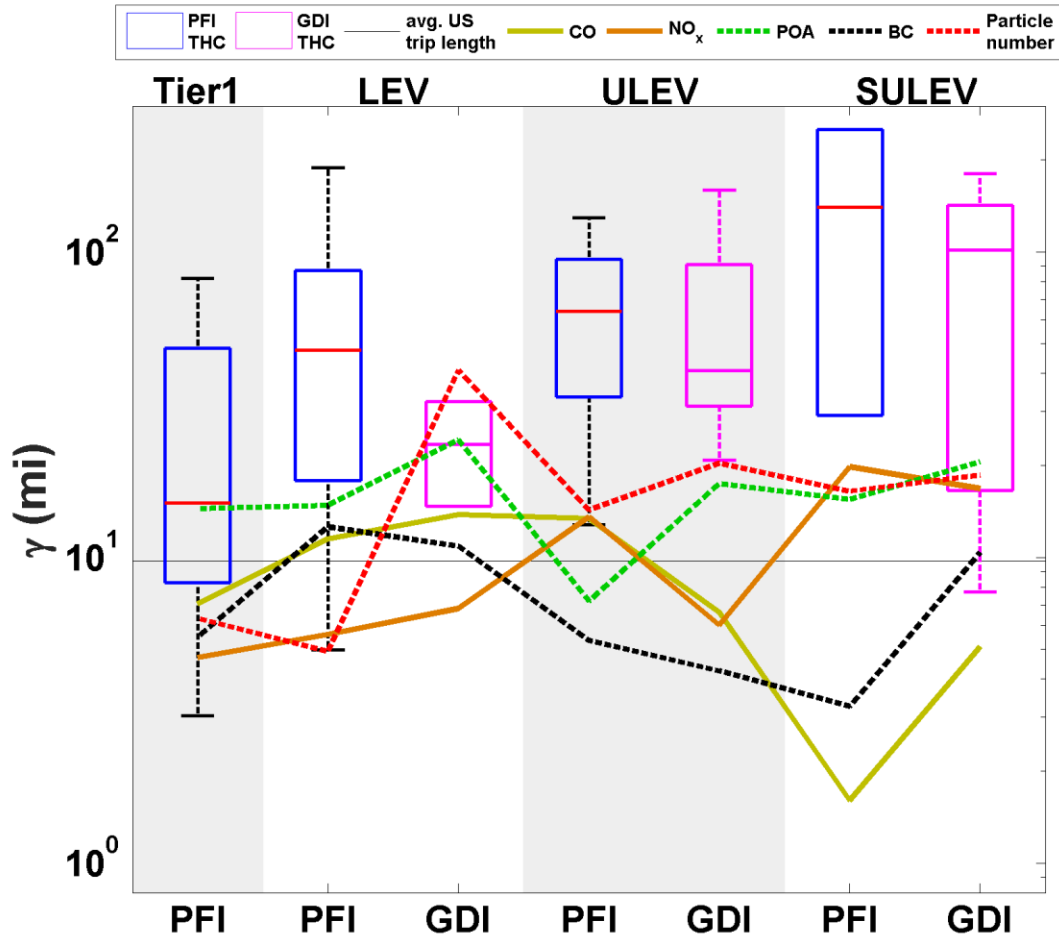
Figure 4.5 Relative importance of cold-start emissions expressed as γ (number of miles of hot-stabilized operations (UC bag 2) to equal cold-start (UC bag 1) emissions) for different vehicle classes. Values of γ for THC are shown as box whiskers to illustrate vehicle-to-vehicle variability in emissions. The box represents the 25th to 75th percentiles, the horizontal red line indicates the median, and the whiskers cover 99.3% of the data. Solid lines connect median γ values for CO and NOx. Dashed lines connect median γ values for POA, BC, and particle number. For reference the U.S average trip length is 9.7 miles, and is shown as the horizontal solid line. Vehicles are grouped based on emission certification standard and engine technology, as described in the text. The alternating shaded regions indicate different certification standards.

Figure 4.5 plots γ values for select gas- and particle-phase pollutants: THC, CO, NOx, POA, BC, and particle number. The THC γ are shown using a box-whisker plot to illustrate vehicle-to-vehicle variability. For the other pollutants, only median γ values for each vehicle category are shown to reduce clutter. Box-whisker plots of γ values for the other

pollutants are shown in Figure S14. As a reference, the daily average trip length in the US is 9.7 miles (FHA, 2011).

Figure 4.5 shows that the importance of cold-start varies by pollutant and emission certification standard, but not engine technology. Cold-start is more important for THC emissions than for other pollutants. Across the fleet, median THC γ is 41.3 mi versus 8.4 mi and 5.9 mi for CO and NO_x respectively. The median THC γ is four times the daily average trip length of 9.7 miles in the US. Therefore, within the limit of the UC cycle representing US driving patterns, cold start dominates the THC emissions for the majority of the fleet. However, the median γ for CO and NO_x is less than the daily average trip length in the US. Therefore, both cold-start and hot stabilized operations likely make significant contributions to real-world emissions for these pollutants.

Cold-start THC emissions are most important for newer vehicles; for example, the median THC γ is 101.5 ± 34.6 mi for SULEV (N=7) versus 15.4 ± 8.4 mi for 25+ year-old Tier 1 vehicles (N=17), p=0.03. This suggests that only a few percent of the fleet will have significant hot-stabilized emissions compared to cold-start emissions as SULEV vehicles dominate the fleet over the next decade. This underscores the importance of continued focus at reducing cold-start THC emissions. Although THC γ is higher for newer vehicles, it is a relative measure of the importance of UC bag 1 versus UC bag 2 emissions. On an absolute basis, the SULEV THC bag 1 emissions are dramatically lower than those from older vehicles, mirroring the trends shown in Figure 4.1.

CO γ decreases for newer vehicles; for example, median CO $\gamma = 14.3 \pm 2.8$ mi for ULEV vehicles (N=21) versus 4.5 ± 1.1 mi for SULEV vehicles (N=11). The difference is statistically significant (p=0.004). Unlike THC and CO, there is no clear trend in γ with

emission certification standard for NO_x; average NO_x γ 17.7 ± 4.2 mi for all vehicles (N=82).

Figure 4.5 also shows γ values for particle phase emissions: POA (measured with the HR-tof-AMS), BC (measured with MSS, comparable to EC, Figure S1) and particle number (measured with EEPS). Cold-start is more important for POA than BC; for our fleet, the average POA γ is 17.7 ± 2.1 mi (N=18) versus BC γ of 10.3 ± 2.0 mi (N=24). This is presumably due to the catalyst removing some of the POA during hot-stabilized operations (bag 2). However, POA γ values are much lower than THC γ, which indicates that POA is less sensitive to catalyst warm up than more volatile organics. Unlike THC, there is little dependence of POA γ on emission standard. Median particle number γ mirror POA γ.

Figure S14 shows the effects of cold-start on major SOA precursors (sum of single-ring aromatics and unspeciated NMOG), BTEX, and air toxics (formaldehyde and acetaldehyde). The γ values of these species largely mirror THC γ (for example, showing increased importance of cold-start emissions from newer vehicles). However, this is not true for all organics. For example, primary fuel compounds in the C7-C12+ paraffin category and single ring aromatic compounds other than BTEX were undetectable emissions during the hot-stabilized phase (undefined γ). Cold-start emissions of formaldehyde are less important for newer vehicles, with a median γ of 22 mi for LEV vehicles versus γ of 4 mi for SULEV GDI vehicles.

4.3.6 Potential Climate Impacts

Higher fuel efficiency is a major motivation for the widespread adoption of GDI vehicles. For our fleet, the GDIs had on average 57 g/mi (10 g/mi – 104 g/mi; 95%

confidence interval, Figure S15) lower CO_2 emissions than PFIs when driven over the UC. This corresponds to a 14.5% (2% – 31%; 95% confidence interval) increase in fuel economy. This suggests a potentially important climate benefit, if the UC is representative of real-world driving. However, GDIs have higher BC emissions. BC is the most potent light-absorbing component of PM (Bond et al., 2013) and can have significant warming impact on the overall energy balance of the earth (Jacobson, 2001; Ramanathan & Carmichael, 2008). Therefore, the net climate benefit depends on both the increases in fuel efficiency and BC emissions.

We examined the potential climate implications of the tradeoff between increased BC emissions from GDIs potentially offsetting the lower CO_2 emissions compared to PFIs. Using emission factors for BC and CO_2 from all PFIs and GDIs, we compared the net atmospheric CO_2 addition or removal from replacing a PFI by a GDI, by converting BC emissions to equivalent CO_2 ($CO_{2\text{-e}}$).

$$\text{net } CO_2 = \Delta BC * 3200 \frac{gCO_{2-e}}{gBC} - \Delta CO_2 \tag{4.3}$$

Where ΔBC indicates the measured increase in BC emissions and ΔCO_2 indicates the measured decrease in CO_2 distance-based emission factor. BC emissions are converted to a CO_2 equivalent basis using a twenty year BC global warming potential of 3200 $gCO_{2\text{-e}}/gBC$ (Bond et al., 2013).

We evaluated Equation (4.3) by randomly sampling emissions data from our fleet of GDIs and PFIs 100,000 times using a Monte Carlo simulation. For our fleet, increases in the fuel economy of 1.6% (0.5% – 2.4%; 95% confidence interval) are sufficient to offset warming due to increased BC emissions from GDIs. This is much lower than the measured 14.5% increase in fuel economy between PFIs and GDIs. Therefore, our data suggests there will be a net climate benefit associated with switching from PFIs to GDIs, similar to

previous results (Zimmerman, Wang, Jeong, Wallace, et al., 2016). However, the increased BC emissions from GDIs reduces their potential climate benefits by 10-20%. This reduction is likely larger in the real-world because our increase in fuel economy (14.5%) between GDIs and PFIs is larger than that reported on-road measurements (National Research Council, 2011).

4.4 References

Abdul-Khalek, I., Kittelson, D., Brear, F., Kittleson, D. (1999). The Influence of Dilution Conditions on Diesel Exhaust Particle Size Distribution Measurments, *1999-01–11*, 1142–1999. https://doi.org/10.4271/1999-01-1142

Ayala, A., Herner, J. D. (2005). Transient Ultrafine Particle Emission Measurements with a New Fast Particle Aerosol Sizer for a Trap Equipped Diesel Truck. *SAE Technical Paper*, *2005-01–38*(724). https://doi.org/10.4271/2005-01-3800

Bahreini, R., Xue, J., Johnson, K., Durbin, T., Quiros, D., Hu, S., Huai, T., Ayala, A., Jung, H. (2015). Characterizing Emissions and Optical Properties of Particulate Matter from PFI and GDI Light-Duty Gasoline Vehicles. *Journal of Aerosol Science*, *90*, 144–153. https://doi.org/10.1016/j.jaerosci.2015.08.011

Bond, T. C., Doherty, S. J., Fahey, D. W., Forster, P. M., Berntsen, T., DeAngelo, B. J., Flanner, M. G., Ghan, S., Kärcher, B., Koch, D., et al. (2013). Bounding the Role of Black Carbon in the Climate System: A Scientific Assessment. *Journal of Geophysical Research: Atmospheres*, *118*(11), 5380–5552. https://doi.org/10.1002/jgrd.50171

Borbon, A., Gilman, J. B., Kuster, W. C., Grand, N., Chevaillier, S., Colomb, A., … De Gouw, J. A. (2013). Emission Ratios of Anthropogenic Volatile Organic Compounds in Northern Mid-Latitude Megacities: Observations Versus Emission Inventories in Los Angeles and Paris. *Journal of Geophysical Research Atmospheres*, *118*(4), 2041–2057. https://doi.org/10.1002/jgrd.50059

Braisher, M., Stone, R., & Price, P. (2010). Particle Number Emissions from a Range of European Vehicles. *Society of Automotive Engineers*, (Ci). https://doi.org/10.4271/2010-01-0786

California Air Resources Board. (2006). *SOP No. 104: Standard Operating Procedure for the*

Determination of Aldehyde and Ketone Compounds in Automotive Source Samples by High Performance Liquid Chromatography. Retrieved from http://www.arb.ca.gov/testmeth/slb/sop104v3.pdf (accessed on: 04/20/2017).

California Air Resources Board. (2007). *SOP No. MLD102/103: Procedure for the Determination of C2 to C12 Hydrocarbons in Automotive Exhaust Samples by Gas Chromatography*. Retrieved from https://www.arb.ca.gov/testmeth/slb/sop102-103v2-2.pdf (accessed on: 04/20/2017).

California Air Resources Board. (2011a). *SOP No. MLD139: Procedure for Organic Carbon and Elemental Carbon (OC/EC) Analysis of Vehicular Exhaust Particulate Matter (PM) on Quartz Filters*. *October*. Retrieved from http://www.arb.ca.gov/testmeth/slb/sop139v1_1.pdf (accessed on: 04/20/2017).

California Air Resources Board. (2011b). *SOP No. MLD142: Procedure for the Analysis of Particulate Anions and Cations in Motor Vehicle Exhaust by Ion Chromatography*. Retrieved from http://www.arb.ca.gov/testmeth/slb/sop142v2-0.pdf (accessed on: 04/20/2017).

California Air Resources Board. (2011c). *SOP No. MLD145: Procedure for the Determination of Particulate Matter (PM) on Filters*. Retrieved from: http://www.arb.ca.gov/testmeth/slb/sop145v5_1.pdf (accessed on: 04/20/2017).

California Air Resources Board. (2014). *California Air Ressources Board* (Vol. [WWW Docue). Retrieved from https://www.arb.ca.gov/msei/msei.htm (accessed on: 04/20/2017).

Carlton, A. G., Bhave, P. V, Napelenok, S. L., Edney, E. O., Sarwar, G., Pinder, R. W., Pouliot, G., Houyoux, M. (2010). Model Representation of Secondary Organic Aerosol in CMAQv4.7. *Environmental Science & Technology*, *44*(22), 8553–60. https://doi.org/10.1021/es100636q

Carter, W. P. L. (1994). Development of Ozone Reactivity Scales for Volatile Organic Compounds. *Air & Waste*, *44*(7), 881–899. https://doi.org/10.1080/1073161X.1994.10467290

Chan, T. W., Meloche, E., Kubsh, J., Brezny, R., Rosenblatt, D., & Rideout, G. (2013). Impact of Ambient Temperature on Gaseous and Particle Emissions from a Direct Injection Gasoline Vehicle and its Implications on Particle Filtration. *SAE Int. J. Fuels Lubr.*, *6*, 350–371. https://doi.org/10.4271/2013-01-0527

Choi, K., Kim, J., Myung, C.-L., Lee, M., Kwon, S., Lee, Y., & Park, S. (2012). Effect of the Mixture Preparation on the Nanoparticle Characteristics of Gasoline Direct-Injection Vehicles. *Proceedings of the Institution of Mechanical Engineers, Part D: Journal of Automobile Engineering*, *226*(11), 1514–1524. https://doi.org/10.1177/0954407012445534

Cole, R. L., Poola, R. B., & Sekar, R. (1998). Exhaust Emissions of a Vehicle with a Gasoline Direct-Injection Engine. *SAE Technical Paper*, (982605). https://doi.org/10.4271/982605

Drozd, G. T., Zhao, Y., Saliba, G., Frodin, B., Maddox, C., Weber, R. J., Chang, M.-C. O., Maldonado, H., Sardar, S., Robinson, A. L., et al. (2016). Time Resolved Measurements of Speciated Tailpipe Emissions from Motor Vehicles: Trends with Emission Control Technology, Cold Start Effects, and Speciation. *Environmental Science & Technology*, acs.est.6b04513. https://doi.org/10.1021/acs.est.6b04513

EPA and NHTSA. (2012). *2017 and Later Model Year Light-Duty Vehicle Greenhouse Gas Emissions and Corporate Average Fuel Economy Standards; Final Rule* (Vol. 77). Retrieved from: https://www.federalregister.gov/documents/2012/10/15/2012-21972/2017-and-later-model-year-light-duty-vehicle-greenhouse-gas-emissions-and-corporate-average-fuel (accessed on: 04/20/2017).

Federal Highway Administartion, U. S. D. of T. (2016). *Transporation Air Quality Selected Facts and Figures*. Retrieved from http://www.fhwa.dot.gov/environment/air_quality/publications/fact_book/index.cfm (accessed on: 04/20/2017).

FHA. (2011). United States Department of Transportation, Summary of Travel Trends: 2009 National Household Travel Survey, 82. https://doi.org/FHWA-PL-ll-022. Retrieved from: http://nhts.ornl.gov/download.shtml%5Cnhttp://scholar.google.com/scholar?hl=en&btnG=Search&q=intitle:2009+National+Household+Travel+Survey#9 (accessed on: 04/20/2017).

Fujita, E., Chow, J., Bachmann, J., Hsu, Y.-C., Chen, S.-K., Tsai, J.-H., Chiang, H.-L., Zielinska, B., Campbell, D., Arnott, W., et al. (2007). Variations in Speciated Emissions from Spark-Ignition and Compression-Ignition Motor Vehicles in California's South Coast Air Basin. *Journal of the Air & Waste Management Association*, *57*(6), 705–720. https://doi.org/10.3155/1047-3289.57.6.705

Fushimi, A., Kondo, Y., Kobayashi, S., Fujitani, Y., Saitoh, K., Takami, A., & Tanabe, K.

(2016). Chemical Composition and Source of Fine and Nanoparticles from Recent Direct Injection Gasoline Passenger Cars: Effects of Fuel and Ambient Temperature. *Atmospheric Environment*, *124*, 77–84. https://doi.org/10.1016/j.atmosenv.2015.11.017

George, I. J., Hays, M. D., Herrington, J. S., Preston, W., Snow, R., Faircloth, J., George, B. J., Long, T., Baldauf, R. W. (2015). Effects of Cold Temperature and Ethanol Content on VOC Emissions from Light-Duty Gasoline Vehicles. *Environmental Science and Technology*, *49*(21), 13067–13074. https://doi.org/10.1021/acs.est.5b04102

Jacobson, M. Z. (2001). Strong Radiative Heating Due to the Mixing State of Black Carbon in Atmospheric Aerosols. *Nature*, *409*, 695–697. https://doi.org/10.1038/35055518

Jathar, S. H., Gordon, T. D., Hennigan, C. J., Pye, H. O. T., Pouliot, G., Adams, P. J., Robinson, A. L. (2014). Unspeciated Organic Emissions From Combustion Sources and their Influence on the Secondary Organic Aerosol Budget in the United States. *Proceedings of the National Academy of Sciences of the United States of America*, *111*(29), 10473–10478. https://doi.org/10.1073/pnas.1323740111

Jathar, S. H., Woody, M., Pye, H. O. T., Baker, K. R., & Robinson, A. L. (2016). Chemical Transport Model Simulations of Organic Aerosol in Southern California: Model Evaluation and Gasoline and Diesel Source Contributions. *Atmospheric Chemistry and Physics Discussions*, (December), 1–18. https://doi.org/10.5194/acp-2016-1055

Jimenez, J., & Canagaratna, M. (2009). Evolution of Organic Aerosols in the Atmosphere. *Science*, *326*(5959), 1525–1529. https://doi.org/10.1126/science.1180353

Ka, L. C., Polidori, A., Ntziachristos, L., Tzamkiozis, T., Samaras, Z., Cassee, F. R., Gerlofs, M., Sioutas, C. (2009). Chemical Characteristics and Oxidative Potential of Particulate Matter Emissions from Gasoline, Diesel, and Biodiesel Cars. *Environmental Science and Technology*, *43*(16), 6334–6340. https://doi.org/10.1021/es900819t

Karavalakis, G., Short, D., Vu, D., Russell, R., Asa-Awuku, A., & Durbin, T. (2015). A Complete Assessment of the Emissions Performance of Ethanol Blends and Iso-Butanol Blends from a Fleet of Nine PFI and GDI Vehicles. *SAE Int. J. Fuels Lubr.*, *8*, 374–395. https://doi.org/10.4271/2015-01-0957

Karjalainen, P., Pirjola, L., Heikkilä, J., Lähde, T., Tzamkiozis, T., Ntziachristos, L., Ntziachristos, L., Keskinen, J., Rönkkö, T. (2014). Exhaust Particles of Modern Gasoline Vehicles: A Laboratory and an on-Road Study. *Atmospheric Environment*, *97*, 262–270. https://doi.org/10.1016/j.atmosenv.2014.08.025

Kerminen, V. M., & Wexler, A. S. (1995). The Interdependence Of Aerosol Processes And Mixing In Point-Source Plumes. *Atmospheric Environment*, *29*(3), 361–375. https://doi.org/10.1016/1352-2310(94)00262-j

Khalek, I. A., Bougher, T., & Jetter, J. J. (2010). Particle Emissions from a 2009 Gasoline Direct Injection Engine Using Different Commercially Available Fuels. *SAE International Journal of Fuels and Lubricants*, *3*(2), 623–637. https://doi.org/10.4271/2010-01-2117

Kirchstetter, T. W., Singer, B. C., Harley, R. A., Kendall, G. R., & Hesson, J. M. (1999). Impact of California Reformulated Gasoline on Motor Vehicle Emissions. 2. Volatile Organic Compound Speciation and Reactivity. *Environmental Science and Technology*, *33*(2), 329–336. https://doi.org/10.1021/es980374g

Li, Y., Xue, J., Johnson, K., Durbin, T., Villela, M., Pham, L., Hosseini, S., Zheng, Z., Short, D., Karavalakis, G., et al. (2014). Determination of Suspended Exhaust PM Mass for Light-Duty Vehicles. *SAE Technical Paper*. https://doi.org/10.4271/2014-01-1594

Liang, B., Ge, Y., Tan, J., Han, X., Gao, L., Hao, L., Ye, W., Dai, P. (2013). Comparison of PM Emissions from a Gasoline Direct Injected (GDI) Vehicle and a Port Fuel Injected (PFI) Vehicle Measured by Electrical Low Pressure Impactor (ELPI) with Two Fuels: Gasoline and M15 Methanol Gasoline. *Journal of Aerosol Science*, *57*, 22–31. https://doi.org/10.1016/j.jaerosci.2012.11.008

Liu, S., Ahlm, L., Day, D. A., Russell, L. M., Zhao, Y., Gentner, D. R., Weber, R. J., Goldstein, A. H., Jaoui, M., Offenberg, J. H., et al. (2012). Secondary Organic Aerosol Formation from Fossil Fuel Sources Contribute Majority of Summertime Organic Mass at Bakersfield. *Journal of Geophysical Research Atmospheres*, *117*(23). https://doi.org/10.1029/2012JD018170

Mamakos, A., Martini, G., Marotta, A., Manfredi, U. (2013). Assessment of Different Technical Options in Reducing Particle Emissions from Gasoline Direct Injection Vehicles. *Journal of Aerosol Science*, *63*, 115–125. https://doi.org/10.1016/j.jaerosci.2013.05.004

May, A. A., Nguyen, N. T., Presto, A. A., Gordon, T. D., Lipsky, E. M., Karve, M., Gutierrez, A., Robertson, W. H., Zhang, M., Brandow, C., et al. (2014). Gas- and Particle-Phase Primary Emissions from in-Use, on-Road Gasoline and Diesel

Vehicles. *Atmospheric Environment*, *88*, 247–260.
https://doi.org/10.1016/j.atmosenv.2014.01.046

Myung, C. L., Choi, K., Kim, J., Lim, Y., Lee, J., Park, S. (2012). Comparative Study of
Regulated and Unregulated Toxic Emissions Characteristics from a Spark Ignition
Direct Injection Light-Duty Vehicle Fueled with Gasoline and Liquid Phase LPG
(Liquefied Petroleum Gas). *Energy*, *44*(1), 189–196.
https://doi.org/10.1016/j.energy.2012.06.039

National Research Council, C. (2011). *FUEL ECONOMY LIGHT-DUTY VEHICLES
Committee on the Assessment of Technologies for Improving Light-Duty Vehicle
Fuel Economy*. Retrieved from: https://www.nap.edu/catalog/21744/cost-
effectiveness-and- 562 deployment-of-fuel-economy-technologies-for-light-duty-
vehicles (accessed on: 04/20/2017).

NIOSH. (1996). Elemental Carbon (Diesel Particulate): Method 5040. *NIOSH Manual of
Analytical Methods*, *4th ed.*(1st suppl.), National Institute for Occupational Safety
and Health. Retrieved from: https://www.cdc.gov/niosh/docs/2003-
154/pdfs/5040f3.pdf (accessed on: 04/20/2017).

Odum, J. R., Jungkamp, T. P., Griffin, R. J., Flagan, R. C., & Seinfeld, J. H. (1997). The
Atmospheric Aerosol-Forming Potential of whole Gasoline Vapor. *Science (New
York, N.Y.)*, *276*(5309), 96–99. https://doi.org/10.1126/science.276.5309.96

Peckham, M. S., Finch, A., Campbell, B., Price, P., & Davies, M. T. (2011). Study of
Particle Number Emissions from a Turbocharged Gasoline Direct Injection (GDI)
Engine Including Data from a Fast-Response Particle Size Spectrometer. *SAE
Technical Paper*, (2011-01–1224), 1–11. https://doi.org/10.4271/2011-01-1224

Price, P., Stone, R., Collier, T., & Davies, M. (2006). Particulate Matter and Hydrocarbon
Emissions Measurements : Comparing First and Second Generation DISI with PFI
in Single Cylinder Optical Engines. *SAE Technical Paper*, *2006-01–12*(724).
https://doi.org/10.4271/2006-01-1263

Ramanathan, V., & Carmichael, G. (2008). Global and Regional Climate Changes due to
Black Carbon. *Nature Geoscience*. https://doi.org/10.1038/ngeo156

Robert, M. a, VanBergen, S., Kleeman, M. J., & Jakober, C. A. (2007). Size and
Composition Distributions of Particulate Matter Emissions: Part 1--Light-Duty
Gasoline Vehicles. *Journal of the Air & Waste Management Association*, *57*(12),

1414–1428. https://doi.org/10.3155/1047-3289.57.12.1414

Russell, L. M., Takahama, S., Liu, S., Hawkins, L. N., Covert, D. S., Quinn, P. K., Bates, T. S. (2009). Oxygenated Fraction and Mass of Organic Aerosol from Direct Emission and aAtmospheric Processing Measured on the R/V Ronald Brown during TEXAQS/GoMACCS 2006. *Journal of Geophysical Research Atmospheres*, *114*(7). https://doi.org/10.1029/2008JD011275

Saito, C., Nakatani, T., Miyairi, Y., Yuuki, K., Makino, M., Kurachi, H., Heuss, W., Kuki, T., Furuta, Y., Kattouah, P., et al. (2011). New Particulate Filter Concept to Reduce Particle Number Emissions. *SAE Technical Paper Series*. https://doi.org/10.4271/2011-01-0814

Seo, J., Lee, J. S., Choi, K. H., Kim, H. Y., & Yoon, S. S. (2013). Numerical Investigation of the Combustion Characteristics and Wall Impingement with Dependence on Split-Injection Strategies from a Gasoline Direct-Injection Spark Ignition Engine. *Proceedings of the Institution of Mechanical Engineers, Part D: Journal of Automobile Engineering*, *227*(11), 1518–1535. https://doi.org/10.1177/0954407013491216

Short, D., Vu, D., Chen, V., Espinoza, C., Berte, T., Karavalakis, G., Durbin, T. D., Asa-Awuku, A. (2016). Understanding Particles Emitted from Spray and Wall-Guided Gasoline Direct Injection and Flex Fuel Vehicles Operating on Ethanol and Iso-Butanol Gasoline Blends. *Aerosol Science and Technology*, *51*(3), 1–12. https://doi.org/10.1080/02786826.2016.1265080

Spiess, S., Wong, K. F., Richter, J. M., Klingmann, R. (2013). Investigations of Emission Control Systems for Gasoline Direct Injection Engines with a Focus on Removal of Particulate Emissions. *Topics in Catalysis*, *56*(1–8), 434–439. https://doi.org/10.1007/s11244-013-9992-6

Stacy C. Davis, Susan E. Williams, Robert G. Boundy, Sheila Moore. (2015). *2015 Vehicle Technologies Market Report*. Retrieved from http://cta.ornl.gov/vtmarketreport/pdf/2015_vtmarketreport_full_doc.pdf (accessed on: 04/20/2017).

Storey, J. M., Lewis, S., Szybist, J., Thomas, J., Barone, T., Eibl, M., Nafziger, E., Kaul, B. (2014). Novel Characterization of GDI Engine Exhaust for Gasoline and Mid-Level Gasoline-Alcohol Blends. *SAE International Journal of Fuels and Lubricants*,

7(2), 571–579. https://doi.org/10.4271/2014-01-1606

Turpin, B. J., & Lim, H.-J. (2001). Species Contributions to PM2.5 Mass Concentrations: Revisiting Common Assumptions for Estimating Organic Mass. *Aerosol Science and Technology*, *35*(February), 602–610. https://doi.org/10.1080/02786820119445

Weilenmann, M. F., Soltic, P., Hausberger, S. (2013). The Cold Start Emissions of Light-Duty-Vehicle Fleets: A Simplified Physics-Based Model for the Estimation of CO2 and Pollutants. *Science of the Total Environment*, *444*, 161–176. https://doi.org/10.1016/j.scitotenv.2012.11.024

Worton, D. R., Isaacman, G., Gentner, D. R., Dallmann, T. R., Chan, A. W. H., Ruehl, C., Kirchstetter, T. W., Wilson, K. R., Harley, R. A., Goldstein, A. H. (2014). Lubricating Oil Dominates Primary Organic Aerosol Emissions from Motor Vehicles. *Environmental Science and Technology*, *48*(7), 3698–3706. https://doi.org/10.1021/es405375j

Zhang, S., & McMahon, W. (2012). Particulate Emissions for LEV II Light-Duty Gasoline Direct Injection Vehicles. *SAE Int. J. Fuels Lubr.*, *5*, 637–646. https://doi.org/10.4271/2012-01-0442

Zhao, F., Lai, M. C., & Harrington, D. L. (1999). Automotive Spark-Ignited Direct-Injection Gasoline Engines. *Progress in Energy and Combustion Science*, *25*(5), 437–562. https://doi.org/10.1016/S0360-1285(99)00004-0

Zimmerman, N., Wang, J. M., Jeong, C.-H., Ramos, M., Hilker, N., Healy, R. M., Sabaliauskas, K., Wallace, J. S., Evans, G. J. (2016). Field Measurements of Gasoline Direct Injection Emission Factors: Spatial and Seasonal Variability. *Environmental Science & Technology*, *50*(4), 2035–43. https://doi.org/10.1021/acs.est.5b04444

Zimmerman, N., Wang, J. M., Jeong, C.-H., Wallace, J. S., & Evans, G. J. (2016). Assessing the Climate Trade-Offs of Gasoline Direct Injection Engines. *Environmental Science & Technology*, acs.est.6b01800. https://doi.org/10.1021/acs.est.6b01800

CHAPTER 5

EFFECTS OF PARTICLE SEEDS ON CONDENSATIONAL GROWTH RATES: DIESEL AND SECONDARY ORGANIC AEROSOL PARTICLES[4]

5.1 Introduction

Growth of particles is ubiquitous in the atmosphere. Various biogenic sources (biomass burning, forests, oceans, volcanic eruptions, etc.) and anthropogenic sources (on-road and off-road diesel, industry, agriculture, etc.) emit copious amounts of gas- and particle-phase compounds. These emissions interact with radiation in complex ways. On top of the direct radiative effects of gas- and particle-phase emissions (absorption and scattering), cloud condensation nuclei (CCN, particles that act as seeds for cloud droplets) play a highly uncertain impact on the lifetime and brightness of clouds, which affect the overall radiative budget of the earth (Twomey, 1977; Lohmann and Lesins, 2002; Rosenfeld, 2006). However, we do not fully understand the processes controlling the atmospheric CCN concentrations (Riipinen et al., 2012).

Condensation of organics is primarily responsible for growing ultrafine (<100 nm) particles into CCN sizes (Riipinen et al., 2012). Depending on atmospheric conditions and thermodynamics, gas-phase semi-volatile and low volatility compounds will partition to the particle-phase and either condense onto existing seeds or homogeneously nucleate to form new particles (Donahue et al., 2006; Riipinen et al., 2012). Growth of particles by condensation depends on gas-phase conditions but is also sensitive to the chemical composition of the particle surface. For example, differences in surface activity can impact

---

the condensation growth of particles by suppressing the surface concentration "seen" by the gas-phase (Seinfeld and Pandis, 2006). Therefore, differences in growth rates have a direct impact on the survival probability of different particles to make it to CCN sizes.

Seed particle effects (notably from seed acidity) have been previously shown to significantly increase secondary organic aerosol (SOA) yields due to reactive uptake of vapors from acid-catalyzed heterogeneous reactions (Czoschke et al., 2003; Lambe et al., 2015; Han et al., 2016). However, field measurements showed modest to no enhancements of organic mass on acidic particles (Takahama et al., 2006; Zhang et al., 2007). Moreover, there is little data in the literature that probe the growth of anthropogenic particle emissions.

Black carbon (BC), a product of incomplete combustion, is the most potent light-absorbing component of anthropogenic particulate matter (PM), with a top of the atmosphere direct radiative forcing only second to CO_2 (IPCC 2013). Freshly emitted BC particles are usually small in size (~100 nm) and hydrophobic; they therefore make poor CCNs (Weingartner et al., 1997). However, BC particles are oxidized and coated in the atmosphere on time scales of hours to days to become more hydrophilic (Riemer et al., 2004; Moffet and Prather, 2009; Subramanian et al., 2010). This atmospheric processing of BC particles affects their optical properties and lifetime. Growth of BC particles (i.e., the amount of coating around BC cores) enhances their absorption (Schnaiter, 2005; Shiraiwa et al., 2010; Saliba et al., 2016), which affects their direct top-of-the atmosphere radiative forcing (Jacobson, 2001). Moreover, growth of BC particles affects their deposition rate, hence their lifetime. Finally, condensational growth of BC particles increases their size and enhances their affinity to water vapor, making them more efficient CCNs (Kuwata et al., 2009).

Temporal differences in the growth rates of particles have previously been measured in the field (Stolzenburg et al., 2005). However, these differences could be due to a multitude of factors, including changing gas-phase conditions due to mixing and transport. Laboratory experiments that directly probe the growth rates of different seed particles exposed to the same gas-phase supersaturation conditions and let to evolve jointly are challenging. This is because atmospheric particle growth rarely exceed ~10 nm/hr (Weber et al., 1997; Kulmala et al., 2004; Dal Maso et al., 2005; Stolzenburg et al., 2005). Typical growth rates of seed particles in the laboratory are one- to two- orders of magnitudes higher than what is observed in the field; thus, lower growth rates are needed to probe atmospheric range. Moreover, it is difficult to accurately estimate the growth rates of different particles in chamber experiments due to the difficulty to physically distinguish between the seeds. Differences in growth rate conditions (atmospheric versus laboratory conditions) could have implications on the growth behavior of the particles, but this remains highly uncertain.

We conducted chamber experiments targeting the condensation growth of particles under different growth rates. We present a novel method to retrieve growth rates of different particles exposed to the same gas-phase conditions. Using this setup, we performed several experiments using different seed particles (biogenic SOA particles and anthropogenic diesel exhaust particles) as well as different condensate materials (biogenic SOA and squalane). We covered a wide range of growth rates: from atmospherically relevant conditions (a few nm/hr) to growth rates typical of chamber experiments (hundreds of nm/hr). Using these data and theoretical formulation for condensational growth, we probed the effect of various supersaturation conditions and seed composition on growth rates.

5.2 Methods

5.2.1 Experimental Setup

The experimental setup is shown in Figure 5.1. We compared the condensation growth of two distinct seeds inside an 8 m^3 Teflon chamber. The seeds were selected to be atmospherically relevant: diesel exhaust as a surrogate for anthropogenic particles and SOA from the ozonolysis of alpha-pinene (αp, Sigma Aldrich, 99.0%) as an important type of biogenic particles. Similarly, coating materials were selected to be atmospherically relevant: For six experiments (experiments 1 through 6 detailed in Table 5.1) we coated the two seeds with αp-SOA. For two other experiments (experiments 7 and 8 detailed in Table 5.1), we coated the two seeds with squalane (C$_{30}$H$_{62}$, Sigma Aldrich, 99.0%). The choice of these condensate material is supposed to represent condensation from anthropogenic and biogenic gas-phase emissions.
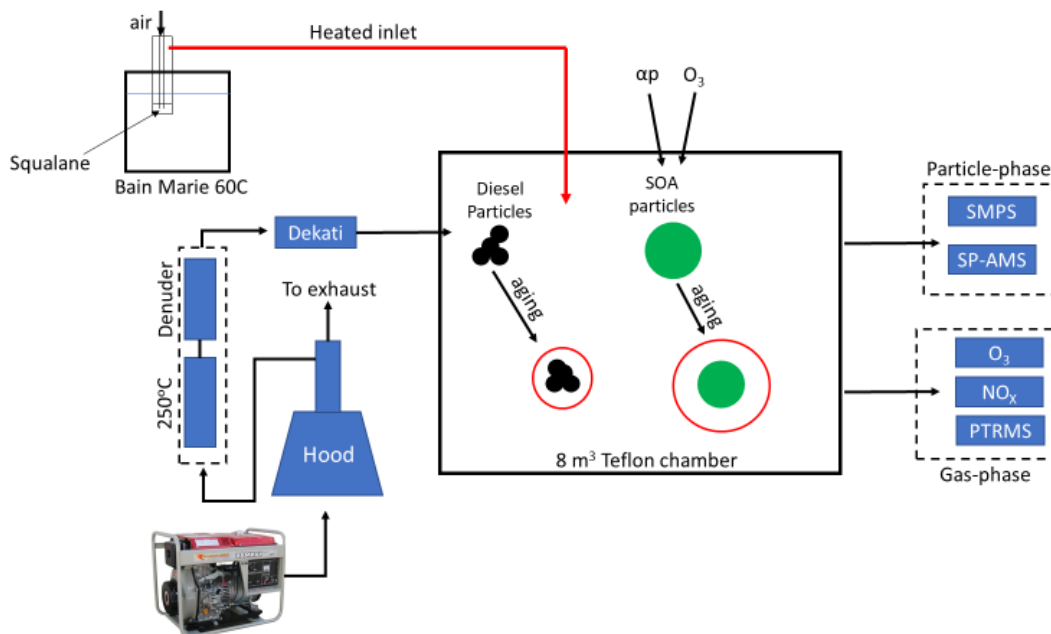
Figure 5.1 Experimental Setup.

To accurately retrieve the growth rates of the different seeds, it was necessary to: (1) have both seed particles in the chamber at the same time (i.e., exposed to the same gas-phase conditions), and (2) physically differentiate between the two seed populations. Diesel exhaust particles were characterized by a mode mobility diameter of ~50 nm. Thus, to physically differentiate between diesel and SOA particles, we started all experiments (except for experiment 8; Table 5.1) by nucleating and growing αp-SOA particles up to a mode mobility diameter of ~150 nm. This ensured that when we subsequently injected the diesel particles, the two seeds were size separated.

A typical experiment consisted of the following steps. First, we injected ~1.5 μL αp using a needle into a heated septum line. Filtered air (through a series of high-efficiency particulate air (HEPA) filters and activated carbon scrubbers (for VOC removal)) carried the αp vapors to the chamber. After αp concentrations achieved steady-state, we would inject ~100 ppb of O_3 inside the chamber. O_3 was generated by passing a flow of pure O_2 inside a corona discharge ozone generator. The mixing of O_3 and αp vapors inside the chamber initiated the dark ozonolysis of αp (Presto et al., 2005; Presto and Donahue, 2006), resulting in the nucleation and subsequent growth (up to a mode mobility diameter of ~150 nm) of αp-SOA particles.

Second, after the chemistry slowed down, i.e., αp concentrations measured using a proton transfer reaction mass spectrometer (PTR-MS) were below 0.2 ppbs, we injected diesel exhaust. The generator was running at a 70% load to maximize BC emissions. The entire emission was diluted inside a hood, from which a 2 LPM slipstream (pulled by a Dekati diluter positioned upstream, Figure 5.1) passed through a thermodenuder operating at ~250°C then through an activated carbon denuder section (to remove NOx) prior to injection inside the chamber. The engine was operated until we achieved number

concentrations greater than 20,000 particles/cm^3 inside the chamber (typically a few minutes). The engine was fueled with a commercially available 10% biodiesel blend (B10).

The fresh diesel particle mode particle diameter was ~50 nm compared to a mode diameter of ~150 nm for the grown SOA particles. This difference in mode diameters ensured that the two size distributions were physically distinct to allow for accurate retrieval of the growth rates from both seed particles.

Finally, we would start the condensational growth. For experiments using biogenic SOA coating, we continued adding intermittent amounts of αp vapors (<0.1 µL) inside the chamber with O_3 concentrations lower than 80 ppb to ensure slow kinetics. For experiments using squalane as a coating material, a 2.0 LPM HEPA- and activated carbon-filtered air flow passed through a bubbler (sitting in a bain-Marie at 60ºC) containing liquid squalane before entering the chamber (Figure 5.1). The tubing between the outlet of the bubbler and the chamber inlet was heated to ensure minimum losses of squalane vapors.

Table 5.1 Experimental Matrix.

Exp. #	1st seed	Mode diameter (nm)	2nd seed	Mode diameter (nm)	Coating material	Slope$^\$$ $(\overline{\alpha_1}/\overline{\alpha_2})$	y-intercept$^\$$ ($\propto \overline{\alpha_1}(a_2 - a_1)$)
1	diesel	68.5	αp-SOA	181.1	αp-SOA	0.71±0.05	-2.7±1.0
2	diesel	66.1	αp-SOA	190.0	αp-SOA	0.77±0.07	-1.4±0.7
3	diesel	53.3	αp-SOA	168.5	αp-SOA	0.88±0.17	-0.5±1.8
4	diesel	51.4	αp-SOA	194.6	αp-SOA	0.88±0.03	-0.9±0.7
5	diesel	46.1	αp-SOA	156.8	αp-SOA	0.68±0.02	0.0±2.5
6	diesel	55.2	αp-SOA	181.1	αp-SOA	0.81±0.03	-1.1±0.6
7	diesel	49.6	αp-SOA	150.0	Squalane	0.85±0.05	-4.5±0.6
8	diesel	55.2	αp-SOA	162.5	Squalane	0.71±0.2	-4.2±2.3
9$^\downarrow$	diesel	-	-	-	-	-	-
10*	αp-SOA	Nucleated	αp-SOA	201.3	αp-SOA	0.99±0.01	-0.3±0.0
11*	αp-SOA	Nucleated	αp-SOA	191.3	αp-SOA	1.01±0.02	-0.1±0.0

*are control experiments. $^\downarrow$corresponds to a single experiment during which we characterized the chemical composition of the diesel particles. $^\$$data are obtained when fitting to a straight line the normalized growth rates (nGR) for diesel particles versus the nGR for SOA particles. Slope data are corrected for size artifacts [see section 5.3.1].

5.2.2 Instrumentation

Real-time particle size distributions were measured using a scanning mobility particle sizer (SMPS, [TSI Inc.]) for particles with mobility diameter between 14.6 nm to 662.5 nm. The SMPS was calibrated using PSL spheres with 100 and 300 nm spherical diameters and the size registered by the SMPS were within the size uncertainty reported by the manufacturer. The SMPS sample and sheath flows were 0.3 LPM and 3.0 LPM respectively.

Unit-resolution mass spectra were measured using a soot photometer aerosol mass spectrometer (SP-AMS, [Aerodyne, Inc.]) for particles with aerodynamic diameter between 50.0 nm to 1.0 µm (Onasch et al., 2012). The laser module of the SP-AMS (SP2, [Droplet Measurement Technologies]) uses a 1064 nm laser that vaporizes the refractory black carbon (rBC) material. C_x fragments (x is a positive integer) from the vaporized refractory BC (rBC) particles are then counted mass spectrometer. The SP-AMS alternated between a one-minute cycle with the laser off and vaporizer and a one-minute cycle with the laser on and vaporizer on configuration. The laser on vaporizer on configuration allows us to estimate the organics that are only present on the rBC particles.

Gas-phase volatile organic compounds (VOCs) were measured using a quadrupole proton transfer reaction mass spectrometer (PTR-MS, [Ionicon]). We calibrated the PTR-MS using a mixture of 20 VOC compounds with concentrations below 50 ppb, in the range of concentrations we expected during the experiments.

Finally, we measured O_3 and NOx concentrations in the chamber using an ozone monitor (Dasibi) and a chemiluminescent NOx monitor (Advanced Pollution Instrumentation, model 200A).

5.2.3 Framework of Condensational Growth

The growth of particles is governed by the mass transfer of condensing vapors to the particle surface. In the kinetic regime (particle diameter small compared to the mean free path), the flux of condensing material to the particle surface is governed by Equation 5.1 (Seinfeld and Pandis, 2006):

$$J_{kin} = 4\pi R_p^2 \bar{\alpha} \frac{\bar{c}}{4} (C^\infty - C^s) \text{ (5.1)}$$

where R_p is the particle radius, $\bar{\alpha}$ is the average mass accommodation coefficient, $\frac{\bar{c}}{4}$ is the mean Maxwell-Boltzmann ideal velocity of condensing vapors normal to the particle surface, C^∞ is the concentration of condensing vapors away from the surface and C^s is the concentration of condensing vapors at the particle's surface. The mass accommodation coefficient ($\bar{\alpha}$) accounts for surface accommodation, deviations from the Maxwell-Boltzmann ideal velocity distribution, and for mass transfer limitation in the particle-phase. We use an average notation for α ($\bar{\alpha}$) in Equation 5.1 because condensing material can have different volatilities and we therefore lump their overall contribution into an effective α.

For the size range considered here, particle diameters are comparable to the mean free path. This is the transition regime. We can correct the flux of condensing vapors from kinetic theory (J_{kin}) to account for deviations from the kinetic regime (J) using the Fuchs-Sutugin factor (FS), (Fuchs et al., 1971). FS is a dimensionless quantity.

$$FS = \frac{J}{J_{kin}} = \frac{kn(1 + Kn)}{kn^2 + kn + 0.283.kn + 0.75} \text{ (5.2)}$$

$$Kn = 2\lambda/d_p \text{ (5.3)}$$

Combining Equations 5.1, 5.2, and 5.3, we can explicitly express the particle growth rate $\left(\frac{d(R_p)}{dt}\right)$ as a function of gas-phase conditions (C^∞):

123

$$\frac{d(m_p)}{dt} = J$$

$$\frac{d(m_p)}{dt} = \frac{d\left(\frac{4}{3}\pi R_p^3 \rho_p\right)}{dt} = \frac{4}{3}\pi \left\{ R_p^3 \frac{d(\rho_p)}{dt} + \rho_p R_p^2 \frac{d(R_p)}{dt} \right\}$$

$$= \frac{4}{3}\pi \left\{ \rho_p R_p^2 \frac{d(R_p)}{dt} \right\} \ (constant \ \rho_p)$$

$$=> \frac{4}{3}\pi \left\{ \rho_p R_p^2 \frac{d(R_p)}{dt} \right\} = FS(R_p) 4\pi R_p^2 \bar{\alpha} \frac{\bar{c}}{4} (C^\infty - C^s)$$

$$=> \frac{d(R_p)}{dt} = \frac{3.FS(R_p)}{\rho_p} \bar{\alpha} \frac{\bar{c}}{4} (C^\infty - C^s) \ (5.4)$$

Where R_p is the particle radius, m_p is the particle mass, ρ_p is the particle density, and $FS(R_p)$ is the Fuchs-Sutugin correction factor at each size. The term multiplying C^∞ can be thought of the flux of condensing vapors towards the particle's surface (condensation) and the term multiplying C^s can be thought of as the flux of material leaving the particle's surface through (evaporation), (Vehkamäki and Riipinen, 2012). Thus, a positive concentration gradient implies net condensation to the particle surface (addition of mass and particle growth). We can show that for the case of condensing material that is different from the seed material (i.e., the particle density is no longer constant), Equation 5.4 still holds, with the density being that of the condensing vapors.

In Equation 5.4 we assume that particles are spherical. However, BC particles for example, are fractal (Slowik et al., 2004; Sorensen, 2011; China et al., 2013). For non-spherical particles, the definition of particle radius becomes ambiguous. The SMPS-based mobility diameter is proportional to the projected area of the particles (Sorensen, 2011). Thus, fractal particles have a larger mobility diameter compared to their volume equivalent diameter. The volume equivalent diameter (d_{ve}) is related to the mobility diameter (d_m)

through the dynamic shape factor (χ) and the Cunningham slip correction factor (C_c), (DeCarlo and Slowik, 2004):

$$d_{ve} = \frac{d_m C_c(d_{ve})}{\chi C_c(d_m)} \quad (5.5)$$

For diesel particles (emitted from a diesel generator) with mobility diameter around 50 nm (as is the case in this study), a typical dynamic shape factor is ~1.1 (Park et al., 2004). Under these conditions, treating the BC particles as spherical with a diameter equal to their mobility diameter results in a 15% error (accounting for different C_c values). In this study we neglected particle shape and used the mobility diameter as the "true" particle diameter.

5.2.4 Slow versus Fast Growth Limits and Particle Seed Effects

We first consider the implications of performing growth experiments under atmospherically relevant conditions versus typical chamber conditions. One of the objectives of this work is to answer the following question: are there differences in particle growth rates when aged under atmospherically relevant conditions that would not be apparent under high supersaturation conditions?

We first consider implications of performing coating experiments under fast growth conditions. In this case, gas-phase concentrations greatly exceed surface saturation concentrations, i.e., $s = \frac{C^\infty}{C^s} \gg 1$. This implies that condensation growth is dominated by gas-phase conditions, and Equation 5.4 becomes:

$$\frac{d(d_p)}{dt} = \frac{3FS(d_p)}{2\rho_v} \bar{\alpha} \frac{\bar{c}}{4} (C^\infty - C^s) \simeq \frac{3FS(d_p)}{2\rho_v} \bar{\alpha} \frac{\bar{c}}{4} C^\infty \quad (5.6)$$

Where ρ_v is the density of the condensate material. If two seed particles (indexed 1 and 2) are exposed to the same gas-phase conditions, we can hence conclude that, under high

saturation, growth rates of both seeds are proportional to the ratio of their mass accommodation coefficient:

$$\frac{d(d_p)}{dt}\bigg|_1 = \left(\frac{\overline{\alpha_1}}{\overline{\alpha_2}}\frac{FS(d_p)_1}{FS(d_p)_2}\right)\frac{d(d_p)}{dt}\bigg|_2 \quad (5.7)$$

When growth rates are slow (i.e., $C^\infty \simeq C^s$), seed composition starts to determine particle growth. To highlight the contribution of seed particles to their growth rates, it is useful to decompose the surface concentration (C^s) into the product of the activity (a), the Kelvin curvature effect, and the vapor saturation concentration ($C^*(T)$, a thermodynamic property), i.e., $C^s = aKC^*$. The activity can be written as the product of the mole fraction of species i in the aerosol phase (x_i, Raoult's law) and the activity coefficient (γ, which accounts for deviations from an ideal solution); $a = x_i\gamma$. C^s is the surface concentration "seen" by the gas-phase. Therefore, growth of particles can be written as:

$$\frac{d(d_p)}{dt} = \frac{3FS(d_p)}{2\rho_v}\overline{\alpha}\frac{\overline{c}}{4}(C^\infty - C^s) = \frac{3FS(d_p)}{2\rho_v}\overline{\alpha}\frac{\overline{c}}{4}C^*(s - aK) \quad (5.8)$$

In this study, we neglected the Kelvin term (K=1) for SOA particles because of their large diameters ($d_{SOA} > 150$ nm). However, diesel particles were characterized by a mode diameter of ~50 nm. Furthermore, diesel particles are an aggregation of carbon monomers with typical diameters between 20 to 30 nm (i.e., at the upper limit where the Kelvin effect can still matter). Assuming an average molecular weight of 400 g/mol and an average surface tension of 0.03 N/m for the condensate material, we estimate that the Kelvin term increases the saturation vapor pressure by 50% (K=1.5). We can now relate the growth rates of diesel and SOA particles.

$$\frac{d(d_p)}{dt}\bigg|_1 = \frac{3FS(d_{p_1})}{2\rho_v}\overline{\alpha_1}\frac{\overline{c}}{4}C^*(s - a_1K_1)$$

$$\frac{d(d_p)}{dt}\bigg|_2 = \frac{3FS(d_{p_1})}{2\rho_v}\overline{\alpha_2}\frac{\bar{c}}{4}C^*(s - a_2)$$

$$\Rightarrow \frac{d(d_p)}{dt}\bigg|_1 = \frac{3FS(d_{p_1})}{2\rho_v}\overline{\alpha_1}\frac{\bar{c}}{4}C^*(s - a_1K_1 + a_2 - a_2)$$

$$= \frac{3FS(d_{p_1})}{2\rho_v}\overline{\alpha_1}\frac{\bar{c}}{4}C^*(s - a_2K_2) + \frac{3FS(d_{p_1})}{2\rho_v}\overline{\alpha_1}\frac{\bar{c}}{4}C^*(a_2 - a_1K_1)$$

$$= \frac{\overline{\alpha_1}}{\overline{\alpha_2}}\frac{FS_1}{FS_2}\frac{d(d_p)}{dt}\bigg|_2 + \frac{3FS(d_{p_1})}{2\rho_v}\overline{\alpha_1}\frac{\bar{c}}{4}C^*(a_2 - a_1K_1)$$

$$\Rightarrow \frac{d(d_p)}{dt}\bigg|_1 = \left(\frac{\overline{\alpha_1}}{\overline{\alpha_2}}\frac{FS_1}{FS_2}\right)\frac{d(d_p)}{dt}\bigg|_2 + \frac{3FS_1}{2\rho_v}\overline{\alpha_1}\frac{\bar{c}}{4}C^*(a_2 - a_1K_1) \quad (5.9)$$

5.2.5 SMPS-based Growth Rates

The growth rates of particles were measured using the SMPS. So far, we have considered growth of a monodisperse aerosol. Our experiments had polydisperse particle populations. Therefore, we represent the entire polydisperse aerosol using a single diameter: its geometric mean diameter (d_{geo}), and growth rates ($GR \equiv \frac{d(d_{geo})}{dt}$) are given by Equation 5.10:

$$GR = \frac{\left(d_{geo}(t) - d_{geo}(t-1)\right)}{\Delta t} \quad (5.10)$$

Growth rates are a function of particle size (through the Fuchs-Sutugin correction factor). Therefore, chemically identical particles but with distinct sizes will have different growth rates when exposed to the same gas-phase supersaturation. To account for this size artifact, we normalized GR to their respective Fuchs-Sutugin factors. This normalized GR (nGR) also has the units of nm/hr. Particles with the same chemical composition but different diameters exposed to the same gas-phase conditions, will have the same nGR (but not the same GR).

$$nGR = \frac{GR(d_p)}{FS(d_p)} \quad (5.11)$$

We can now summarize the final growth equations that are subsequently used in the result section, using nGR notation. Equation 5.12 applies for fast growth rates and Equation 5.13 applies otherwise.

$$\boldsymbol{nGR_1 = \left(\frac{\overline{\alpha_1}}{\overline{\alpha_2}}\right) nGR_2 \qquad for\ s \gg a} \quad (5.12)$$

$$\boldsymbol{nGR_1 = \left(\frac{\overline{\alpha_1}}{\overline{\alpha_2}}\right) nGR_2 + A\overline{\alpha_1}(a_2 - a_1 K_1) \qquad otherwise} \quad (5.13)$$

Where $\overline{\alpha_1}$ and $\overline{\alpha_2}$ are the mass accommodation coefficients for the condensing material on the diesel and SOA particles respectively, a_1 and a_2 are the particle-phase activities for the condensate material on the diesel and SOA particles respectively, K is the Kelvin effect, and A is a constant $\left(A = \frac{3}{2\rho_v} \frac{\bar{c}}{4} C^*\right)$.

5.2.6 Control Experiments and Experimental Repeatability

We performed two control experiments (experiments 10 and 11 detailed in Table 5.1) to compare the growth rates of two chemically identical particles (but having distinct sizes). The goal of these experiments is to confirm that we get identical values for nGR from both seed particles.

For these experiments, we nucleated twice αp-SOA at separate times to physically distinguish them in the SMPS. After nucleating and growing the first SOA mode (typical mode mobility diameter of ~200 nm) we initiated the second nucleation event. To nucleate a second time, we waited until the surface area of the first SOA distribution was ~10^8 nm²/cm³, and then injected   1 µL of αp under ~400 ppb of O_3. These conditions insured that the condensation sink was sufficiently low to thermodynamically favor nucleation.

Experimental repeatability was estimated by the relative standard deviation of the slope of nGR (large SOA versus small SOA particles) for both experiments.

5.3 Results

To illustrate the experimental approach, the temporal evolution of mobility-based number distributions for the diesel and αp-SOA particles is shown in Figure 5.2, for a typical experiment (experiment 4, listed in Table 5.1). Both distributions are well captured by the SMPS and are clearly separated, allowing for accurate retrieval of growth rates for both modes.
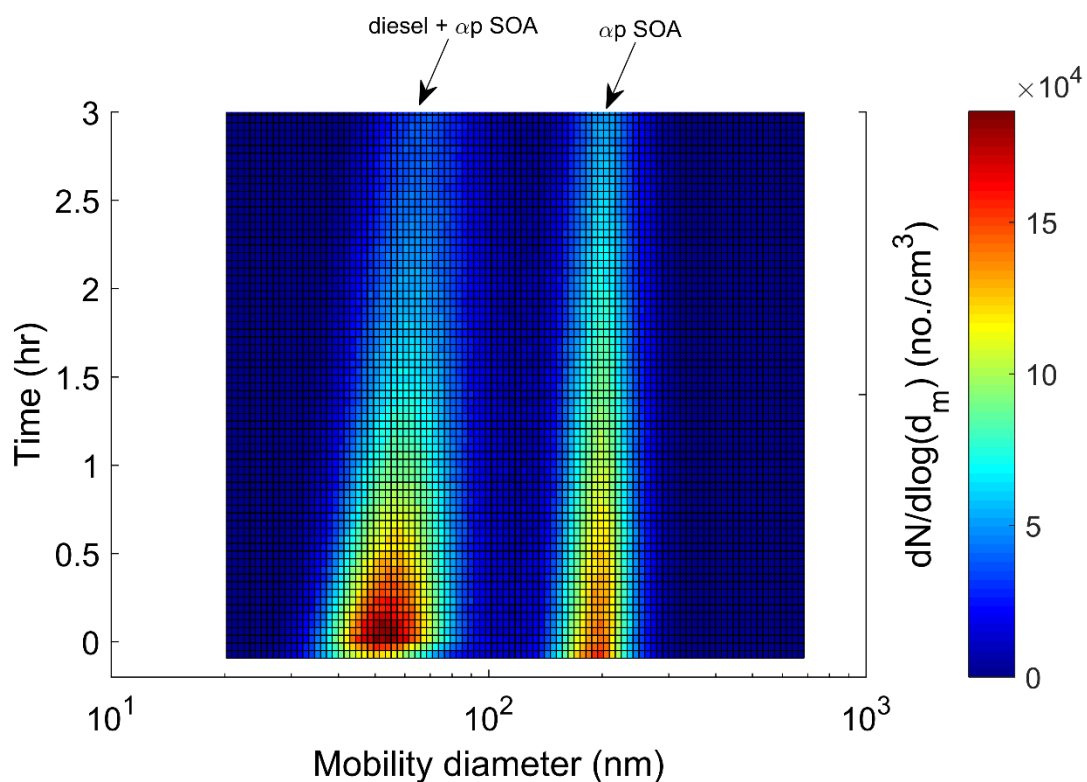
Figure 5.2 Temporal evolution of the number distribution for diesel particles (leftmost distribution) and αp-SOA nucleated particles (rightmost distribution). t=0 is the time at which we injected diesel emissions inside the chamber. Colors indicate particle number concentrations in each logarithmic diameter binning (dN/dlog(d)).

The smaller diesel particles were lost to the chamber's walls faster than the larger SOA particles due to their higher diffusion. For example, after three hours of growth, the mode number concentration of the diesel particles decreased 5-fold compared to a 3-fold decrease in the mode number concentrations of SOA particles. Even though wall losses are significant, they had a negligible impact on the geometric mean diameter of the distributions; the geometric diameter was nearly constant during wall loss dominated periods, potentially due to narrow size distributions and consistent with findings from Saleh et al., (2013).

The information contained in Figure 5.2 is presented differently in Figure 5.3. Figure 5.3a plots time series for the geometric mean diameters of the two particle modes (diesel and nucleated SOA) shown in Figure 5.2. The geometric mean diameter for diesel particles increased from ~75 nm to ~94 nm during 3 hours of growth; this is an average growth rate of 8 nm/hr. Similarly, nucleated SOA particles grew 15 nm in 3 hours, averaging at 5 nm/hr growth.

The growth rates of the two particle populations varied throughout the experiment, as shown in Figure 5.3b. We tried to keep the growth rate around 10 nm/hr, which is at the high end of atmospheric conditions by injecting intermittently very small amounts of αp vapors (visible as bumps in Figure 5.3b).

Clearly, noise in the geometric mean diameter during periods of little growth were amplified when calculating nGRs (Figure5.3). Therefore, some degree of smoothing of the data were necessary. For example, with no smoothing in the data, the average 3% noise in the geometric mean diameter of SOA particles corresponded to a 300% variability in the calculated nGR. Smoothing the geometric mean data (using a moving average algorithm

over a number N data points) reduced the variability in the calculated nGR to an average of 40%. N was typically equal to 20.
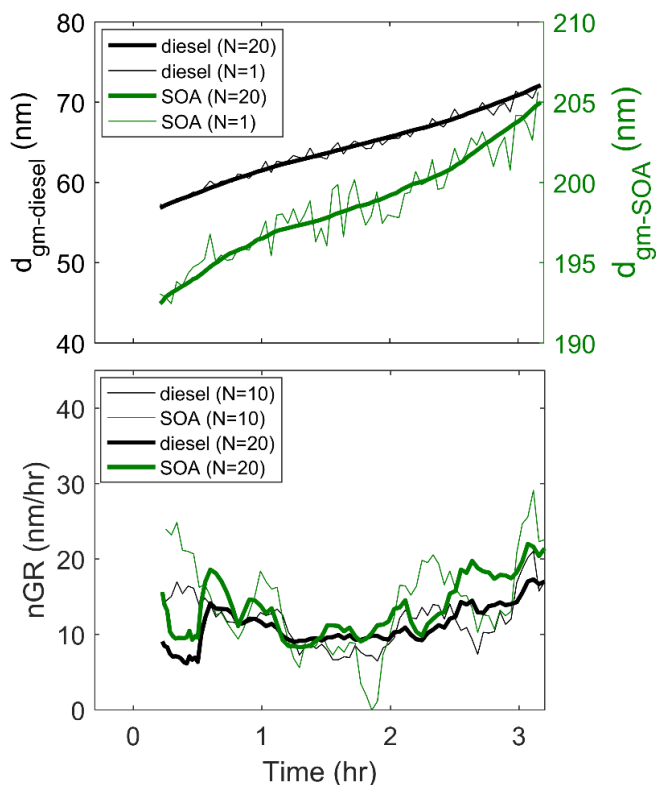
Figure 5.3 Particle growth using geometric mean diameters as surrogates for the entire distributions. (a) Time series of geometric mean diameters for diesel particles (black lines) and SOA particles (green lines). Thick lines in (a) are geometric mean diameter after smoothing the data (N=20) and thin lines in (a) are the raw SMPS data (N=1); where N is the number of points in the moving average. (b) Time series for the normalized growth rates (nGR) calculated from the data shown in (a). Thick lines in (b) use geometric mean diameter data from (a) smoothed over N=20 points, and thin lines in (b) use geometric mean diameter data from (a) smoothed over N=10 points.

5.3.1 Results from Control Experiments

We performed two control experiments (experiments 10 and 11, Table 5.1) to quantify size-related biases and repeatability of our experimental setup. The results from both experiments are shown in Figure S1.

We found a consistent linear bias between the larger (older) SOA particles and the smaller (freshly nucleated) SOA particles (R^2=0.99). This measured difference in growth

rates could reflect biases in: (1) using a single diameter (the geometric mean diameter) as representative of the entire size distribution, (2) a size-dependent charge bias in the neutralizer, and (3) bias in the empirical formulation of the Fuchs-Sutugin correction factor. We corrected for this size bias by linearly fitting the data in Figure S1 and applied this empirical correction to the larger particles for all our experiments.

The two repeat experiments agreed very well with one another. We estimated the experimental repeatability of our system to be the relative standard deviation from the two slopes shown in Figure S1. This yields a value of ±4%.

5.3.2 Chemical Composition of Fresh Denuded Diesel Particles

Figure S2 shows unit-resolution mass spectra from the SP-AMS (panel (a)) and vacuum aerodynamic mass distributions (panel (b)) for diesel particles for an experiment during which we only injected denuded diesel exhaust (experiment 9 in Table 5.1). The data are from the laser on, vaporizer on, mode. Also shown in Figure S2 is the SMPS-based mobility mass distribution for the fresh denuded diesel particles. The mobility distribution had a mode diameter of 50 nm, which is a factor of three smaller than the vacuum aerodynamic mode diameter (not accounting for particle density). This difference is not due to highly fractal-like diesel particles but reflects the inability of the AMS to capture the full diesel particle distribution.

Even though we only captured the tail of the diesel particle distribution, we used the AMS qualitatively to investigate the chemical composition of denuded diesel particles. The AMS spectra signals were separated into three main categories: organics (C_xH_y and $C_xH_yO_z$ fragments), refractory BC (C_x fragments, x is a positive integer), and fullerenes (carbon clusters $C_x > C_{20}$). The C_1^+, C_2^+, and C_3^+ fragments contributed ~2% of the total rBC signal.

This is surprisingly low compared to results from previous studies who report that the C_1^+ to C_3^+ fragments contributed around 20% of total rBC signal for Ethelyn flame BC particles (Onasch et al., 2012) and more than 60% of total rBC signal for regal black particles and turbine engine BC particles (Corbin et al., 2014). This could be due to the large particle losses in the AMS inlet in our experiments. The measured C_1^+/C_3^+ for diesel particles was 0.62, in agreement with Corbin et al., (2014).

Substantial amounts of organic material coated the BC particles; the average organic-to-rBC mass ratio was ~1.5 for fresh denuded diesel emissions. The presence of this organic shell around the BC cores implies that condensation growth of diesel particles is governed by the layer of organics and not by adsorption to the BC surface. Coating material exhibited hydrocarbon-like chemical signatures (C_xH_y): prominent signal at m/z 55 and 57 and very low signal from at m/z of 60, consistent with hydrocarbon-like organic aerosols (Mohr et al., 2009).

5.3.3 Particle Growth Rates: Diesel versus SOA Particles

We now compare the normalized growth rates (from SMPS measurements) from diesel and SOA particles. Figure 5.4 is a log-log plot of nGR for denuded diesel particles versus nGR for SOA particles, for all experiments listed in Table 5.1, except experiment 9. The data in Figure 5.4 have been corrected for all size biases (FS correction factor and the experimental-based size bias; see section 5.3.1).

The growth rate of SOA particles almost always exceeded that of diesel particles (all data points are below the 1:1 line), regardless of growth rate (i.e., fast versus slow) or condensate material (αp-SOA or squalane). Moreover, differences in growth rates between diesel and SOA particles seem to be more pronounced at smaller growth rates. This

important observation signifies that atmospheric particles may also exhibit differences in their growth rates. The data in Figure 5.4 demonstrates our ability to achieve low growth rates (<10 nm/hr). The range of growth rates covered in this study spans two orders of magnitude; from a few nm/hr up to 250 nm/hr.
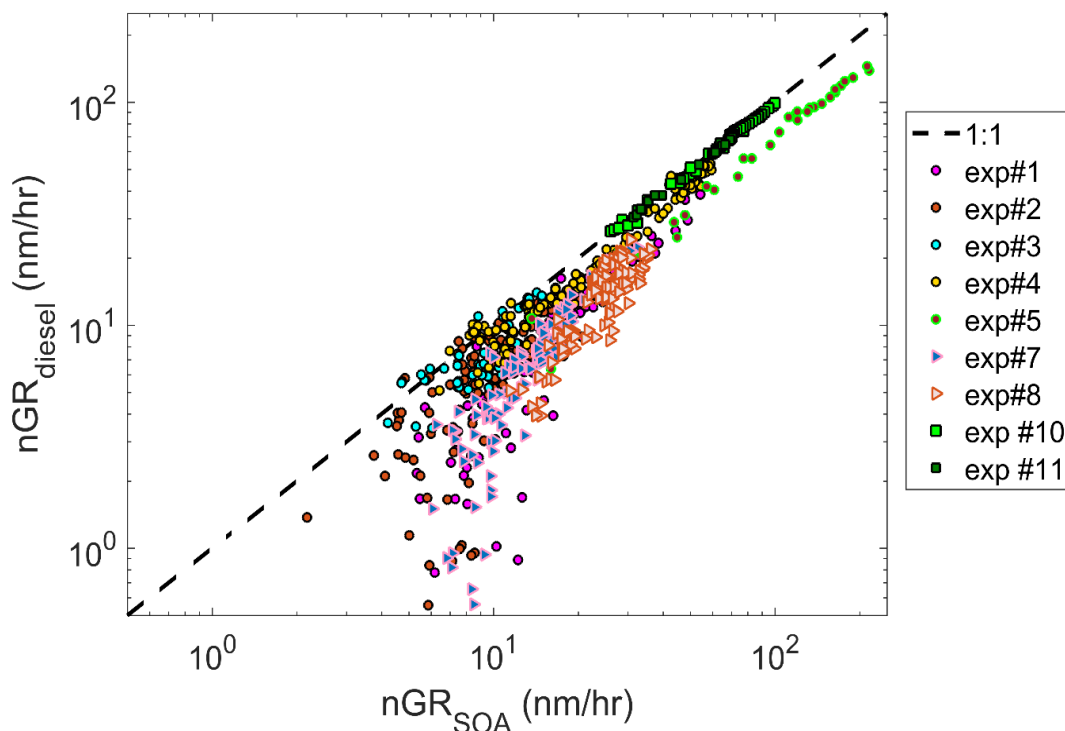
Figure 5.4 Log-log scatter plot of normalized growth rate (nGR, nm/hr) for diesel particles versus SOA particles. Square data points are the control experiments. Circle data points are the diesel versus SOA experiments coated with αp-SOA. Triangular data points are the diesel versus SOA experiments coated with squalane. For reference, straight lines with zero y-intercept (i.e., of the form Y=aX) run parallel to the 1:1 line. In contrast, straight lines with a negative y-intercept curve below the 1:1 line as nGR→0. nGR for the two control experiments (light and dark green squares) are also shown for reference.

There are trends in the data that are not directly apparent by looking at Figure 5.4. In the next sections we will analyze more closely some of the data. We separated growth experiments into three broad categories: (1) the fast growth rate experiment (experiment 5 in Table 5.1), (2) diesel versus SOA particles growth experiments using αp-SOA as

condensate material (experiments 1, 2, 3, 4, and 6 in Table 5.1) and (3) diesel versus SOA particles growth experiments using squalane as condensate material (experiments 7 and 8 in Table 5.1).

5.3.3.1 Fast Growth Rates

The data for Experiment 5 are given in Figure 5.5. The beginning of the experiment was marked by high normalized growth rates ~150 nm/hr for the SOA particles. The normalized growth rate then increased to ~250 nm/hr before decreasing to ~20 nm/hr at the end of the experiment (Figure 5.5a). These values are much higher than typical atmospheric growth (typically, a few nm/hr). The geometric mean diameter increase of diesel particles is shown in Figure 5.5b. During the experiment, diesel particles increased a mean diameter 60 nm to 108 nm in about an hour. During the experiment the ratio of the nGR for diesel particles to that of SOA particles (nGR_{diesel}/nGR_{SOA}) was nearly constant at around 0.67 (Figure 5.5b).

We can fit the data of Figure 5.5a to a linear fit passing through the origin (R^2=0.99). This proportionality between the growth rates of both seed particles is expected if the supersaturation ratio is large (Equation 5.12). We therefore infer that the ratio of the mass accommodation coefficients of the condensate material in the diesel and SOA particles is constant: $\overline{\alpha_{diesel}}/\overline{\alpha}_{SOA} = 0.67 \pm 0.01$.

We did not expect the proportionality factor between the growth rates from both seed particles be a constant throughout the experiment; we expected the ratio nGR_{diesel}/nGR_{SOA} to converge to unity towards the end of the experiment (diesel particles would have accumulated enough αp-SOA coating to "resemble" pure αp-SOA particles). This does not seem to be case. One potential explanation is that the least volatile compounds (which are responsible for condensational growth) diffuse inside the large SOA particles, therefore

changing the surface activity of the low volatility products. This mixing potentially does not occur to the same extent on the diesel particles because of their smaller sizes and because of the presence of a solid BC core.
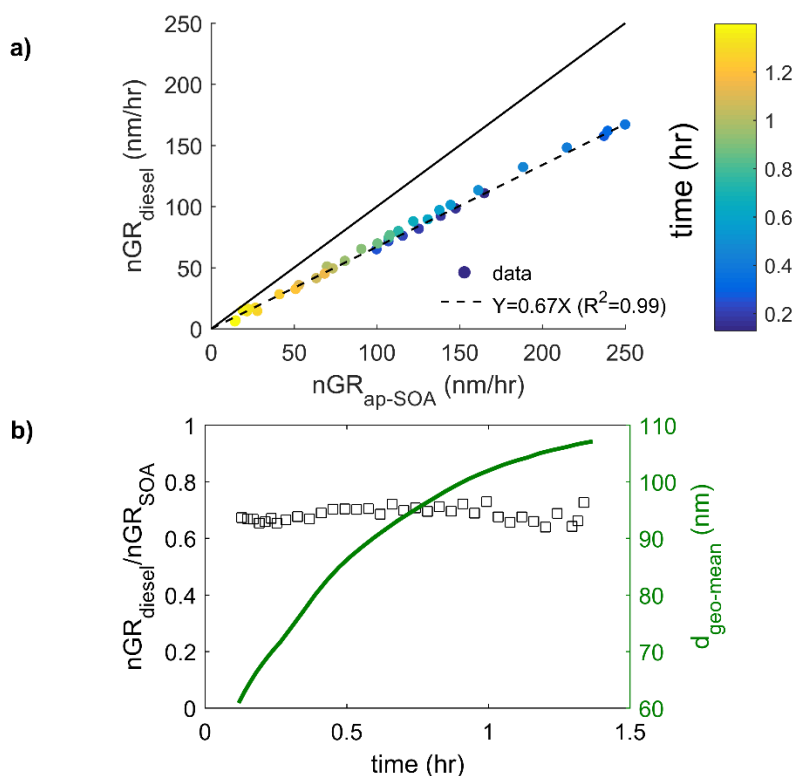
Figure 5.5 Fast growth experiment (experiment 5 in Table 5.1) for denuded diesel particles versus SOA particles coated with αp-SOA. The data in (a) are colored by time. The solid line is the 1:1 line; data below the 1:1 line indicates faster growth form SOA particles compared to diesel ones. The dashed line is the line of best fit. (b) Time series for the ratio of the nGR of diesel to that of SOA particles (square data points) and for the evolution of the geometric mean diameter of diesel particles.

5.3.3.2 Diesel versus SOA Particles Coated with αp-SOA

To assess the role of gas-phase supersaturation on the growth rates of particles, we also conducted experiments at lower growth rates. In this section we present data for the rest of the experiments using αp-SOA as condensate material (experiments 1, 2, 3, 4, and 6 in table 5.1). We will use experiment 3 as a case example.

The data for experiment 3 are shown in Figure 5.6. Growth rates of SOA particles increased from an initial value of ~6 nm/hr up to 60 nm/hr. Part of these values are higher than atmospheric conditions.
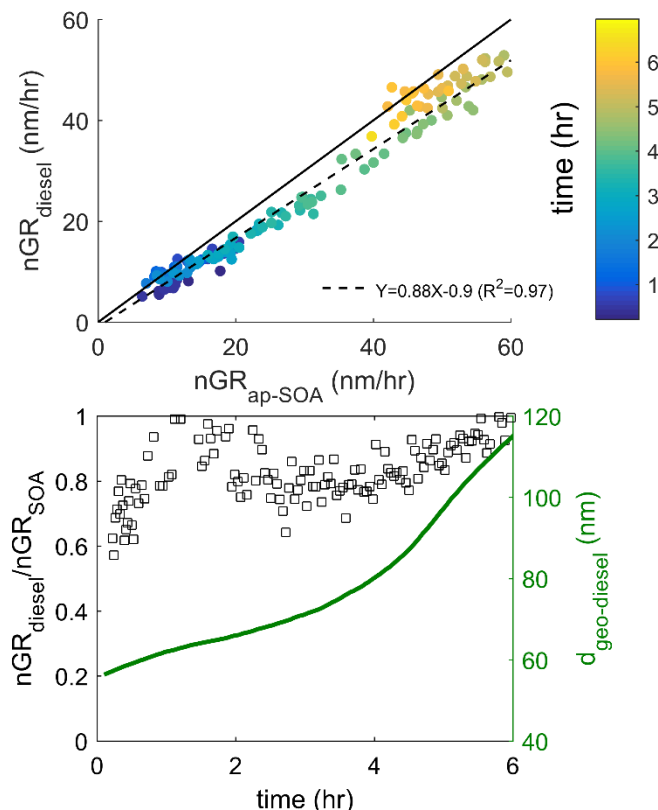
Figure 5.6 Growth experiment for diesel exhaust particles versus αp-SOA coated with αp-SOA. The figure follows the same format as Figure 5.5.

The geometric mean diameter for the diesel particles increased from 60 to 110 nm. This increase in diesel diameter is similar to the increase in diesel diameter during the fast growth rate experiment. However, experiment 3 lasted 6 times longer than experiment 5. We can fit the data in Figure 5.6a to a linear fit, but this would hide some subtilties in the data. Temporal trends become more apparent when plotting the ratio nGR_{diesel}/nGR_{SOA} (Figure 5.6b). In contrast to the fast growth experiment (experiment 4), we measured an increase in nGR_{diesel}/nGR_{SOA} from ~0.6 to ~1.0 over the course of the experiment. This indicates that the growth rates of the two seed particles are converging. We do not fully

understand yet why the growth rates between the two seed particles converged for this particular experiment but did not for the fast growth rate experiment.

5.3.3.3 Diesel versus SOA Particles Coated with Squalane

We also conducted two growth rate experiments (experiments 7 and 8 in Table 5.1) using squalane as the condensate material. The choice of squalane as a condensate material was not arbitrary. First, condensational growth using squalane vapors represents atmospheric growth from hydrocarbon-like organic aerosols (HOA). Second, squalane is a pure compound compared to the complex chemical composition of condensing material from the ozonolysis of alpha-pinene, and therefore simplifies data interpretation.

Figure 5.7 shows the data for experiment 7. The measured growth rate of SOA particles decreased from an initial value of 30 to 6 nm/hr over the entire experiment (Figure 5.7a). In contrast to experiments using SOA as condensate material, we measured a decrease in the ratio nGR_{diesel}/nGR_{SOA} as the particles were coated with squalane. This divergent behavior of growth rates might seem counter-intuitive since we are coating both seed particles using the same condensate material. We hypothesize that this divergence in growth rates is due to differences in particle-phase activities between condensate material and the diesel and SOA particles and/or enhanced surface saturation concentration of squalane around monomers forming the diesel aggregates (due to the Kelvin effect), effectively decreasing the condensational gradient.

Figure 5.7 Growth experiment for diesel exhaust particles versus αp-SOA coated with squalane. The figure follows the same format as Figure 5.5.
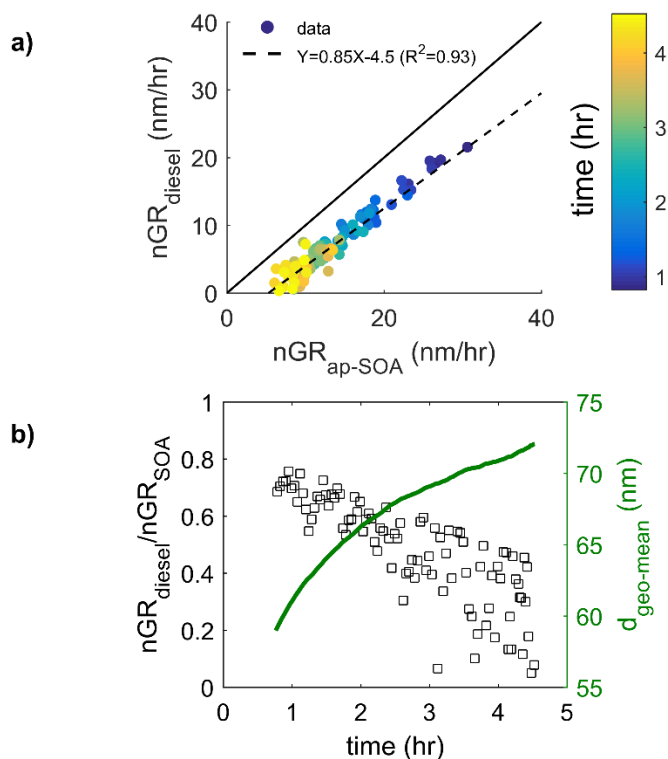
5.3.4 Effects of Seed Particles and Condensate Material on Particle Growth

In the previous section we have shown that the data can be fit to equations of the form $nGR_{diesel} = A \cdot nGR_{SOA} + B$, where A and B are constants. Using this formulation, A (the slope) is the ratio $\alpha_{diesel}/\alpha_{SOA}$ and B (the y-intercept) is proportional to the difference in the surface concentrations of the condensate material $C^* \cdot (a_{SOA} - K \cdot a_{diesel})$. Therefore, a negative y-intercept indicates that the surface concentration of the condensate material is larger in diesel particles compared to SOA particles, resulting in impeded growth of diesel particles (due to a smaller condensation force gradient).

The data for slope $(\alpha_{diesel}/\alpha_{SOA})$ and y-intercept ($\propto C^* (a_{SOA} - K \cdot a_{diesel})$) for all experiments are shown as box-whisker plots in Figure 5.8. The slope data combined experiments using SOA and squalane as condensate material because we measured no

139

differences between the two. In contrast, we separated the y-intercept data between experiments using SOA as condensate material and experiments using squalane as condensate material.
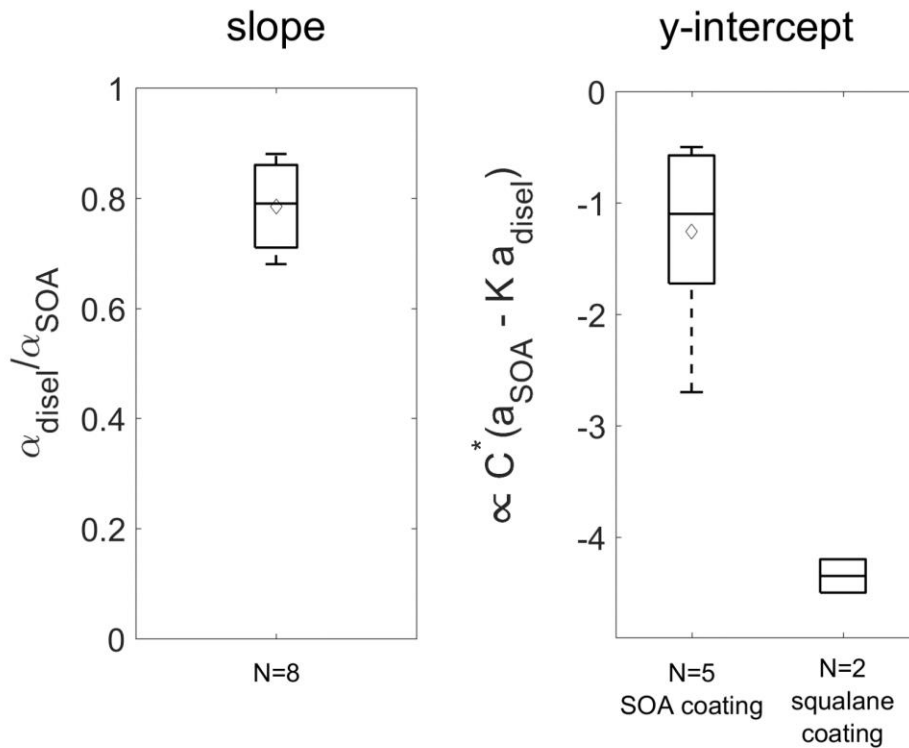
Figure 5.8 (a) Box-whisker plot of $\alpha_{\text{diesel}}/\alpha_{\text{SOA}}$ for all experiments (except experiment 9, Table 5.1). (b) Box-whisker plot for y-intercept data for experiments using SOA (N=5) and squalane (N=2) as condensate materials. The boxes represent the interquartile range and the whiskers extend to approximately ±2.7σ. The horizontal lines inside the boxes are median values and diamonds are averages.

It is clear from Figure 5.8 that the differences in measured growth rates shown in Figure 5.4 are caused by a combination of differences in particle-phase activity and differences in the mass accommodation coefficients. The average (interquartile range) of the ratio $\alpha_{\text{diesel}}/\alpha_{SOA}$ was 0.8 (0.7 – 0.9) (N=8). To a first approximation, this value indicates that,

on average, the growth rate of diesel particles was 20% slower than the growth rate of SOA particles.

On top of that, we need to account for differences in the condensational gradient between the two seed particles caused by differences in surface concentrations of the condensate material ($C^*(a_{SOA} - K.a_{diesel})$). Our data indicate that surface concentration differences (due to different seed material) plays a prominent role in determining particle growth (especially at low growth rates). Values for the y-intercept are shown in Figure 5.8b.

For all experiments, y-intercept data were negative, indicating that the surface concentration of the condensate material is larger on diesel particles compared to SOA particles. The fact that the surface concentration for the condensation material was always larger on diesel particles compared to SOA particles can be due to: (1) larger mixing of condensate material in the SOA particles compared to the diesel particles (due to their larger sizes) and/or (2) Kelvin effect around the monomers forming the diesel aggregates, effectively increasing the surface concentration of the condensate material on diesel particles compared to SOA particles (we estimated a 1.5 time enhancement in the saturation concentration of the condensate material coating 20 nm diameter monomers).

The average (interquartile range) of the y-intercept data (condensational gradient) was -1.3 (-1.7 – -0.6), (N=5) for all experiments using SOA as the condensate material. In contrast, the average of the y-intercept data for experiments using squalane as the condensate material was 3-fold smaller: -4.3 (-4.5 – -4.2), (N=2). One reason for the measured discrepancy could be differences in saturation concentrations (C^*) of squalane and SOA materials; the condensational gradient is directly proportional to C^*. Another reason could be that the surface tension of squalane is not strong enough to overcome Van-

der-Waals interactions between monomers and collapse the diesel aggregates. This would cause condensation of squalane around monomers, therefore enhancing the surface concentration of squalane on the diesel particles. Presumably collapse of the diesel aggregates is more prominent when coated with SOA, and condensation becomes less sensitive to the Kelvin effect.

5.4 Conclusions

We present experiments that probe the growth of different seed particles at different rates (including atmospherically relevant rates) and different condensates. Both seed particles were exposed to the same gas-phase supersaturation conditions. This allowed for a direct comparison of their growth rates. Using our experimental setup, we were able to successfully deconvolute the roles of the mass accommodation coefficient and surface activity on the growth of particles.

We successfully measured different growth rates from the different seed particles depending on gas-phase supersaturation (i.e., high versus slow growth rates), and condensate material. For all experiments, we found that the diesel particles exhibited slower growth rates compared to SOA particles. Our data suggest that the growth rate of BC particles is impeded compared to SOA particle growth due to two factors. (1) The mass accommodation coefficient of condensing material was on average 20% lower for BC particles compared to SOA particles. (2) Higher surface concentrations of the condensate material on the diesel particles compared to SOA particles.

Our measurements provide direct evidence that growth enhancements (due to differences in seed composition) can be observed on non-acidic seeds. Using our setup, we cannot explain the broad range of measured y-intercept data (i.e., differences in surface

concentration of the condensate material). The source of variability in y-intercept data is likely a combination of saturation concentration of condensate material, collapse of aggregates, and changes in surface activity (due to mixing of condensate material in the liquid phase or reactive uptake of vapors). However, it is important to explain this variability to better represent condensational growth of particles. This could help formulate better predictions of CCN concentrations in the atmosphere.

These results can have important implications on the atmospheric processing of BC particles (emitted form anthropogenic combustion sources), which compete for atmospheric condensate material with other non-BC particles shortly after emissions.

5.5 References

China, S.; Mazzoleni, C.; Gorkowski, K.; Aiken, A. C.; Dubey, M. K. Morphology and Mixing State of Individual Freshly Emitted Wildfire Carbonaceous Particles. *Nat. Commun.* **2013**, *4*, 2122.

Corbin, J. C.; Sierau, B.; Gysel, M.; Laborde, M.; Keller, A.; Kim, J.; Petzold, A.; Onasch, T. B.; Lohmann, U.; Mensah, A. A. Mass Spectrometry of Refractory Black Carbon Particles from Six Sources: Carbon-Cluster and Oxygenated Ions. *Atmos. Chem. Phys.* **2014**, *14* (5), 2591–2603.

Czoschke, N. M.; Jang, M.; Kamens, R. M. Effect of Acidic Seed on Biogenic Secondary Organic Aerosol Growth. *Atmos. Environ.* **2003**, *37* (30), 4287–4299.

Dal Maso, M.; Kulmala, M.; Riipinen, I.; Wagner, R.; Hussein, T.; Aalto, P. P.; Lehtinen, K. E. J. Formation and Growth of Fresh Atmospheric Aerosols: Eight Years of Aerosol Size Distribution Data from SMEAR II, Hyytiälä, Finland. *Boreal Environ. Res.* **2005**, *10* (5), 323–336.

DeCarlo, P.; Slowik, J. Particle Morphology and Density Characterization by Combined Mobility and Aerodynamic Diameter Measurements. Part 1: Theory. *Aerosol Sci. ...* **2004**, *38* (12), 1185–1205.

Donahue, N. M.; Robinson, A. L.; Stanier, C. O.; Pandis, S. N. Coupled Partitioning, Dilution, and Chemical Aging of Semivolatile Organics. *Environ. Sci. Technol.* **2006**, *40* (8),

2635–2643.

Fuchs, N. A.; Sutugin, A. G.; Hidy, G. M.; Brock, J. R. Topics in Current Aerosol Research. *Vol. 2Pergamon, New York* **1971**, 34.

Han, Y.; Stroud, C. A.; Liggio, J.; Li, S.-M. The Effect of Particle Acidity on Secondary Organic Aerosol Formation from &lt;i&gt;α&lt;/i&gt;-Pinene Photooxidation under Atmospherically Relevant Conditions. *Atmos. Chem. Phys.* **2016**, *16* (21), 13929–13944.

IPCC Working Group 1, I.; Stocker, T. F.; Qin, D.; Plattner, G.-K.; Tignor, M.; Allen, S. K.; Boschung, J.; Nauels, A.; Xia, Y.; Bex, V.; et al. IPCC, 2013: Climate Change 2013: The Physical Science Basis. Contribution of Working Group I to the Fifth Assessment Report of the Intergovernmental Panel on Climate Change. *IPCC* **2013**, *AR5*, 1535.

Jacobson, M. Z. Strong Radiative Heating due to the Mixing State of Black Carbon in Atmospheric Aerosols. *Nature* **2001**, *409*, 695–697.

Kulmala, M.; Vehkamäki, H.; Petäjä, T.; Dal Maso, M.; Lauri, A.; Kerminen, V. M.; Birmili, W.; McMurry, P. H. Formation and Growth Rates of Ultrafine Atmospheric Particles: A Review of Observations. *Journal of Aerosol Science*. 2004, pp 143–176.

Kuwata, M.; Kondo, Y.; Takegawa, N. Critical Condensed Mass for Activation of Black Carbon as Cloud Condensation Nuclei in Tokyo. *J. Geophys. Res. Atmos.* **2009**, *114* (20).

Lambe, A. T.; Chhabra, P. S.; Onasch, T. B.; Brune, W. H.; Hunter, J. F.; Kroll, J. H.; Cummings, M. J.; Brogan, J. F.; Parmar, Y.; Worsnop, D. R.; et al. Effect of Oxidant Concentration, Exposure Time, and Seed Particles on Secondary Organic Aerosol Chemical Composition and Yield. *Atmos. Chem. Phys.* **2015**, *15* (6), 3063–3075.

Lohmann, U.; Lesins, G. Stronger Constraints on the Anthropogenic Indirect Aerosol Effect. *Science (80-.).* **2002**, *298* (5595), 1012–1015.

Moffet, R. C.; Prather, K. a. In-Situ Measurements of the Mixing State and Optical Properties of Soot with Implications for Radiative Forcing Estimates. *Proc. Natl. Acad. Sci. U. S. A.* **2009**, *106*, 11872–11877.

Mohr, C.; Huffman, J. A.; Cubison, M. J.; Aiken, A. C.; Docherty, K. S.; Kimmel, J. R.; Ulbrich, I. M.; Hannigan, M.; Jimenez, J. L. Characterization of Primary Organic Aerosol Emissions from Meat Cooking, Trash Burning, and Motor Vehicles with High-Resolution Aerosol Mass Spectrometry and Comparison with Ambient and Chamber Observations. *Environ. Sci. Technol.* **2009**, *43* (7), 2443–2449.

Onasch, T. B.; Trimborn, A.; Fortner, E. C.; Jayne, J. T.; Kok, G. L.; Williams, L. R.; Davidovits, P.; Worsnop, D. R. Soot Particle Aerosol Mass Spectrometer: Development, Validation, and Initial Application. *Aerosol Sci. Technol.* **2012**, *46* (7), 804–817.

Park, K.; Kittelson, D. B.; McMurry, P. H. Structural Properties of Diesel Exhaust Particles Measured by Transmission Electron Microscopy (TEM): Relationships to Particle Mass and Mobility. *Aerosol Sci. Technol.* **2004**, *38* (9), 881–889.

Presto, A. A.; Donahue, N. M. Investigation of Alpha-Pinene + Ozone Secondary Organic Aerosol Formation at Low Total Aerosol Mass. *Environ. Sci. Technol.* **2006**, *40*, 3536–3543.

Presto, A. A.; Huff Hartz, K. E.; Donahue, N. M. Secondary Organic Aerosol Production from Terpene Ozonolysis. 2. Effect of NOx Concentration. *Environ. Sci. Technol.* **2005**, *39*, 7046–7054.

Riemer, N.; Vogel, H.; Vogel, B. Soot Aging Time Scales in Polluted Regions during Day and Night. *Atmospheric Chemistry and Physics*. 2004, pp 1885–1893.

Riipinen, I.; Yli-Juuti, T.; Pierce, J. R.; Petäjä, T.; Worsnop, D. R.; Kulmala, M.; Donahue, N. M. The Contribution of Organics to Atmospheric Nanoparticle Growth. *Nat. Geosci.* **2012**, *5* (7), 453–458.

Rosenfeld, D. Aerosol-Cloud Interactions Control of Earth Radiation and Latent Heat Release Budgets. *Space Sci. Rev.* **2006**, *125* (1–4), 149–157.

Saleh, R.; Donahue, N. M.; Robinson, A. L. Time Scales for Gas-Particle Partitioning Equilibration of Secondary Organic Aerosol Formed from Alpha-Pinene Ozonolysis. *Environ. Sci. Technol.* **2013**, *47* (11), 5588–5594.

Saliba, G.; Subramanian, R.; Saleh, R.; Ahern, A. T.; Lipsky, E. M.; Tasoglou, A.; Sullivan, R. C.; Bhandari, J.; Mazzoleni, C.; Robinson, A. L. Optical Properties of Black Carbon in Cookstove Emissions Coated with Secondary Organic Aerosols: Measurements and Modeling. *Aerosol Sci. Technol.* **2016**, *50* (11), 1–13.

Schnaiter, M. Absorption Amplification of Black Carbon Internally Mixed with Secondary Organic Aerosol. *J. Geophys. Res.* **2005**, *110* (D19), D19204.

Seinfeld, J. H.; Pandis, S. N. *Atmospheric Chemistry and Physics: From Air Pollution to Climate Change*; 2006.

Shiraiwa, M.; Kondo, Y.; Iwamoto, T.; Kita, K. Amplification of Light Absorption of Black Carbon by Organic Coating. *Aerosol Sci. Technol.* **2010**, *44* (1), 46–54.

Slowik, J. G.; Stainken, K.; Davidovits, P.; Williams, L. R.; Jayne, J. T.; Kolb, C. E.; Worsnop, D. R.; Rudich, Y.; DeCarlo, P. F.; Jimenez, J. L. Particle Morphology and Density Characterization by Combined Mobility and Aerodynamic Diameter Measurements. Part 2: Application to Combustion-Generated Soot Aerosols as a Function of Fuel Equivalence Ratio. *Aerosol Sci. Technol.* **2004**, *38* (12), 1206–1222.

Sorensen, C. M. The Mobility of Fractal Aggregates: A Review. *Aerosol Sci. Technol.* **2011**, *45* (7), 765–779.

Stolzenburg, M. R.; McMurry, P. H.; Sakurai, H.; Smith, J. N.; Mauldin, R. L.; Eisele, F. L.; Clement, C. F. Growth Rates of Freshly Nucleated Atmospheric Particles in Atlanta. *J. Geophys. Res. Atmos.* **2005**, *110* (22), 1–10.

Subramanian, R.; Kok, G. L.; Baumgardner, D.; Clarke, A.; Shinozuka, Y.; Campos, T. L.; Heizer, C. G.; Stephens, B. B. Black Carbon over Mexico: The Effect of Atmospheric Transport on Mixing State, Mass Absorption Cross-Section, and BC/CO Ratios. *Atmospheric Chemistry and Physics*. **2010**, *10*(1).

Takahama, S.; Davidson, C. I.; Pandis, S. N. Semicontinuous Measurements of Organic Carbon and Acidity during the Pittsburgh Air Quality Study: Implications for Acid-Catalyzed Organic Aerosol Formation. *Environ. Sci. Technol.* **2006**, *40* (7), 2191–2199.

Twomey, S. The Influence of Pollution on the Shortwave Albedo of Clouds. *J. Atmos. Sci.* **1977**, *34* (7), 1149–1152.

Vehkamäki, H.; Riipinen, I. Thermodynamics and Kinetics of Atmospheric Aerosol Particle Formation and Growth. *Chem. Soc. Rev.* **2012**, *41* (15), 5160.

Weber, R. J.; Marti, J. J.; McMurry, P. H.; Eisele, F. L.; Tanner, D. J.; Jefferson, a. Measurements of New Particle Formation and Ultrafine Particle Growth Rates at a Clean Continental Site. *Journal of Geophysical Research: Atmospheres*. 1997, pp 4375–4385.

Weingartner, E.; Burtscher, H.; Baltensperger, U. Hygroscopic Properties of Carbon and Diesel Soot Particles. *Atmos. Environ.* **1997**, *31* (15), 2311–2327.

Zhang, Q.; Jimenez, J. L.; Worsnop, D. R.; Canagaratna, M. A Case Study of Urban Particle Acidity and Its Influence on Secondary Organic Aerosol. *Environ. Sci. Technol.* **2007**, *41* (9), 3213–3219.

CHAPTER 6
CONCLUSIONS

6.1 Summary of Scientific Findings

The research presented in this dissertation addressed key uncertainties in emissions and optical properties of aerosol emitted from biofuel (cookstoves) combustion and gasoline vehicles. We also investigated the role of atmospheric processing on the optical properties and growth rates of particles. The dissertation had three primary objectives. Below, we summarize the scientific findings and key results for each objective.

Objective I – Investigate the climate impacts of aerosol emissions from recently adopted new energy technologies: improved cookstoves and gasoline direct injection (GDI) engines.

Cookstoves and vehicles are undergoing fast technology transitions. So-called "improved" cookstoves are being widely deployed in developing countries because of their reduced particulate matter (PM) emissions. There are potential health and climate co-benefits from improved cookstove emissions. However, improved cookstoves can have increased black carbon (BC) emissions which could offset their climate benefits. Also, GDI technology is being very rapidly adopted. Older GDI engines have higher emissions than PFI, but the GDI technology is rapidly evolving. There are limited data on latest vehicles which limits our understanding of the climate impacts of adopting GDI technology.

In chapter 3 we assessed the climate implications of switching traditional cookstoves to more efficient improved cookstoves. We performed extensive experiments using 18 different cookstove technology and fuels combinations to measure the suite of optical

properties of fresh cookstove emissions. We tested a wide range of cookstove models; from highly emitting traditional cookstoves to cleaner gasifier cookstoves. The cookstoves were tested in the laboratory using the newly developed firepower sweep protocol, which covers a wide range of operating conditions. Using the data, we developed parametrizations for the BC-mass absorption cross section (MAC_{BC}), the absorption angstrom exponent (AAE, wavelength dependence of MAC_{BC}), and the single scattering albedo (SSA) as a function of the BC-to-PM mass ratio for fresh cookstove emissions. Our parametrizations largely explain the significant variability in measured optical properties both in the field and in the laboratory. We combined these parametrizations with field emissions from 6 published datasets to assess the climate impacts from the advent of various cookstove technologies. We estimate modest climate benefits from deploying these improved stoves: average 4% and 30% reductions in the radiative forcing of emissions from rocket-style and gasifier cookstoves respectively compared to traditional ones. These cookstoves also have lower PM emission rates, indicating that there are health and climate co-benefits.

In Chapter 4 we investigated the climate implications from switching engine technologies, from widely used port fuel injection (PFI) to GDI engines. GDI engines are more fuel efficient compared to PFI engines, but recent studies have shown increased BC emission rates and increased fraction of BC from GDI engine emissions, which will offset some of the climate benefits from decreased CO_2 emissions (Zhang and McMahon, 2012; Short et al., 2015; Zimmerman et al., 2016). However, these studies tested few GDI-equipped vehicles certified to the most stringent emission certifications. We tested GDI and PFI equipped-vehicles certified to the most stringent emission certifications (super-ultra-low emission vehicles (SULEV)). The vehicles were tested on a chassis dynamometer using the cold-start Unified Cycle, at the ARB Haagen-Smit laboratory. We combined our

tested vehicles with 2 previous field campaigns to create a comprehensive emissions database for 82 light-duty gasoline vehicles.

We measured on average a factor of six higher BC emission rates from older GDI engines compared to older PFI engines, consistent with results from previous studies. However, SULEV certified GDI engines had a factor of three higher BC emission rates compared to SULEV PFI engines. These improvements in emissions may enable GDI-equipped vehicles to meet the new Federal Tier 3 PM standard of 3.0 mg/mi starting in 2017 without gasoline particulate filters (GPF, which would offset part of their fuel economy). We assessed the climate impacts of increased fuel economy (i.e., decreased CO_2 emissions) and increased BC emissions from switching PFI to GDI engines. We found that the average measured increase in BC emission rates of 2 mg/mi from GDI versus PFI vehicles did not offset the average decrease in CO_2 emissions rates of 57 g/mi. We estimated that the increased BC emissions from GDIs reduces their climate benefits by 10% to 20%, however this value is likely higher in the real-world due to lower real-world measured fuel economy form GDI engines compared to values obtained on the cold-start Unified Cycle.

<u>Key findings from objective I:</u>

- Switching traditional to improved cookstoves will likely provide modest climate benefits.

- Switching GDI engines to PFI engines will likely result in decreased warming from emissions.

Objective II – Develop parametrizations of optical properties of fresh cookstove emissions.

Cookstoves are an important source of BC particles to the atmosphere (Bond et al., 2013), but their emissions are highly variable due to uncontrolled combustion conditions. Moreover, there are limited published data of the optical properties of real-world cookstove emissions. We need to understand and explain the variability in emissions and optical properties to assess the global climate impacts from switching cookstove technologies.

In chapter 4, we conducted laboratory experiments to comprehensively characterize the gas and particle emissions from a suite of cookstove technologies and fuel combinations using the firepower sweep protocol. The data were used to develop parametrizations to explain the large variability in published data of optical properties from cookstove emissions in the field and in the laboratory.

We compared our newly developed parametrizations with predictions from Mie theory. We found that assuming a complete internal mixture between PM and BC resulted in Mie theory over predicting the absorption from fresh cookstove emissions. It is therefore likely that the optical properties of freshly emitted BC particles are poorly represented in the climate models that treat lensing of coated BC particles, because these models assume complete internal mixture of BC and non-BC material. Moreover, we measured increased contribution to absorption from brown carbon (BrC) with increased BC-to-PM mass ratios. BrC contribution to absorption from cookstove emissions was smaller compared to predictions of BrC absorption based on parametrizations developed for biomass burning emissions (Saleh et al., 2014). These findings suggest that climate models need improved representations of the optical properties of fresh cookstove emissions. Our parametrizations can be implemented in climate models to rigorously assess the global

climate implications from adoption of different improved stove technologies, using a multitude of published emission data.

When we combined the measured mixing-state (measured qualitatively using a single-particle soot-photometer, SP2) of the fresh cookstove emissions with Mie theory, we found the Mie theory agreed well with measured absorption of fresh cookstove emissions (assuming absorptive non-BC material).

<u>Key findings from objective II:</u>

- Climate models that assume complete internal mixture between BC and non-BC material likely overestimate the absorption (i.e., warming) of fresh cookstove emissions.

- Mie theory can approximate the absorption of fresh cookstove emissions provided the BC-mixing state is known

<u>Objective III – Quantify the atmospheric evolution of aerosol emissions and their impact on optical properties</u>

Upon entering the atmosphere, aerosols interact in complex ways with other compounds. The optical properties of BC particles depend on the atmospheric processing which controls the accumulation of coating around the BC cores. Also, the growth rate of BC particles can affect their atmospheric lifetime by affecting the dry and wet deposition rates of BC particles. However, current models do not account for seed-dependent growth rates.

In chapter 2, we presented results from controlled experiments to investigate the role of the coating material on the optical properties of nascent BC particles emitted from a rocket-style cookstove and coated with SOA from the ozonolysis of alpha-pinene. The experiments used size-selected BC particles and non-absorbing coating material (no BrC). We coated the BC cores in a controlled manner to ensure complete internal mixture between SOA material and BC particles. These experiments explicitly target to evaluate measurements and modeling using simple formulation like Mie theory and the Rayleigh-Debye-Gans (RDG) formulation. We measured data for MAC_{BC} and MSC for fresh and coated BC particles and used the data to evaluate the performance of Mie and RDG formulations. Our results indicate that Mie theory can predict both absorption and scattering enhancement from emissions when the particles are sufficiently coated (organic-to-BC mass ratio > 5). However, at low coating thicknesses, measured scattering agreed better with RDG predictions and the data suggest fractal-like BC particles.

In chapter 5, we investigated the role of seed particle composition and gas-phase supersaturation conditions on the growth rates of particles. We examined fresh diesel and SOA particles from the ozonolysis of alpha-pinene as our seed particles, and SOA and squalane as condensate material. To accurately measure differences in growth rates from both seed particles, we had both seeds present in the same environment (i.e., exposed to the same gas-phase conditions). Using this setup, we measured differences in growth rates that varied on both the seed and condensate materials.

We estimated that the mass accommodation of condensing material (for both SOA and squalane) was 10% to 30% lower on the diesel particles compared to the SOA particles. Moreover, we found larger surface concentrations of condensate materials on the diesel particles potentially due to less-miscible condensing vapors in the diesel phase compared

to the SOA particles. Our data suggest that growth of BC (diesel) particles in the atmosphere is likely slower compared to SOA particles. Accurately representing these processes is important to estimate the lifetime and absorption enhancement from coated BC particles, as they compete with other particles for condensable vapors.

<u>Key findings from objective III:</u>

- Mie theory predicts the absorption and scattering of coated BC particles and can be used in climate models if the mixing-state of BC particle is known.

- Seed-dependent differences in growth rates of particles will likely need to be incorporated in models to better understand atmospheric processing and its effect on lifetime and optical properties.

6.2 Future Work

In this dissertation, we investigated key uncertainties regarding the overall direct radiative forcing of BC particles: emissions, optical properties, and atmospheric processing (lifetime).

In chapter 3 we investigated the radiative implications from various stove technologies and developed parametrizations to address the large variability in field measurements of optical properties. Our measurements revealed the presence of BrC in emissions. Improved characterization of the BrC optical properties is needed to reduce uncertainty. Only Roden et al., (2006) reports field measurements of the absorption angstrom exponent (an indication of the presence of BrC) from real-world stove emissions. More field measurements of optical properties of BrC emissions from cookstoves are needed to more thoroughly evaluate our proposed parametrizations.

In chapter 3, we also presented comprehensive parametrizations of the optical properties as a function of the BC-to-PM. These parameterizations can be combined with source emissions in radiative transfer models to estimate the global impacts from switching cookstove technologies. These parameterizations should be implemented in models and inventories to systematically investigate the contribution of cookstove emissions to climate forcing. For example, Kodros et al., (2015) used parametrizations of the optical properties of BrC, developed for biomass burning emissions by Saleh et al., (2014), to estimate the global direct radiative forcing of cookstove emissions. Output form radiative models using our parameterizations can be compared to output using different parametrizations like the one proposed by Saleh et al., (2014) to assess the sensitivity of the radiative forcing from BrC particles on their optical treatment.

In chapter 4 we reported a discrepancy in PM mass emission rates between our measurements and EMFAC predictions, primarily due to under-represented PM emission rates from new PFI vehicles. It corresponded to 0.15 Gg PM in 2014, which is four time larger than the EMFAC predictions for all model year 2004 – 2014 gasoline vehicles. This discrepancy needs to be corrected in emission inventories. Also presented in chapter 4 is a comprehensive gas and particle emissions database. Model simulations using our dataset should be performed to evaluate the impacts of widespread adoption of GDI vehicles on human exposure and health in urban areas, with a focus on near road environments.

Chapter 5 provides some of the initial evidence that particle growth rates depend on seed composition. The next steps of this work are to: (1) compare measurements of growth rates with a condensational microphysics scheme. (2) Perform more chamber experiments to enlarge our data set and explore growth rates from more different seed materials. (3) Explain and parametrize the variability in activity and mass accommodation coefficients

data estimated from our experiments. One key challenge of these experiments is to be able to physically distinguish between the two seed particles. This was not very challenging for our system of SOA and diesel particles because the diesel mode was small, but could prove to be more difficult in the future with different systems.

6.3 References

Bond, T. C.; Doherty, S. J.; Fahey, D. W.; Forster, P. M.; Berntsen, T.; DeAngelo, B. J.; Flanner, M. G.; Ghan, S.; Kärcher, B.; Koch, D.; et al. Bounding the Role of Black Carbon in the Climate System: A Scientific Assessment. *J. Geophys. Res. Atmos.* **2013**, *118* (11), 5380–5552.

Kodros, J. K.; Scott, C. E.; Farina, S. C.; Lee, Y. H.; L'Orange, C.; Volckens, J.; Pierce, J. R. Uncertainties in Global Aerosols and Climate Effects due to Biofuel Emissions. *Atmos. Chem. Phys.* **2015**, *15* (15), 8577–8596.

Roden, C. A.; Bond, T. C.; Conway, S.; Osorto Pinel, A. B. Emission Factors and Real-Time Optical Properties of Particles Emitted from Traditional Wood Burning Cookstoves. *Environ. Sci. Technol.* **2006**, *40*, 6750–6757.

Saleh, R.; Robinson, E. S.; Tkacik, D. S.; Ahern, A. T.; Liu, S.; Aiken, A. C.; Sullivan, R. C.; Presto, A. a.; Dubey, M. K.; Yokelson, R. J.; et al. Brownness of Organics in Aerosols from Biomass Burning Linked to Their Black Carbon Content. *Nat. Geosci.* **2014**, *7*, 1–4.

Short, D. Z.; Vu, D.; Durbin, T. D.; Karavalakis, G.; Asa-Awuku, A. Components of Particle Emissions from Light-Duty Spark-Ignition Vehicles with Varying Aromatic Content and Octane Rating in Gasoline. *Environ. Sci. Technol.* **2015**, *49* (17), 10682–10691.

Zhang, S.; McMahon, W. Particulate Emissions for LEV II Light-Duty Gasoline Direct Injection Vehicles. *SAE Int. J. Fuels Lubr.* **2012**, *5*, 637–646.

Zimmerman, N.; Wang, J. M.; Jeong, C.-H.; Ramos, M.; Hilker, N.; Healy, R. M.; Sabaliauskas, K.; Wallace, J. S.; Evans, G. J. Field Measurements of Gasoline Direct Injection Emission Factors: Spatial and Seasonal Variability. *Environ. Sci. Technol.* **2016**, *50* (4), 2035–2043.